Petra

21.2.2009

Field leader

Tina M. Niemi

Paleoseismology and archaeoseismology of sites in Aqaba and Petra, Jordan

Tina M. Niemi*[1]

[1]Department of Geosciences, University of Missouri - Kansas City

NiemiT@umkc.edu

*Field guide

QUATERNARY GEOLOGY OF AQABA

Aqaba, Jordan is built predominantly on alluvial fan sediment derived from the adjacent mountain ranges to the east (Fig. 1). The drainage basin of the Wadi Yutim reaches far into the eastern plateau and covers a minimum area of 1100 km^2. It is the largest drainage system in the southern 'Arabah valley and flows into the 'Ain Defiya depression in Eilat. Several branches of the Wadi Yutim flow southwestward toward the Gulf of Aqaba. The Aqaba Regional Authority has constructed flood control measures to divert runoff away from the city of Aqaba.

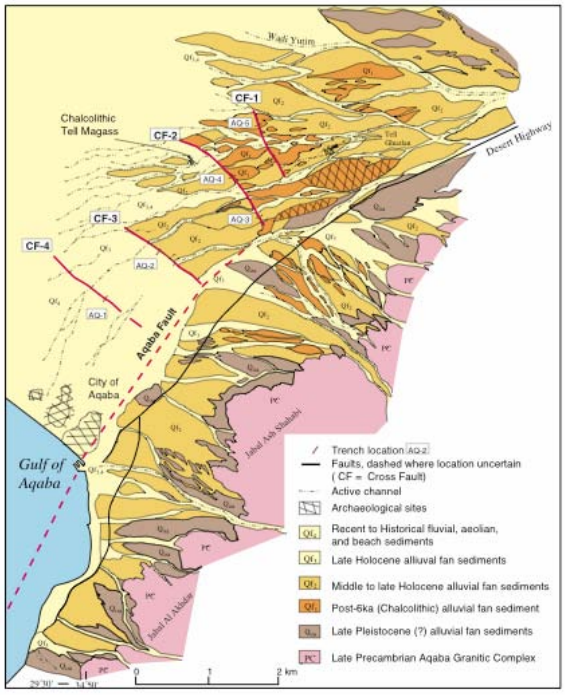

Figure 1. Geologic map of the Aqaba region based on interpretation of 1:25,000 scale airphoto from 1953. Cross fan faults (CF 1-4) are mapped as continuous lines even though these features are eroded by wadi washes. These cross faults formed as normal to oblique-slip faults associated with a left stepover in the Dead Sea Transform. Locations AQ 1-3 mark the sites of exploratory trenches excavated across the NW-trending faults. A high concentration of archaeological ruins in the Aqaba area provide age constraints on surface deformation and provide a unique record of damage from past earthquakes (modified from Niemi and Smith, 1999).

Niemi and Smith (1999) divided the alluvial fan sequence in the Aqaba region into five mappable fan units (Q_{oa}, Qf_1, Qf_2, Qf_3 and Qf_4). Remnants of a Pleistocene alluvial fan sequence, designated Q_{oa}, located near the mountain front, may correlate to the Upper Pleistocene fan surfaces mapped on the Shehoret alluvial fan sequence west side in Israel. The oldest Holocene alluvial fan surface (Qf_1) is distinguished by a moderately developed desert varnish. It overlies archaeological artifacts from the Chalcolithic period (Tell Magass and Tell Ghuzlan) dated to 5-6 ka. The Qf_2 fan surface is slightly inset into or buries the Qf_1 surface. The age of the Qf_2 fan surface is unknown. The young alluvial fan deposits are generally incised across older fan surfaces and include the active channel deposits and distal fan sediments. The youngest unit also contains aeolian and beach sediment within the coastal zone.

PALEOSEISMOLOGY

Airphoto interpretation of the Aqaba regional surficial geology (Fig. 1) suggests that a strike-slip fault emerges from the gulf and that slip is transferred to cross faults. This geometry constrains the location of the Aqaba fault to lie east of the cross faults and west of alluvial fan surfaces that contain no north- to northeast-striking fault lineaments. The location of the Aqaba fault is therefore believed to lie within a 500-m swath that is covered by the modern city (Fig. 1). It appears that the Aqaba fault follows a recent wadi that has obliterated its active fault morphology. A ground-penetrating radar survey in the city confirmed the location of a portion of the Aqaba fault (Slater and Niemi, 2003; Abueladas, 2005; Abueladas *et al.*, in prep).

The Aqaba fault apparently trends northeast with increasing curvature as it dies out toward the northeast. This bending to the northeast of the eastern bounding fault of a pullapart has been noted for other large pullapart basins along the Dead Sea Transform including the Dead Sea and the Sea of Galilee (Garfunkel *et al.*, 1981; Garfunkel, 1981). Reches (1987) showed using clay model experiments that that faults initially bend away from each other at a dilational jog in ductile materials. This geometry led Reches (1987) to conclude that the Arabian plate was thickening by ductile deformation. The Aqaba fault

should therefore have a reverse component to its motion. New GPR data across the fault confirm this prediction (Abueladas *et al.*, in prep; Fig. 2).

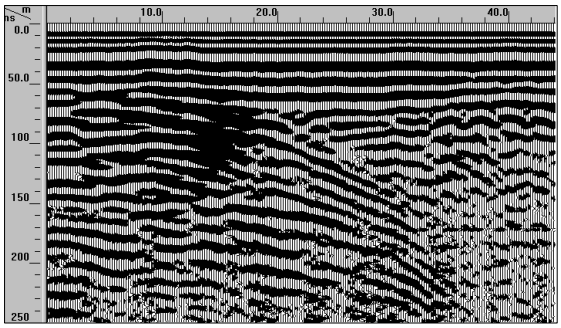

Figure 2. GPR profile highlighting the potential reverse component of the Aqaba fault. These data were collected as part of the MERC project "High resolution marine geophysical imaging of active faults in the Aqaba-Eilat region".

Geological trenches excavated across several faults in Aqaba document that the fault motion is transferred from the Aqaba fault onto five northwest - trending cross-faults that produce active tectonic subsidence at the head of the Gulf (Mansoor, 2002; Slater and Niemi, 2003; Fig. 4). Mapping of alluvial fan and buried soil horizons in trenches excavated on three of the cross faults reveal multiple fault ruptures on the highest scarps and fewer distinct ruptures on the lowest scarp (Mansoor, 2002). The scarp heights range from 25 cm across the youngest Qf_4 surface to 1.3 m across the older Qf_1 and Qf_2 surfaces. These data indicate that scarp heights reflect cumulative slip events. The most recent scarp-forming event fault occurred after A.D. 1045-1278 based on a corrected, calibrated radiocarbon age from charcoal collected from a buried campfire at the base of the scarp (Fig. 3). This likely represents fault motion in either the historical earthquakes of 1212 or 1068.

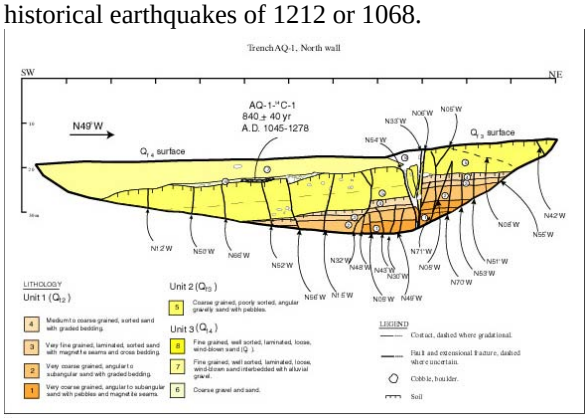

Figure 3. Trench log of the north wall of AQ-1 excvated across the cross fault 4 (Mansoor, 2002).

ARCHAEOSEISMOLOGY IN AQABA

Islamic Ayla

Based both on the historical accounts and the archaeological work of Whitcomb and Parker (*e.g.* 1996), it is clear that earthquakes have played a significant role in the history of the Aqaba region. The exact location of the Aqaba fault remains somewhat uncertain because it has never been exposed in paleoseismic trenches in this heavily urbanization location. Whitcomb (1993; 19) hypothesized that the wadi running across the ancient site of Ayla has its origins in erosion along the structural weakness of the fault itself. Thus, our main objective in investigating the city wall of Ayla was to test this hypothesis and to locate the Aqaba fault.

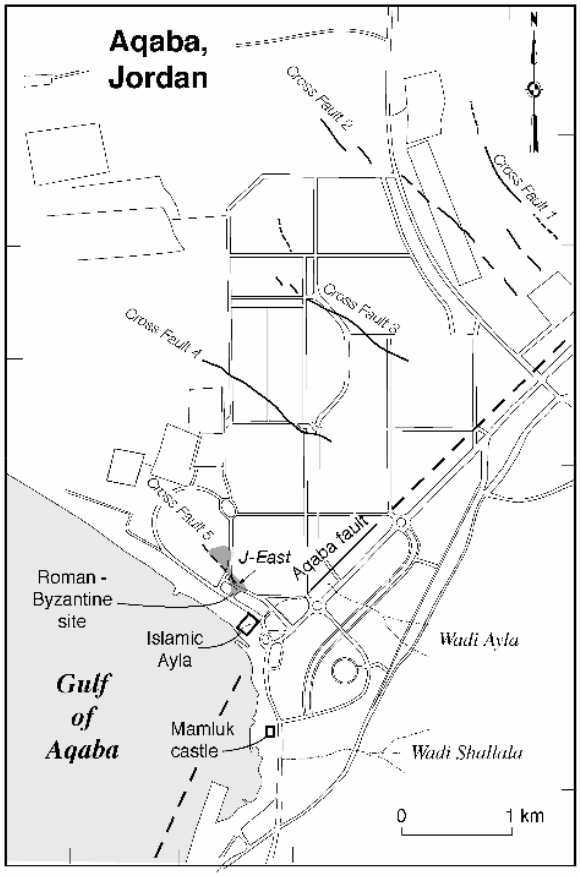

Figure 4. Map of the city of Aqaba showing the location of major archaeological sites. Active cross faults (CF) mapped from aerial photos and discovered in the archaeological excavations of J-east are also shown (Thomas et al., 2007).

The Early Islamic site of Ayla, extensively excavated by Donald Whitcomb of the Oriental Institute at the University of Chicago, is a walled city, circa 250 m southeast of the Byzantine city wall excavated by Parker (1996; 2002), and approximately 850 m north of the Mamluk castle in modern Aqaba (Fig. 4). The city of Islamic Ayla was probably founded under the Caliph 'Uthman ibn 'Affan around 650 A.D. (Whitcomb, 1995; 277). The city seems to have suffered some damage as a result of the 748 A.D. earthquake, and extensive reconstruction with the beginning of the Abbasid period (Whitcomb,

1994; 9). It is described by al-Muqaddasi in the late 10th century, as he described it in reference to the ruins nearby of the Roman/Byzantine site (after Whitcomb, 1997; 359). The town was severely damaged by the earthquake in 1068 A.D. (Ambraseys, 1994; 31). The destruction and loss of life (accounts claim that all but 12 residents who had been out fishing were killed) caused by this earthquake may account for the relative ease with which Baldwin I of Jerusalem took over when he arrived with a small retinue in 1116 A.D. Baldwin I constructed a small fortification (the origin of the current castle?), and a new settlement grew up around this (Whitcomb, 1997; 359). The site of Islamic Ayla was apparently never reoccupied to any significant degree after the time of the Crusaders.

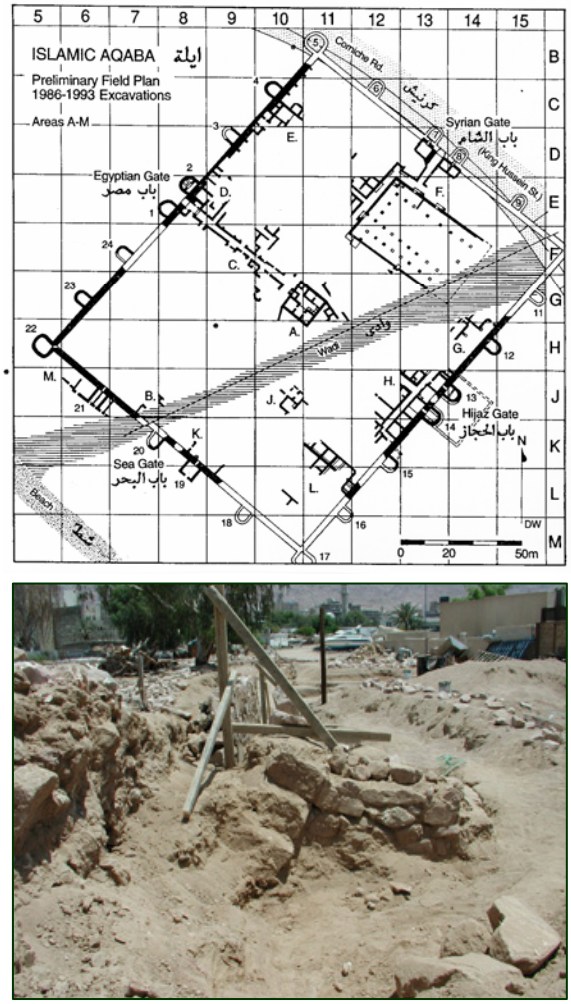

Figure 5. (Top) Site Plan of Early Islamic Ayla, from Whitcomb (1995). (Bottom) Section of the Sea Wall, tilted outward and buttressed in antiquity, with reconstructed wall on original alignment in background, view to SE.

Al-Hamoud and Tal (1998) conducted geotechnical investigations using three boreholes to a depth of 12m on the tell of Islamic Ayla. Archaeological deposits overlie sand and gravels. They noted tilting and sinking of exterior walls that they interpreted as slumping due to horizontal ground acceleration in an earthquake. Similar conclusions were reported by Al-Tarazi and Koryenkov (2007). According to the analyses of Mansoor *et al.* (2004), Ayla lies in an area of high liquefaction susceptibility due to the presence of saturated sands at shallow depth. This means that during seismic shaking, the substrate may lose its ability to bear weight, resulting in collapse of structures. Areas in the city of Aqaba that experienced subsidence in the Nuweiba earthquake of 1995 lie along the beach zone near the ancient site of Ayla (Wust 1997; Malkawi *et al.*, 1999; Al-Tarazi, 2000).

Rucker and Niemi (2005) reported on the results of excavation of the northeast corener tower the walled citadel of Islamic Ayla. In the four trenches excavated, the wall aligns across the entire width of the wadi indicating that no fault offset is present in the NE or SE city wall or through the corner tower in the wadi. Furthermore, the 2001 Department of Antiquities restoration project in the south corner of the site revealed a section of the Sea Wall that was tilted outward (Fig. 5). The outer edge of this section before excavation would have appeared on the ground surface 1.5 to 2m from the alignment of its actual foundation. Interestingly, it appeared to have been buttressed and continued in use in antiquity. This phenomenon, (easily caused by liquefaction and subsidence, not faulting) may provide an explanation for the apparent misalignment in the Sea wall above foundation levels observed by Whitcomb and others.

Byzantine Aila

The Roman Aqaba Project directed by S. Thomas Parker (North Carolina State University) excavated a monumental mudbrick structure heavily damaged by successive earthquake faulting in Aqaba (in excavation Area J-East), between 1994 and 2003. A collaborative study of the excavated evidence from this area identified a sequence of seven earthquakes that have ruptured the fault since the 2nd Century A.D. (Thomas *et al.*, 2007).

Previous excavations of the monumental Byzantine mudbrick structure indicate that a portion of this building collapsed in the earthquake of May 19, 363 A.D. This date is derived from over 100 coins of Constantius II (337-361 A.D.) found beneath a thick layer of collapsed mudbrick walls. Our detailed mapping of the excavated Early Byzantine walls revealed ancient repair work over seismically-induced structural wall failures. The structural repairs of the Church walls indicate that the southwest corner of the building subsided. This damage may have

occurred in a minor earthquake (perhaps a significant foreshock) prior to the major earthquake that collapsed the structure. Based on subsidence across the fault location, changes in floor elevations, and layers of collapsed mudbrick, the archaeological data suggest that the site was ruptured in an early 2nd Century earthquake, an early 4th Century earthquake, and the 363 A.D. earthquake. The monumental use of the structure was converted to domestic use in the late 4th to early 5th Century.

Figure 6. Faults across the Byzantine mudbrick building in Aqaba. Person is standing by the wall that is faulted. View toward the SW.

We also have evidence for primary ground rupture for at least four post-date 363 A.D. earthquakes that transect the ruins in the J-East area of Aila. Primary fault rupture is documented in stratigraphic sections and plan maps of walls of various construction age (Fig. 6). Two earthquakes occurred during the Late Byzantine to Umayyad period (sith to eighth Century). There is a hiatus of deposition at this location between the Umayyad and the modern age. The two most recent earthquakes, with 42 and 35 cm of dip slip, occurred some time after the 8th Century and may correlate to the historical earthquakes of 1068 and 1212 A.D. No stratified materials were found at this site that could be used to further refine the timing. Our data suggest significant periods of active seismicity (M 6-7) in the 4th, 7th-8th, and probably in the 11th-13th Centuries. These data clearly show that historical earthquake catalogues are incomplete with regard to some of the less damaging earthquakes that have affected southern Jordan but may have played a significant role in the cultural history of the region. The data also document a long period of quiescence since the last phase of intense earthquake activity along the southern Dead Sea transform and highlight the elevated potential earthquake hazard in the region**.**

GEOLOGY FROM AQABA TO PETRA

The mountains east of Aqaba and for a distance of 50 km northeast are Precambrian igneous rocks of the Aqaba Granite Complex (Rashdan, 1988). These igneous rocks are composed of granite, monzogranite, granodiorite, and quartz diorite that developed during the Pan-Arrican orogeny. A series of dikes with widely varying compositions from diabase to felsite cross cut the granitic rocks.

Nonconformably overlying the Aqaba Granite Complex are Paleozoic rocks of the Ram Group (Fig. 7). Cambrian arkosic sandstones and conglomerates derived from the weathered granitic rocks (Salib Formation) form the basal unit. These rocks grade into massive quartzose sandstones of Cambrian to Silurian age (Umm Ishrin and Disi Formations). Outcrops of Lower Paleozoic sandstone are present 50 km northeast of Aqaba along the eastern mountain range. Erosion of the sandstone supplies the sand which has formed extensive dune field within Wadi ‘Arabah to the north.

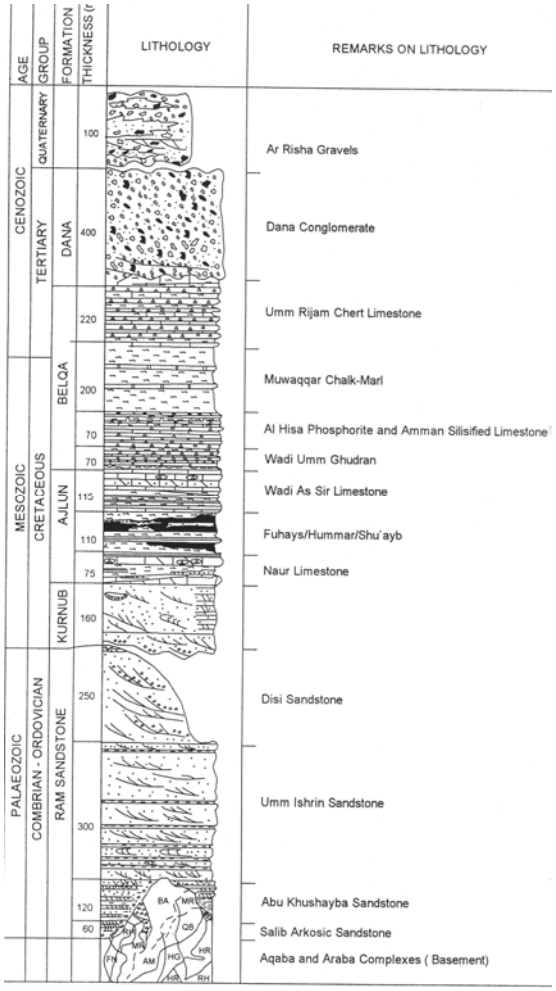

Figure 7. Generalized graphic log of the lithostratigraphic units exposed in Southern Jordan (Barjous, 2003).

The road to Amman crosses the Aqaba Complex rocks within the canyon of Wadi Yutim along part of

the King's Highway—the *Via Nova Traiana* commissioned by Trajan in 111-114 A.D. The walls of the canyon expose the cross-cutting late phases of dike intrusion during the latest Precambrian. Pleistocene terraces line the course of the wadi.

Near the turn-off for Wadi Rum, the valley opens and the contact between the Aqaba Complex and overlying sedimentary sequence is easily discerned. The nonconformity represents an erosional peneplain that is tilted to the east (Abed *et al.*, 1998).

North of Wadi Rum the region of Ras En Naqab is a spectacular area of scenic beauty. The NW-SE trending fault escarpment separates Lower Cretaceous varicolored sandstone and Upper Cretaceous carbonates in the north from the sandstone highlands in the south (Abed *et al.,* 1998). The recent highway improvements in this area expose outcrops of faulted bedrock.

PETRA

Petra, the "Rose City" was the capital of the Nabataeans during the Hellenistic and into the Roman periods. In the Siq of the Petra, you will first pass through the white Disi Sandstone and then the underlying thick red Umm Ishrin sandstone into which most of the monuments were carved (Abed *et al*., 1998). "Following the course of Wadi Musa, the city-center was laid out on either side of the colonnaded street on an elongated plan between the theater in the east and Qasr al Bint in the west. Petra basin boasts over 800 individual monuments that were mostly carved in the Cambrian sandstone by the technical and artistic genius of the Nabataeans" (Barjous, 2003). Some of the most famous antiquities at Petra include al Khazneh (the Treasury), Qasr al-Bint (the free-standing, two-storey building), the Roman Amphitheater, the Great Temple, the Temple of the Winged Lion, and the Petra Church.

Several earthquakes are likely to have caused damage at Petra since it's founding. Josephus Flavius in his *Jewish Wars* describes an earthquake in 31 B.C. that "killed an infinite number of cattle and thirty thousand people" in Palestine (Guidoboni, 1994: 173). Evidence from this early occupation period is scanty because of later monumental construction.

There is evidence of massive destruction in Petra at the Temple of the Winged Lions, at the Great Temple, and other monuments dated to the beginning of the 2nd century A.D. Much scholarly debate has focused on the interpretation of the destruction in light of sparse and rather enigmatic documentary evidence for the Trajanic annexation of Nabataea ca. 106 A.D. The lack of historical text leaves open the possibility of multiple interpretations for the destruction horizons. Coins and milestones suggest Arabia was "acquired" rather than gained by military force. Corroborating evidence for a 2nd C. earthquake in the southern Levant has been documented at Nabataean sites in the Negev, Wadi 'Arabah (Arava Valley), and at Aqaba. The coincidence of an earthquake with a documented political transition makes unequivocal interpretation of the archaeological record extremely difficult (Niemi *et al.,* 2006).

Undeniably, Petra sustained significant damage in the May 19, 363 earthquake that affected the region from north of Lake Tiberias to Aqaba in the south. Russell (1980) and Guidoboni (1994: 264-267) provide convincing literary data for the earthquake. Furthermore, coins from 358-361 beneath collapse at the Petra site of Ez-Zantur (Stucky *et al.,* 1990) and Aqaba (Parker, 1999) confirm damage at both sites in the earthquake.

Figure 8. Collapsed columns of the Great Temple at Petra viewed toward the east. The collapse likely dates to late antiquity sometime after the 6th century.

In the Byzantine period, the Urn tomb was modified into a 5th century church. Other churches were constructed through the 6th and 7th centuries as Petra thrived as a Byzantine center. Many Hellenistic- and Roman-era Nabataean building stones and architectural elements are reused in this construction phase. Excavators of the Petra garden and pool complex just east of the Great Temple (Bedal *et al.,* 2007) note that the final destruction there probably occurred in the 6th century, perhaps they hypothesized, by the 551 A.D. However, the source rupture of this earthquake is the Lebanese coast (Elias *et al.,* 2007).

Scrolls found in the Petra Church provide an unprecedented record of Late Byzantine Petra (Feima *et al.,* 2001). The church was destroyed in a fire at the end of the 6th or the beginning of the 7th century. The fire carbonized scrolls that were being stored in the church. The last recorded date on the scrolls is 597 A.D. It is possible that the earthquake that destroyed

Aereopolis (east of the Dead Sea) based on a dedicatory inscription found there that states "Restored in 492 (597-598 C.E.) after the earthquake" (Zayadine, 1971), also caused damage in Petra.

After the fire and into the 7th century A.D., the church ceased to function as an ecclesiastical building, materials were gutted, and the shell of the structure was converted to a domestic complex. Feima *et al.* (2001) noted evidence for two earthquakes in the later phases of the Petra Church—one in the 7th Century and one in the medieval to Ottoman period—at which time no columns remained standing.

REFERENCES CITED

Abed, A.M., Jarrar, G., and Atallah, M., 1998, Geology of Jordan—An overview: 6th Jordanian Geological Conference 5-8 October, 1998, University of Jordan, Amman, Jordan, 12 p.

Al-Homoud A.S. and Tal A.B., 1998, Geotechnical study for evaluating stability and restoration work at the 1,000 year old archaeological site of Ayla, Gulf of Aqaba, Kingdom of Jordan: *Environmental and Engineering Geoscience*, v. 4, p. 103-114.

Al-Tarazi, E., 2000, The major Gulf of Aqaba earthquake, 22 November 1995—maximum intensity distribution: *Natural Hazards*, v. 22, p. 11-27.

Al-Tarazi, E., and Korjenov, A.M., 2007, Archaeoseismological investigation of the ancient Ayla site in the city of Aqaba, Jordan: *Natural Hazards*, v. 42, no. 1, p. 47-66.

Ambraseys N. N., Melville, C.P. and Adams, R.D., 1994, *The Seismicity of Egypt, Arabia, and the Red Sea*.Cambridge University Press, Cambridge, 181 p.

Barjous, M.O., 2003, *The Geology of Petra and Wadi Al Lahyana Area, Map Sheets No. 3050-I and 3050-IV*, National Resources Authority, Geology Directorate, Amman, Jordan, 93 p. Map scale 1:50,000.

Bedal, L.-A., Gleason, K.L., Schryver, J.G., 2007, The Petra garden and pool complex, 2003-2005: *Annual of the Department of Antiquities of Jordan*, v. 51, p. 151-176.

Elas, A., *et al.*, 2007, Active thrusting offshore Mount Lebanon: Source of the tsunamigenic A.D. 551 Beirut-Tripoli earthquake: *Geology*, v. 35, no. 8, p. 755–758.

Feima, Z.T., Kanellopoulos, C., Waliszewki, T., and Schick, R., 2001, *The Petra Church*, P.M. Bikai (ed.), American Center of Oriental Research, Amman, Jordan, 446 p.

Garfunkel, Z., Zak, I., and Freund, R., 1981, Active faulting in the Dead Sea Rift: *Tectonophysics*, v. 80, p. 1-26.

Garfunkel, Z., 1981, Internal structure of the Dead Sea leaky transform (rift) in relation to plate kinematics: *Tectonophysics*, v. 80, p. 81-108.

Guidoboni, E., 1994, *Catalogue of ancient earthquakes in the Mediterranean area up to the 10th century*. Roma, Italy: Istituto Nazionale di Geofisica, 504 p.

Malkawi, A.H., Abdulla, F., and Barakat, A.B., 1999, The Earthquake of November 22, 1995: *Earthquake Spectra*, v. 15, no. 3, p. 711-724.

Mansoor, N.M., 2002, A GIS-based assessment of active faults and liquefaction potential of the city of Aqaba, Jordan: M.S. Thesis, Geosciences Dept., UMKC, 258 p.

Mansoor, N.M., Niemi, T.M., and Misra, A., 2004, A GIS-based assessment of liquefaction potential of the city of Aqaba, Jordan: *Environmental and Engineering Geoscience*, v. 10, no. 4, p. 297-320.

Niemi, T.M., and Smith, A.M., II, 1999, Initial results of the southeastern Wadi Araba, Jordan geoarchaeological study: Implications for shifts in Late Quaternary aridity: *Geoarchaeology*, v. 14, no. 8, p. 791-820.

Niemi, T.M., Thomas, R., and Parker, S.T., 2006, A 2nd century earthquake at the time of the Roman annexation of Nabataea?: *Geological Society of America* annual meeting, Philadelphia, PA, Oct. 22-25, 2006.

Parker, S.T., 1996, The Roman Aqaba Project: Preliminary Report of the 1994 Season, *Annual of the Department of Antiquities of Jordan*. Amman.

Parker, S.T., 1999, Brief notice on a possible early 4th century church at Aqaba, Jordan: *Journal of Roman Archaeology*, *v.* 12, p. 372–376.

Parker, S.T., 2002, The Roman Aqaba Project: Preliminary Report of the 2000 Season. *Annual of the Department of Antiquities*, Amman

Rashdan, M., 1988, *The regional geology of the Aqaba-Wadi Araba area*, Map Sheets No. 3049 III and 2949 II: National Resources Authority, Geology Directorate, Amman, Jordan, 87 p. Map scale 1:50,000.

Reches, Z., 1987, Mechanical aspects of pull-apart basins and push-up swells with application to the Dead Sea transform: *Tectonophysics*, v. 141, p. 75-88.

Rucker, J.D., and Niemi, T.M., 2005, New excavations of the city wall at Islamic Ayla in Aqaba, Jordan: *Annual of the Department of Antiquities of Jordan*, v. 49, p. 501-508.

Russell, K.W., 1980, The earthquake of May 19, A.D. 363: *Bulletin of the American School of Oriental Research*, v. 238, p. 47–64.

Slater, L., and Niemi, T.M., 2003, Detection of active faults along the Dead Sea Transform using ground penetrating radar and implications for seismic hazards within the city of Aqaba, Jordan: *Tectonophysics*, v. 368, p. 33-50.

Stucky, R.A. *et al*., 1990, Schweizer Ausgrabungen in Ez Zantur, Petra Vorbericht der Kampagne 1988: *Annual of the Department of Antiquities of Jordan*, v. 34, p. 249-283.

Thomas, R., Niemi, T.M., and Parker, S.T., 2007, Structural damage from earthquakes in the 2nd-9th Century at the archaeological site of Aila in Aqaba, Jordan: *Bulletin of the American School of Oriental Research*, v. 346, p. 59-77.

Whitcomb, D., 1993, *Oriental Institute Annual Report* 1992-1993/

____, 1994a, Water and Recent Excavations at Aqaba, *The Oriental Institute News and Notes*. University of Chicago.

____, 1994b, A Street and the Beach at Ayla: The Fall Season of Excavations at Aqaba. 1992, *Annual of the Department of Antiquities of Jordan*. V. 39, p. 499-507.

____, 1995, The *misr* of Ayla: New Evidence for the Early Islamic City, *Studies in the History and Archaeology of Jordan V, Amman: Department of Antiquities.*

____, 1997, The Town and Name of 'Aqaba: An Inquiry into the Settlement History from an Archaeological Perspective, *Studies in the History and Archaeology of Jordan* v. 6, Amman: Department of Antiquities.

Wust, H., 1997, *The November 22, 1995, Nuweiba Earthquake, Gulf of Elat (Aqaba): Post Seismic Analysis of Failure Features and Seismic Hazard Implications*: Geological Survey of Israel, Report GSI 3-97, Jerusalem, Israel.

Zayadine, F., 1971, Un séisme a Rabbat Moab (Jordanie) d'apres une inscription Grecque du VIe S., *Berytus*, v. 20, p. 139-141.

Arava valley

22.2.2009

Field leader

Arimatmon

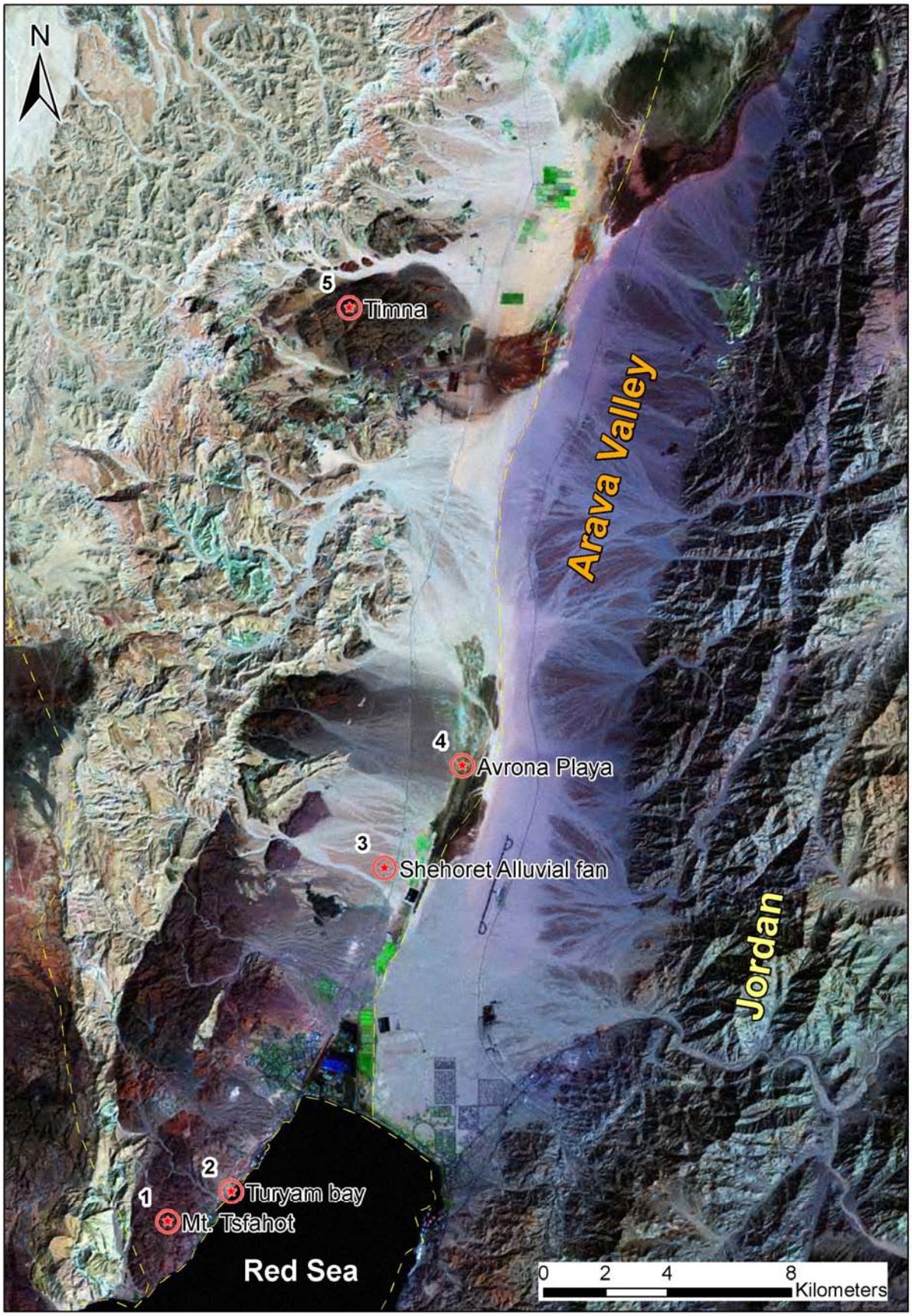
N
5
Timna
Arava Valley
4
Avrona Playa
3
Shehoret Alluvial fan
Jordan
2
Turyam bay
1
Mt. Tsfahot
Red Sea
0 2 4 8
Kilometers

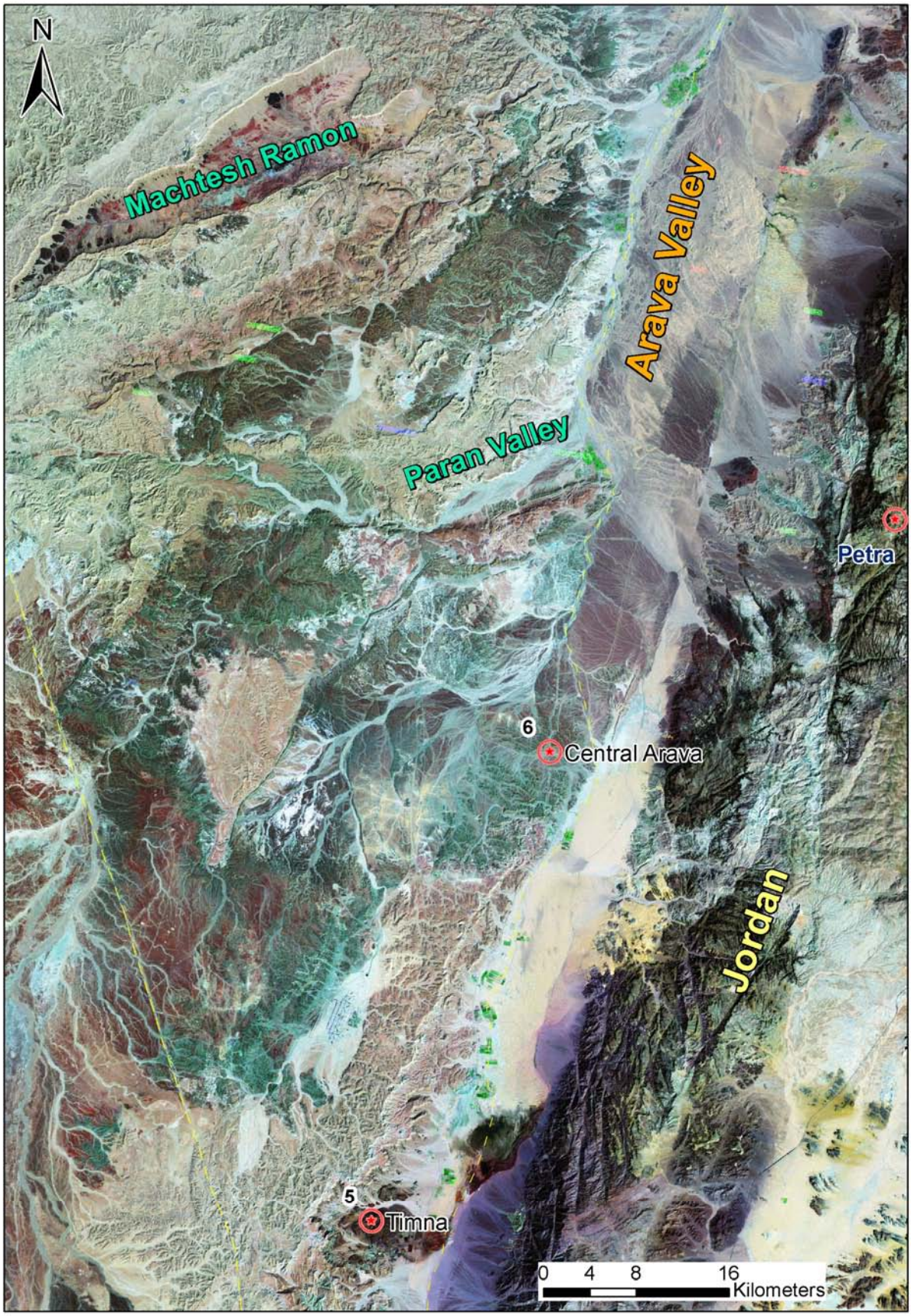
N
Machtesh Ramon
Arava Valley
Paran Valley
Petra
6
Central Arava
Jordan
5
Timna
0 4 8 16
Kilometers

The structure of the western margin of the Dead Sea rift, southern Arava Valley

(modified after Garfunkel et al., 1974, ´ Raham conglomerate – new evidence for Neogene tectonism in the southern part of the Dead Sea Rift) paper attached

The Red Sea Rift splits in the N into the Suez Rift and the Dead Sea Rift (Fig. 1). The southern part of the latter is occupied by the Gulf of Elat (Aqaba). A thick marine Neogene series developed in the Suez Rift attests to its already advanced development in Miocene, and probably in older, times (Hume, 1906; Said, 1962; Robson, 1971). Marine Miocene rocks are also known from the southern tip of the Gulf of Elat (Hume, 1906; Omara, 1959; Bramkamp *et al.*, 1963; Goldberg, (unpub. thesis, Hebrew University of Jerusalem) 1957; see Fig. 1), but these do not bear any direct evidence on the age of the tectonic depression which comprises the Dead Sea Rift. Neogene sediments were not clearly identified nor described from the southern part of the Dead Sea Rift. This led to the belief that the Gulf of Elat, which is much deeper than the Gulf of Suez and bears abundant evidence of young tectonism, was shaped by Quaternary movements only. The southernmost Neogene basin within the Dead Sea Rift, located more than 100 km N of the Gulf of Elat, is filled with continental sediments of the Hazeva Formation (Bentor & Vroman, 1957; Garfunkel & Horowitz, 1966).

This work describes a newly discovered group of Neogene sediments around the northern part of the Gulf of Elat, herein called the Raham Conglomerate, which bears direct evidence on the Neogene existence of the southern part of the Dead Sea Rift.

The Raham Conglomerate was deposited subsequent to, and as a result of, the creation of a considerable topographic and structural relief in the Elat region. The retreating Middle (and Late?) Eocene seas left a very subdued relief here and an almost tabular structure, later considerably modified by tectonic movements and by erosion, mainly related to the formation of the Dead Sea Rift. The formation of the deformed Raham Conglomerate is related herein to the early stages of the formation of the Rift Valley during the Neogene.

The existence of a considerable topographic and structural relief when the Conglomerate was formed is indicated by the coarseness of the conglomerates and the nature of the clast-

The occurrence of clasts from different parts of the section requires that they were all exposed side by side, which could result only from tectonic uplifting and subsequent stripping of the overlying sediments. In particular the occurrence of clasts of Precambrian rocks in Nahal Taba indicates that the basement rocks were exposed at least at the same topographic elevation as the Eocene rocks which underlie the Conglomerate. Therefore, S of Nahal Taba the structural relief was at least 1200 m, which is approximately the thickness of the sedimentary cover in this region. If much of the structural relief was achieved by flexures, as it is now, then the structural relief must have been considerably larger, perhaps exceeding 2 km. Analogously, a lesser, though still considerable relief, is also indicated near Ras Burqa.

Precambrian rocks are now exposed W of the northern part of the Gulf of Elat in a narrow strip, due to uplifting along the margins of the rift valley. The older outcrops could not have been larger, and rocks similar to the clasts in the Raham Conglomerate are exposed there. It is therefore assumed that the development of the border structures of the rift in this region was well under way when the Raham Conglomerate was deposited, possibly as a syntectonic sediment.

The angular unconformities at the base of the Raham Conglomerate suggest still older tectonism, but since the various outcrops are probably not strictly contemporaneous, an older and distinct phase cannot be demonstrated.

Later movements deformed the Conglomerate, and erosion stripped the rock formations which supplied the clasts of the Conglomerate from most of the area. In particular Senonian to Eocene rocks, which were still abundant in the Elat region when the Raham Conglomerate was formed, are now virtually completely eroded, except in few structural lows. It is most probable that considerable volumes of the Raham Conglomerate itself were also eroded.

The bulk of the Conglomerate is probably fluviatile and lacustrine, but the occurrence of marine beds indicates that an arm of the sea, conveniently termed the 'ancestral' or 'proto' Gulf of Elat, reached as far N as the Elat region. This further corroborates the conclusion that the depression of the Dead Sea Rift was already well outlined when the Raham Conglomerate was deposited. This old Gulf probably did not communicate with the Mediterranean, but only with the Red Sea. Marine Neogene sediments are well developed at the southern end of the Gulf of Elat (see Fig. 1, and Omara, 1959; Bramkamp *et al.*, 1963; Goldberg, 1957, see Introduction above), but they do not clearly prove the existence of a Neogene Gulf. The few fossil occurrences and the tectonic position indicate a Neogene age for the Raham Conglomerate.

Additional information can be derived from consideration of the relations of the Raham Conglomerate with continental sediments preserved on the plateau W of the Gulf of Elat (Fig. 1).

These sediments belong to the higher parts of the Hatzeva Formation and contain conglomerates of extremely well-rounded pebbles, mainly of chert and quartzites, of the type known as the 'cover conglomerate' (Bentor & Vroman, 1957; Garfunkel & Horowitz, 1966). These conglomerates were transported over distances exceeding 150–200 km, and in the N interfinger with marine sediments of Late Miocene or earliest Pliocene age (Reiss & Gvirtzman, 1966).

The conglomerates in the higher parts of the Hazeva Formation are probably only broadly contemporaneous, but they do seem to record a definite episode when a well-integrated drainage system crossed the entire Negev and debauched into the Mediterranean in the Beer Sheba region.

For the present purpose the following observations are important:

(a) The 'cover conglomerate' was transported across the outcrops of the Raham Conglomerate west of Elat (Fig. 1).

(b) The 'cover conglomerate' was deposited on rocks of the Judea Group or on down-faulted younger rocks; the field relations indicate that by that time the Eocene rocks had already been virtually completely eroded away from the region west of Elat, and the Senonian rocks were also largely eroded.

(c) The virtual total absence of clasts of local derivation, and the great distances of transport of the clasts of the 'cover conglomerate' indicate a generally subdued, plateau-like landscape. In fact, the region N of Sheikh Atiya still largely retained this physiography.

These features suggest that the Raham Conglomerate, except perhaps the uppermost parts of the section near Ras Burqa, is older than the 'cover conglomerate' in this region, and that a period of extensive erosion intervened between the two. Thus the Raham Conglomerate may be of Middle Miocene or even older age.

It should be stressed that the very characteristic clast assemblage of the 'cover conglomerate' was not found in any of the outcrops of the Raham Conglomerate or anywhere else in the rift valley within a distance of 150 km N of Elat. It seems that the interior of the rift valley in the Elat region was already separated by a watershed from the drainage of the plateau W of it, similar to the present situation.

The Raham Conglomerate is probably roughly equivalent to the basal conglomerate and lower parts of the Hazeva Formation of the Central Arava and Northern Negev, which are older than the 'cover conglomerate' (Bentor & Vroman, 1957). This is suggested not only by the relations in the Elat region discussed above, but also by:

(a) general lithologic similarity;

(b) similar tectonic position, namely deposition in the first morphotectonic or topographic depressions to be formed along the borders of the Dead Sea Rift, and probably also inside the rift valley.

A new formational name is suggested herein for the southern conglomerates because they were deposited in a separate basin or in several basins which were related to the Gulf of Elat. On the other hand, the Hazeva Formation was related to a northward flowing drainage system and to a basin in the Central Arava. Thus it seems that the two groups of sediments record somewhat different histories.

It seems that the Raham Conglomerate is also generally correlative with the 'Untere Syntektonische Konglomerate' of southern Jordan which occurs in similar structural circumstances, and possibly also with an outcrop of marine Neogene beds at Gebel Hureij, all of which were described by Bender (1968).

Summarizing, the Raham Conglomerate records a Middle Miocene or older phase of deposition which was related to early movements in the southern half of the Dead Sea Rift. A morpho-tectonic depression was already developed and it was partly occupied by the 'proto' Gulf of Elat, which communicated with the Red Sea. The structural relief in some parts of the border structures of the rift exceeded 1.2 km, and probably even 2 km.

The major erosion of the rift margins which ensued in response to the deepening of the rift valley had not yet occurred when the Raham Conglomerate was formed, and the cover of Eocene rocks was still largely preserved in the Elat region. The deposition of the Raham Conglomerate in fact records part of this erosion, which was already very advanced by the time of the deposition of the 'cover conglomerate' (Latest Miocene or Early Pliocene) of the Hazeva Formation.

Later tectonism greatly deformed the Raham Conglomerate and eventually shaped the present form of the rift valley.

Plate arrangement in the eastern Mediterranean region

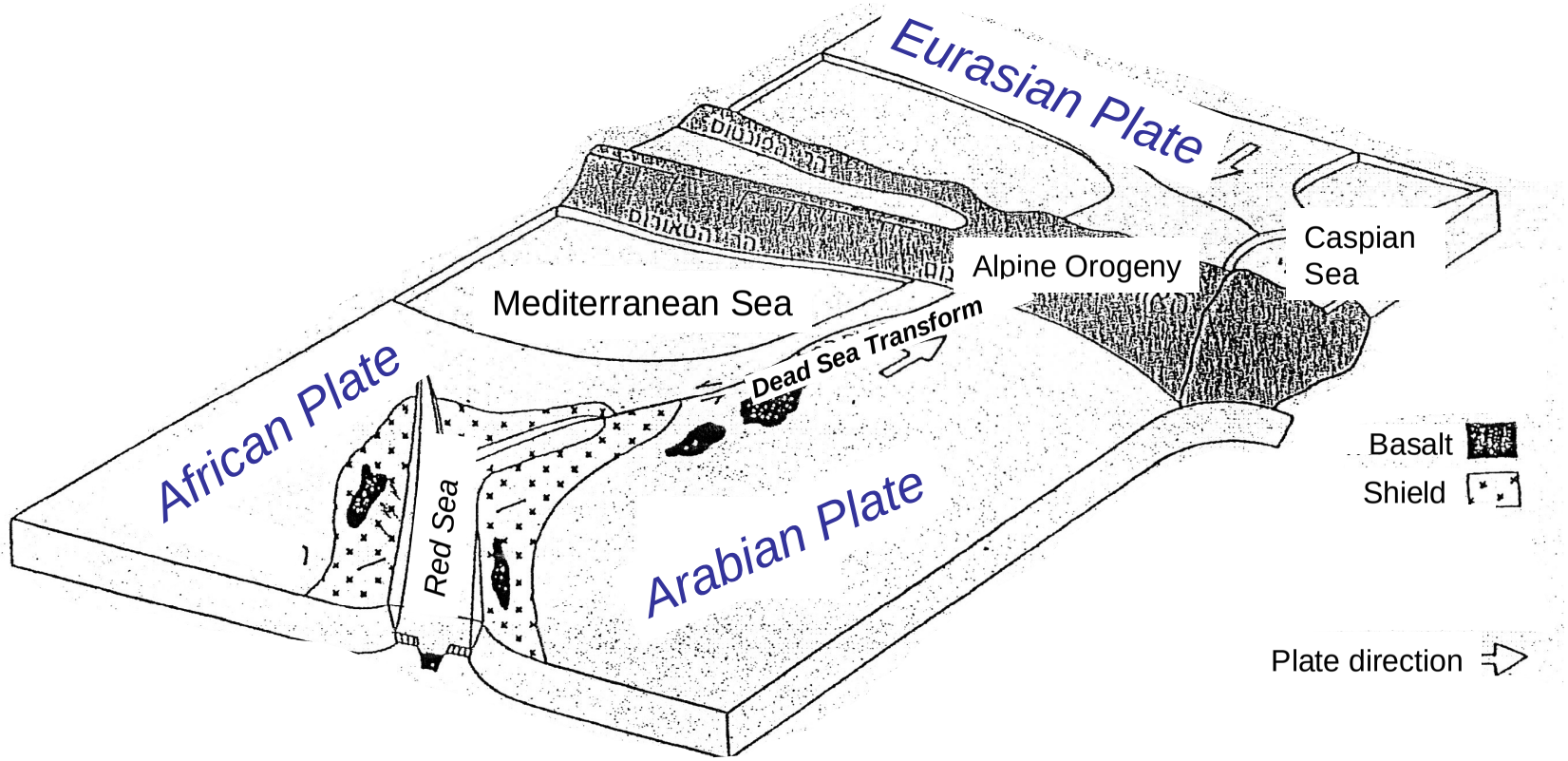

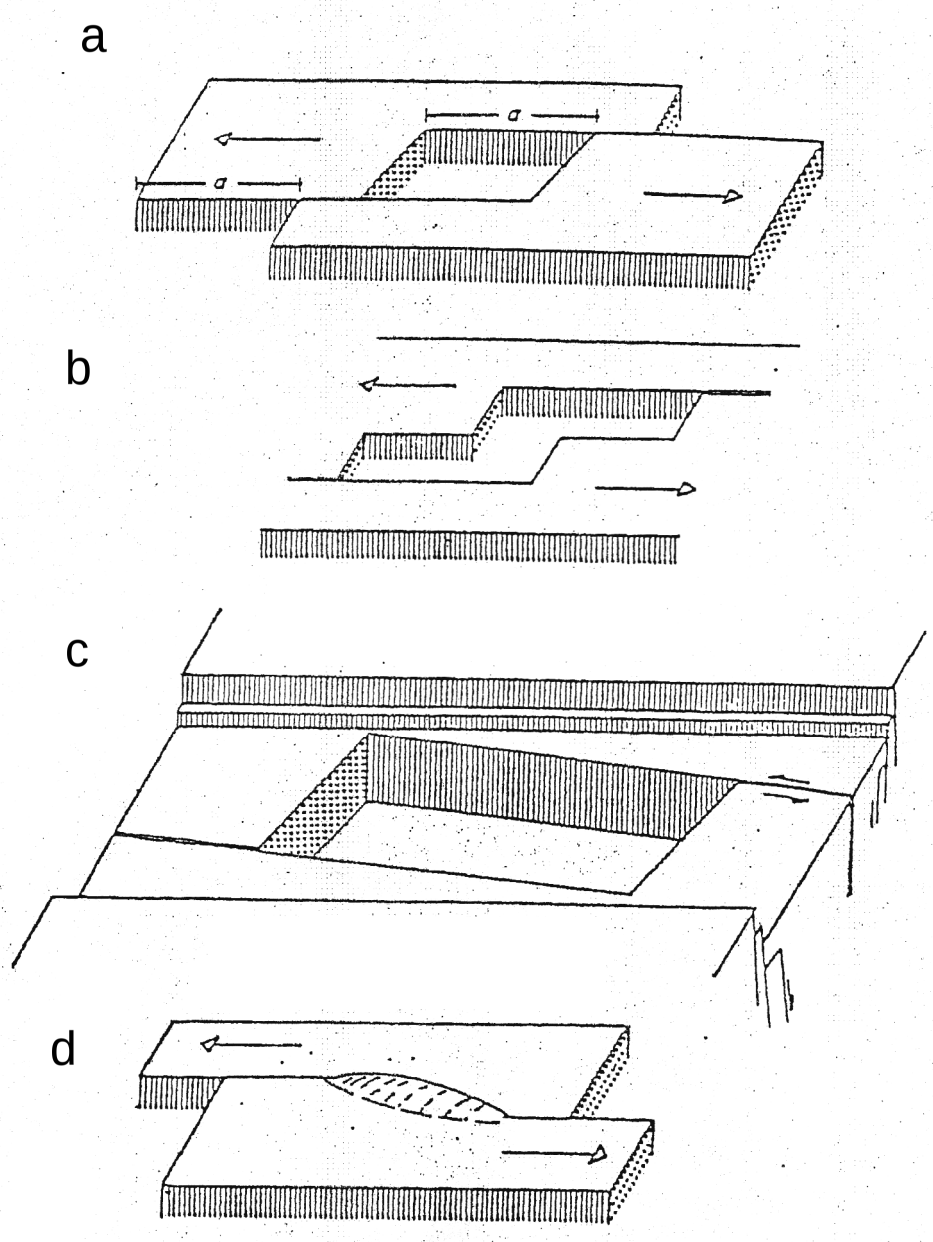

Garfunkel, 1981

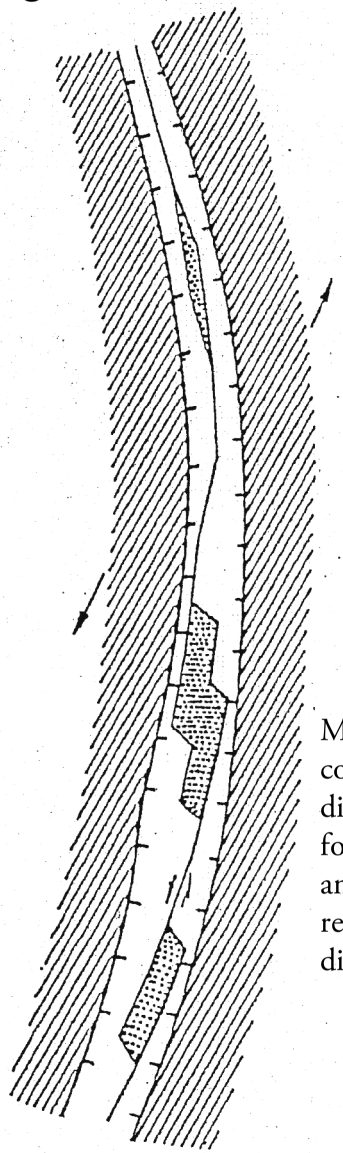

Motion along the Dead Sea fault is composed of lateral and normal displacement. This combination forms deep rhomb shaped grabens and push ups within a rift valley as a result of shift in the plate boundary direction.

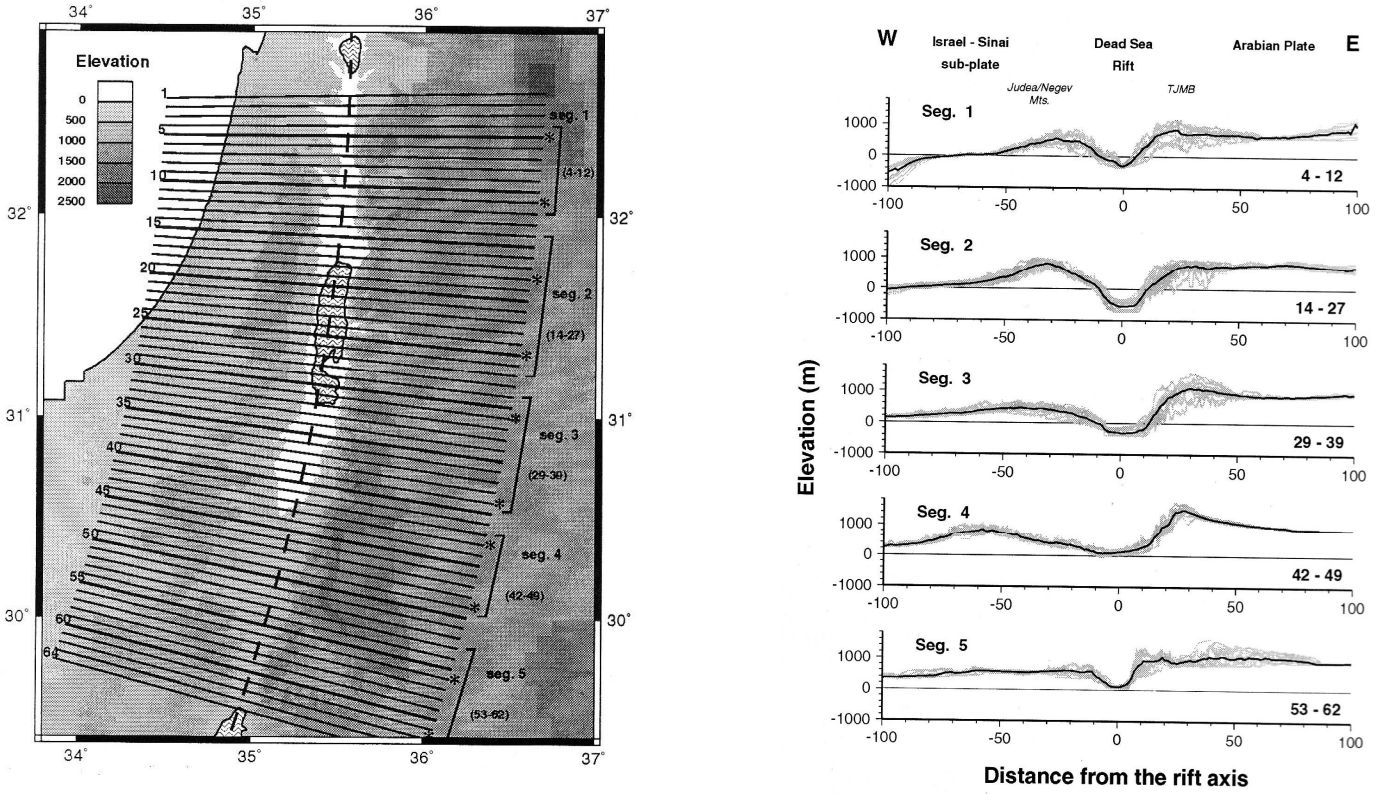

Wdowinski and Zilberman, 1997

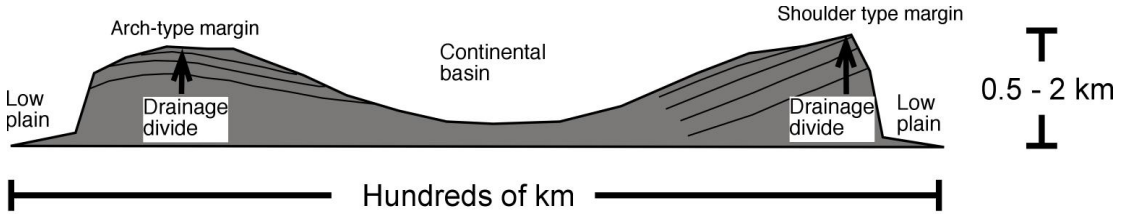

Generalized continental margin geometry modified from Ollier (1984). *Shoulder-type margins* are those where the uplift axis is located at the edge of the uplifted domain. Along these margins, the drainage divide is coincident with the top of the escarpment. *Arch-type margins* are those where the uplift axis is located inland from the edge of the uplifted domain. Along these margins, the drainage divide is separated from the top of the escarpment (Matmon et al., 2002).

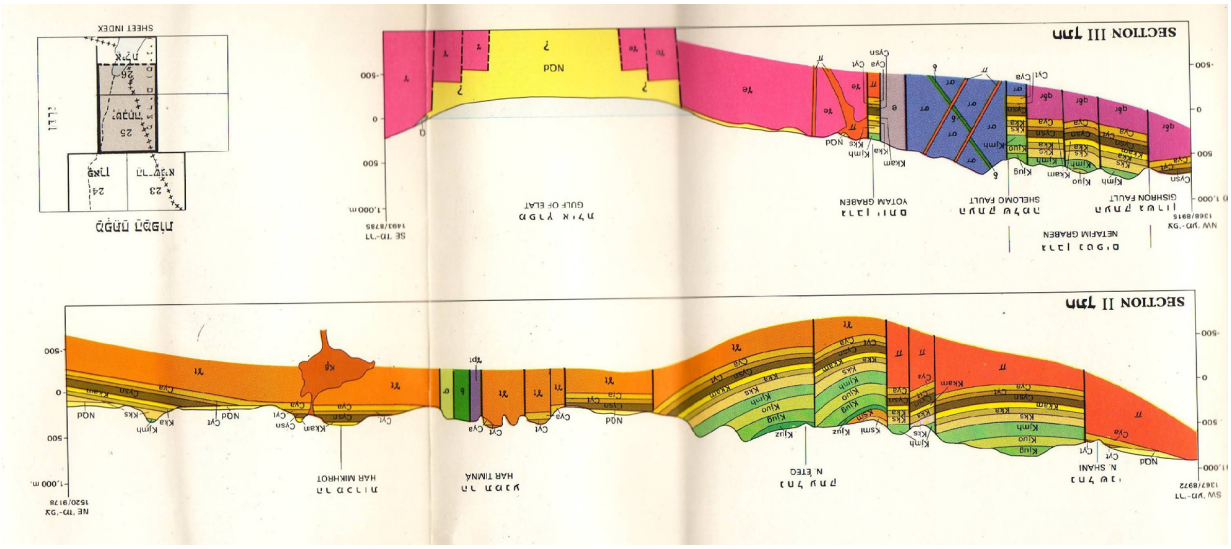
SECTION III
SECTION II
SHEET INDEX
GULF OF ELAT
YOTAM GRABEN
SHELOMO FAULT
SHIHON FAULT
NETAFIM GRABEN
HAR NIKHROT
HAR TIMNA
N. ETEC
N. SHANI

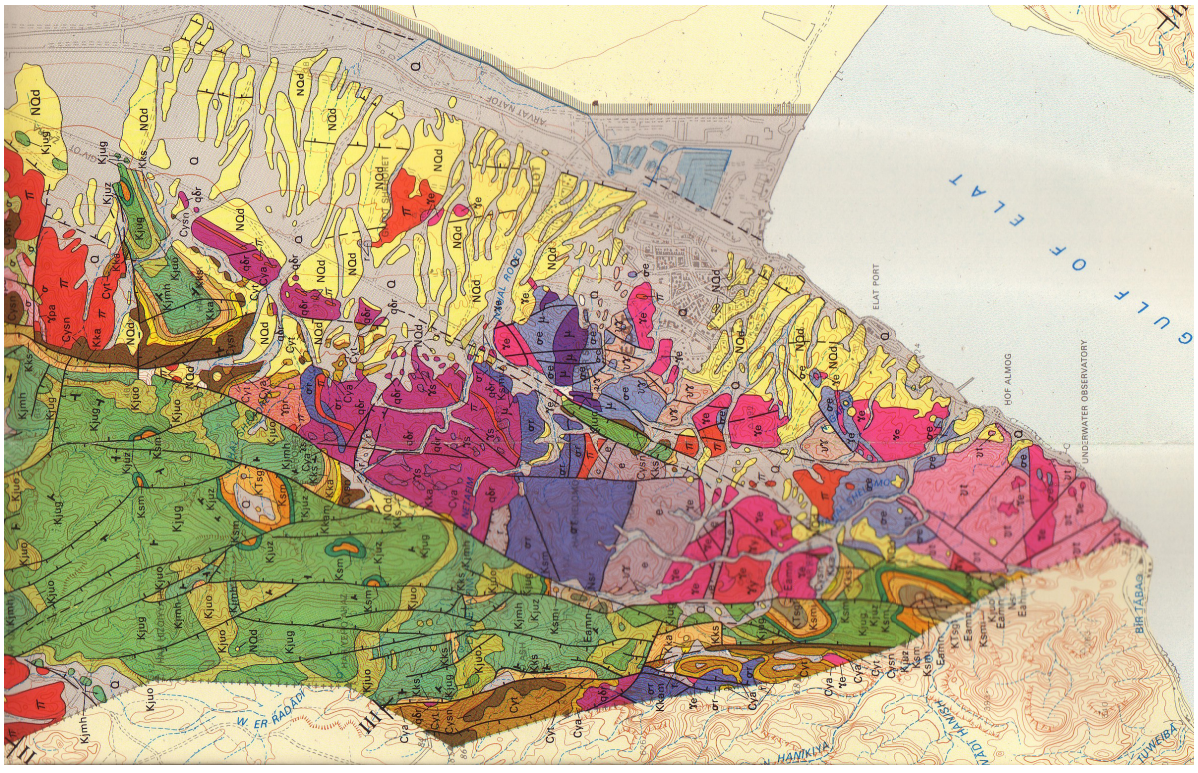
GULF OF ELAT
ELAT PORT
HOF ALMOG
UNDERWATER OBSERVATORY
W. ER RADADI
HANIKLYA
TUWEIBA

Geodetic and Geophysical Background of the Arava Valley

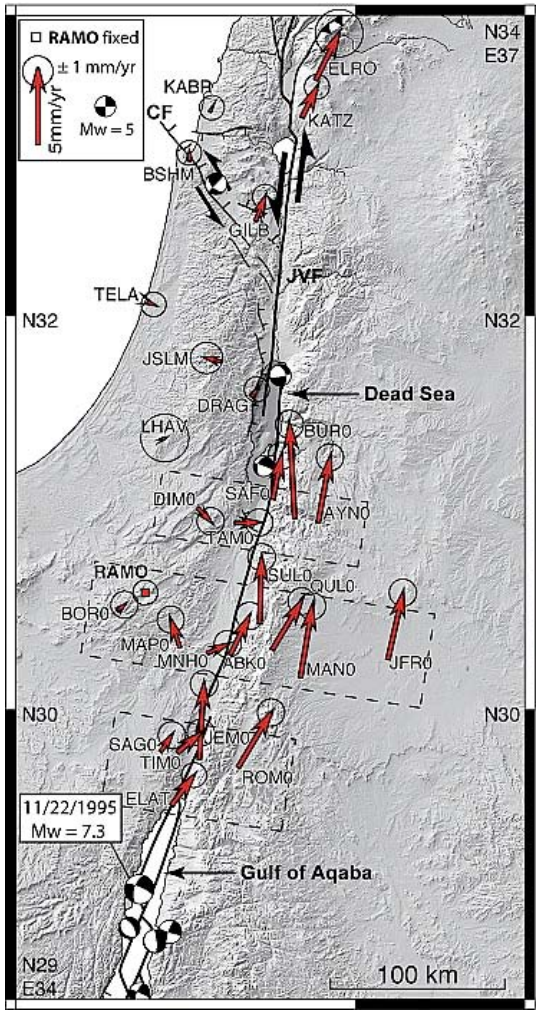

Figure 1: Tectonic map and horizontal velocity field plotted relative to site RAMO. Also shown focal mechanisms of events with ML > 5 that occurred since 1976 (USGS (http://www.seismology.harvard.edu) and GII (http://www.gii.co.il) databases). Le Beon et al., 2008.

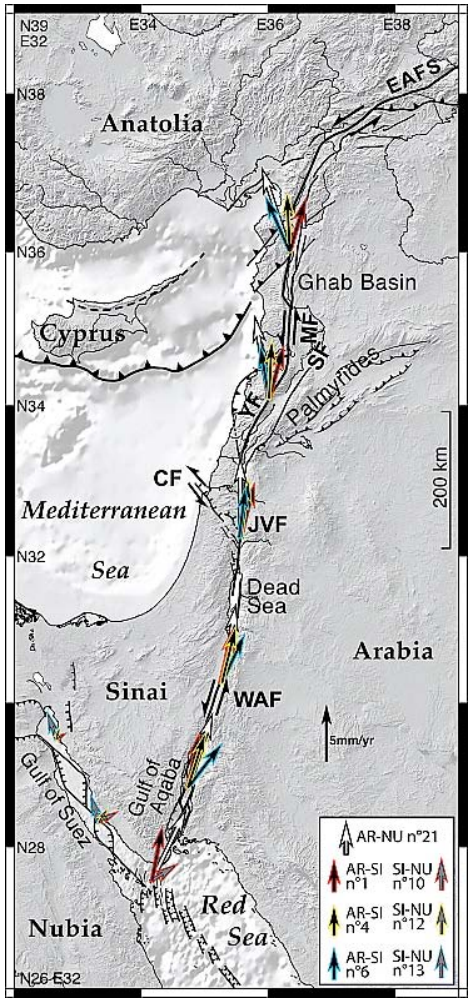

Figure 2: Regional kinematics predicted by selected Euler vectors. AR, Arabia; NU, Nubia; SI, Sinai. Pole numbers refer to Tables 4, 5a, and 5b. EAFS, East Anatolian fault system; WAF, Wadi Araba fault; JVF, Jordan Valley fault; CF, Carmel fault; YF, Yammouneh fault; SF, Serghaya fault; MF, Missyaf fault. Le Beon et al., 2008.

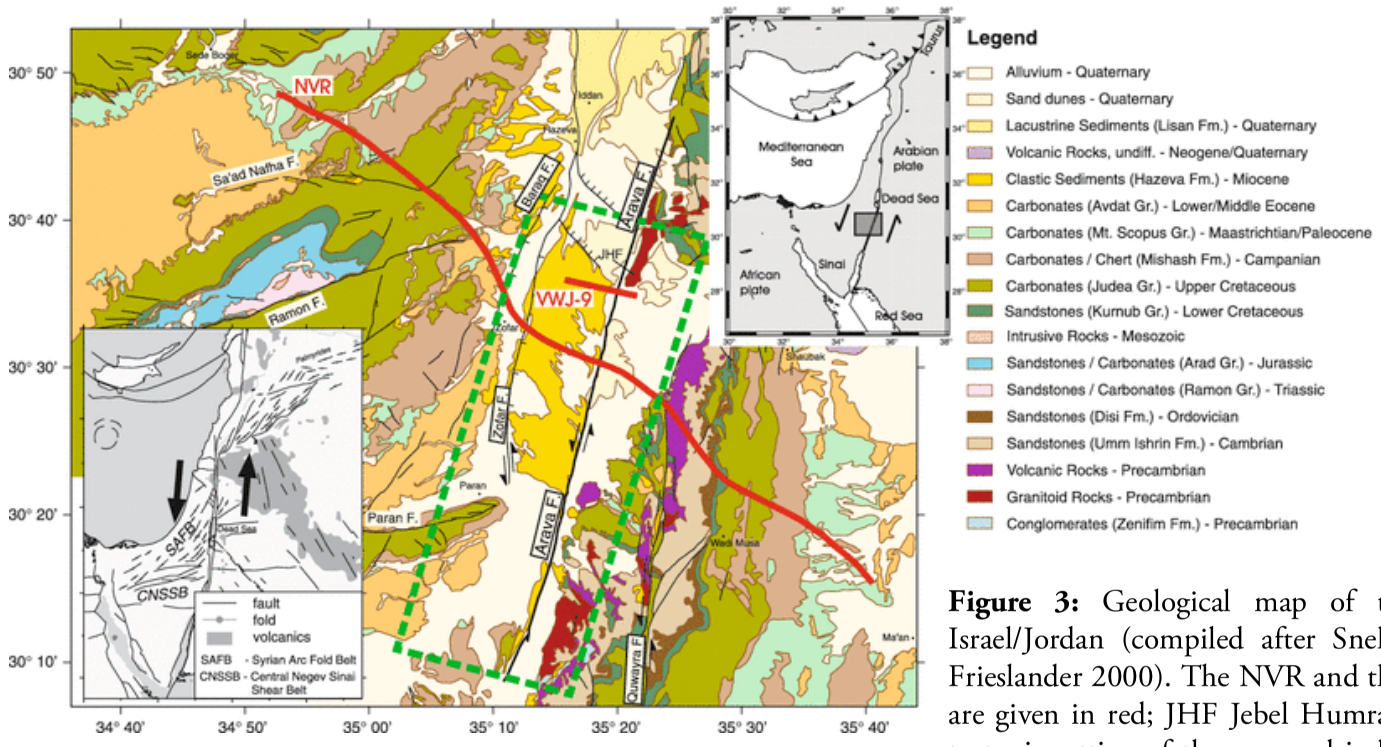

Figure 3: Geological map of the central Arava/Araba Valley in Israel/Jordan (compiled after Sneh et al. 1998; Bender et al. 1968; Frieslander 2000). The NVR and the VWJ-9 common depth point lines are given in red; JHF Jebel Humrat Fiddan. The right inset shows the tectonic setting of the area and indicates the left lateral displacement of 105 km. The left inset shows information on some major tectonic elements in the Dead Sea region (after Sneh et al. 1998). The green dashed box indicates the area of subsequent figures. Kesten et al., 2008.

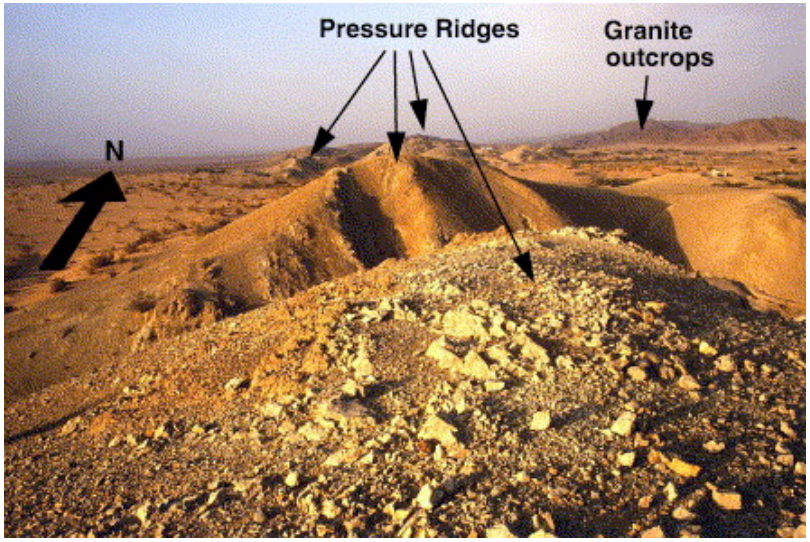

Figure 4: View of the pressure ridges in the northern part of Haberland et al.'s (2007) study area. View toward the North.

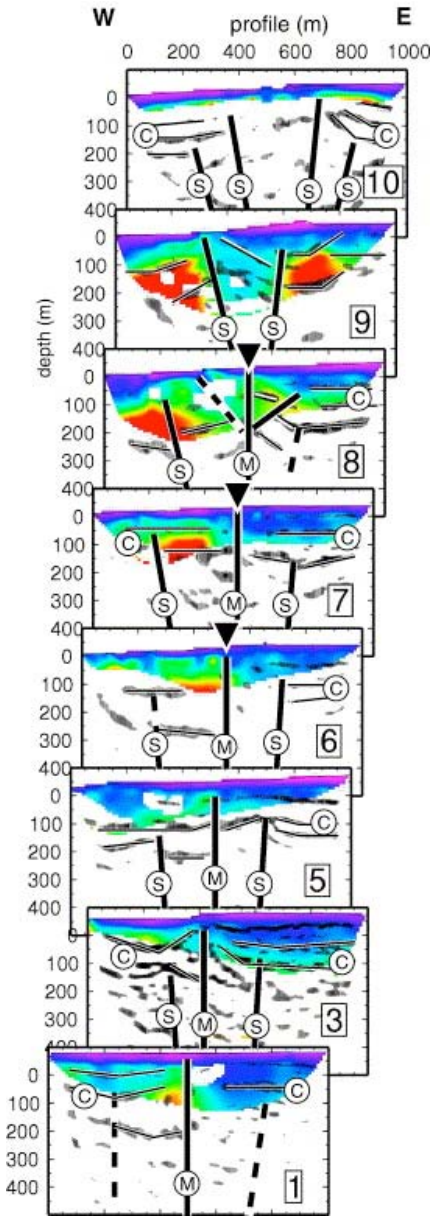

Figure 5: (left) Migrated reflection seismic images (black wiggles) overlaid on the tomography (color coded) together with our geological interpretation. Black thick lines indicate inferred faults, dashed lines indicate less well constrained faults. M), S), and C) indicate the main fault, secondary/flanking faults, and sedimentary cover at the two sides, respectively. Inverted triangles indicate the position of guided wave observations from (Haberland et al., 2003).

(right) A) Summary of all interpreted sections along the fault (perspective view from the South). The main fault is indicated by the red area. B) Possible reconstruction of the fault structure based on the seismic results. A few subparallel faults form the WAF system in the study area; to the North the pressure ridge structure dominates. Covering sediments are omitted.

Haberland et al., 2007.

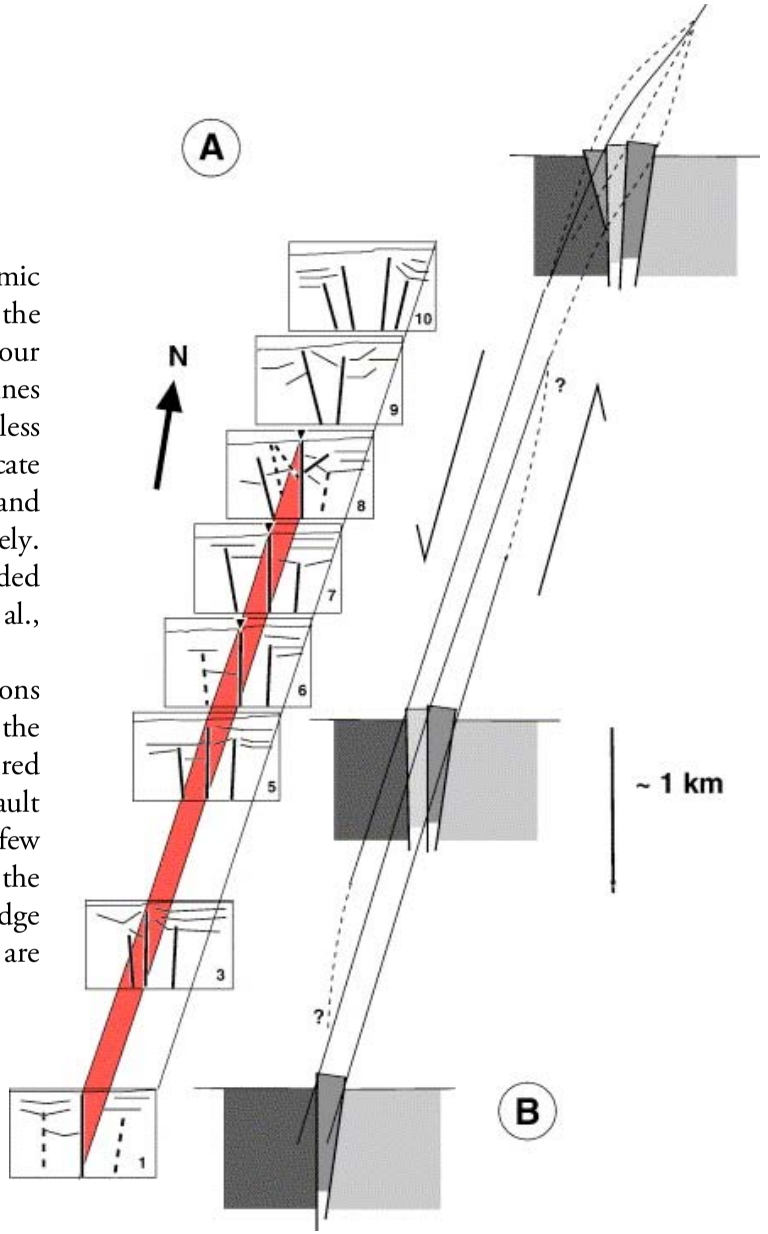

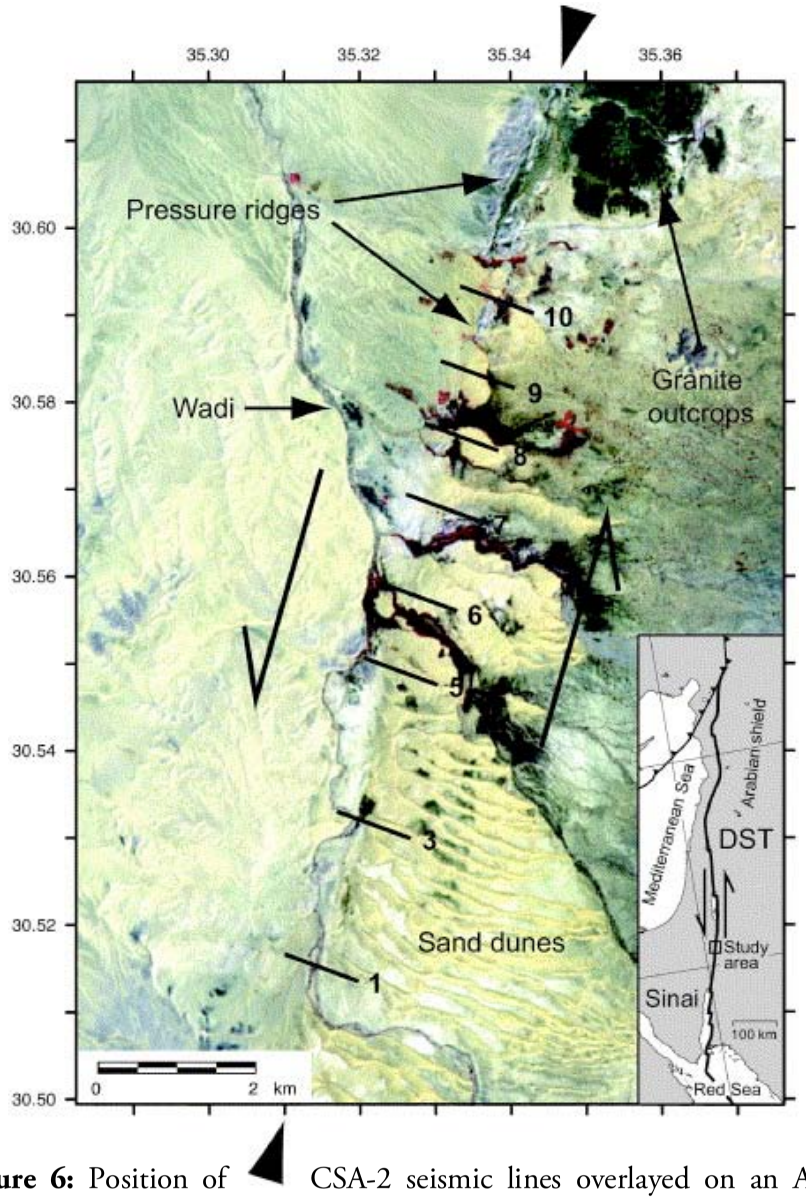

Figure 6: Position of CSA-2 seismic lines overlayed on an ASTER satellite image of the study area. Large arrowheads mark the course of the Wadi Araba fault (WAF). The inset shows the principal geotectonic situation in the Middle East. Haberand et al., 2007.

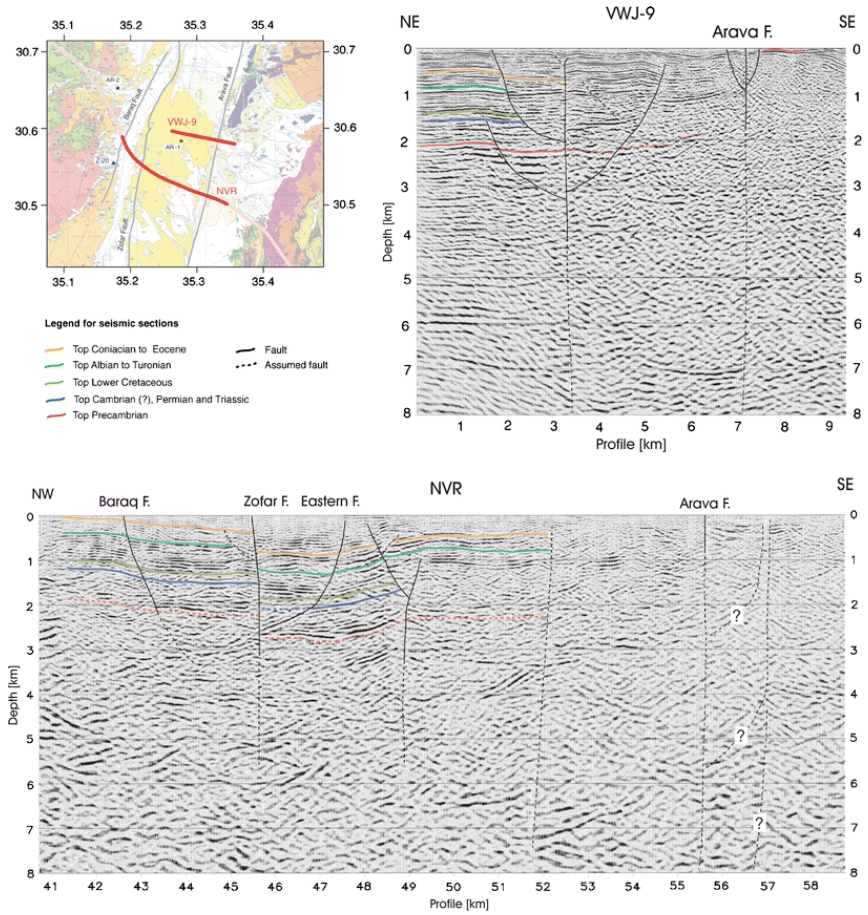

Figure 7: Near-surface structure as seen in seismic reflection data. a Location of seismic profiles NVR and VWJ-9; Z-20: Zofar-20 well; AR-1 and AR-2: outcrops of Arava/Araba Formation. b Depth migrated shallow seismic reflection profile VWJ-9 (Kesten 2004). c Upper central part of the depth migrated NVR profile, only the range indicated in full red is shown (see Fig. 2a, profile km 40.5–58.5). Kesten et al., 2008

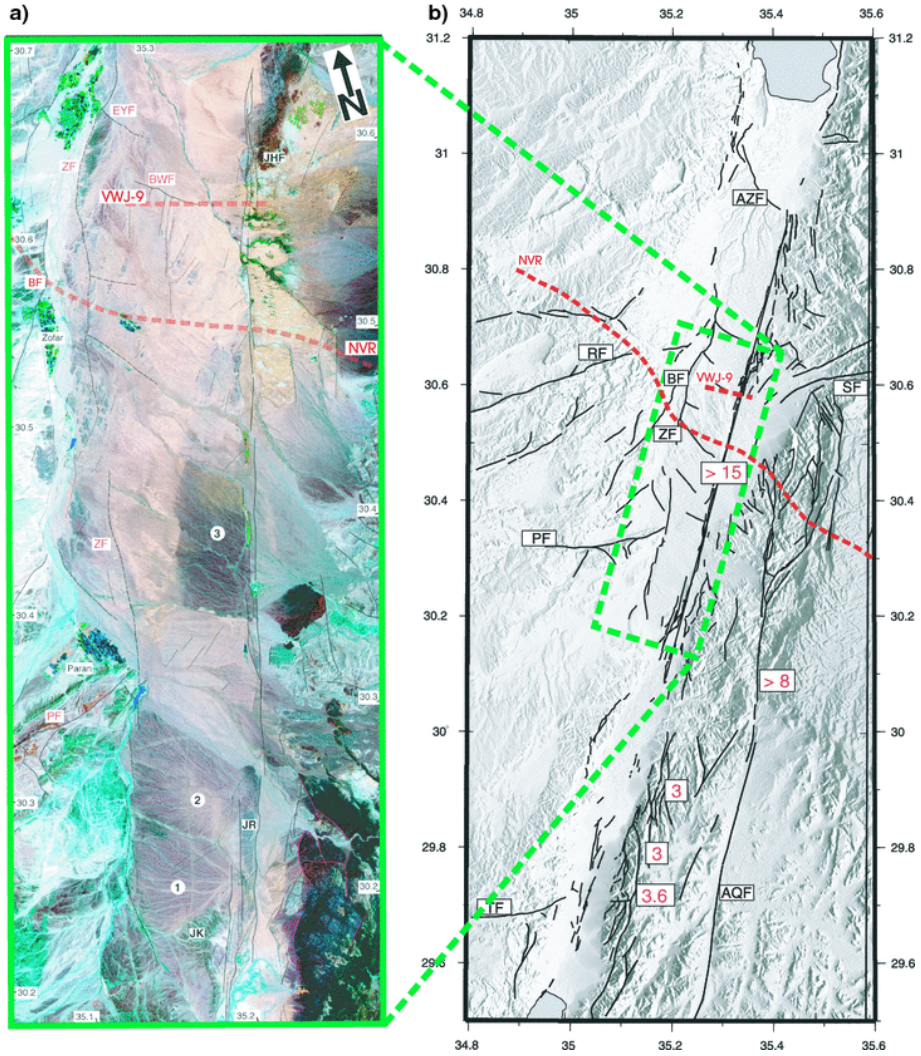

Figure 8: An ASTER scene of the central Arava/Araba Valley taken on April 6, 2001. Three types of lineaments can be distinguished: (1) Solid lines represent lineaments that are clearly recognized as faults (by displaced geological units, offset alluvial fans or clear 'doglegs' of streams); (2) Dashed lines are used for lineaments that were identified as faults in other, mainly shallow seismic studies (e.g. Frieslander 2000); (3) Dotted lines are lineaments whose origin could not be clarified for lack of geological or geophysical information. EYF En Yahav Fault, BWF Buweirida Fault, ZF Zofar Fault, BF Baraq Fault, PF Paran Fault, JHF Jebel Humrat Fidan, JR Jebel Er Risha, JK Jebel El Khureij and numbers 1–3 indicate alluvial fans; b Fault map of the southern Dead Sea Transform, derived from the interpretation of ASTER satellite images (Kesten 2004 and this study) over the shaded relief map. The red numbers indicate the minimum amount of left-lateral strike-slip displacement along the respective faults in kilometres. AQF Al Quwayra Fault, AZF Amaziahu Fault, BF Baraq Fault, PF Paran Fault, RF Ramon Fault, SF Salawan Fault, TF Themed Fault and ZF Zofar Fault. Here, the nomenclature of Frieslander (2000) and Calvo and Bartov (2001) is used.

Kesten et al., 2008

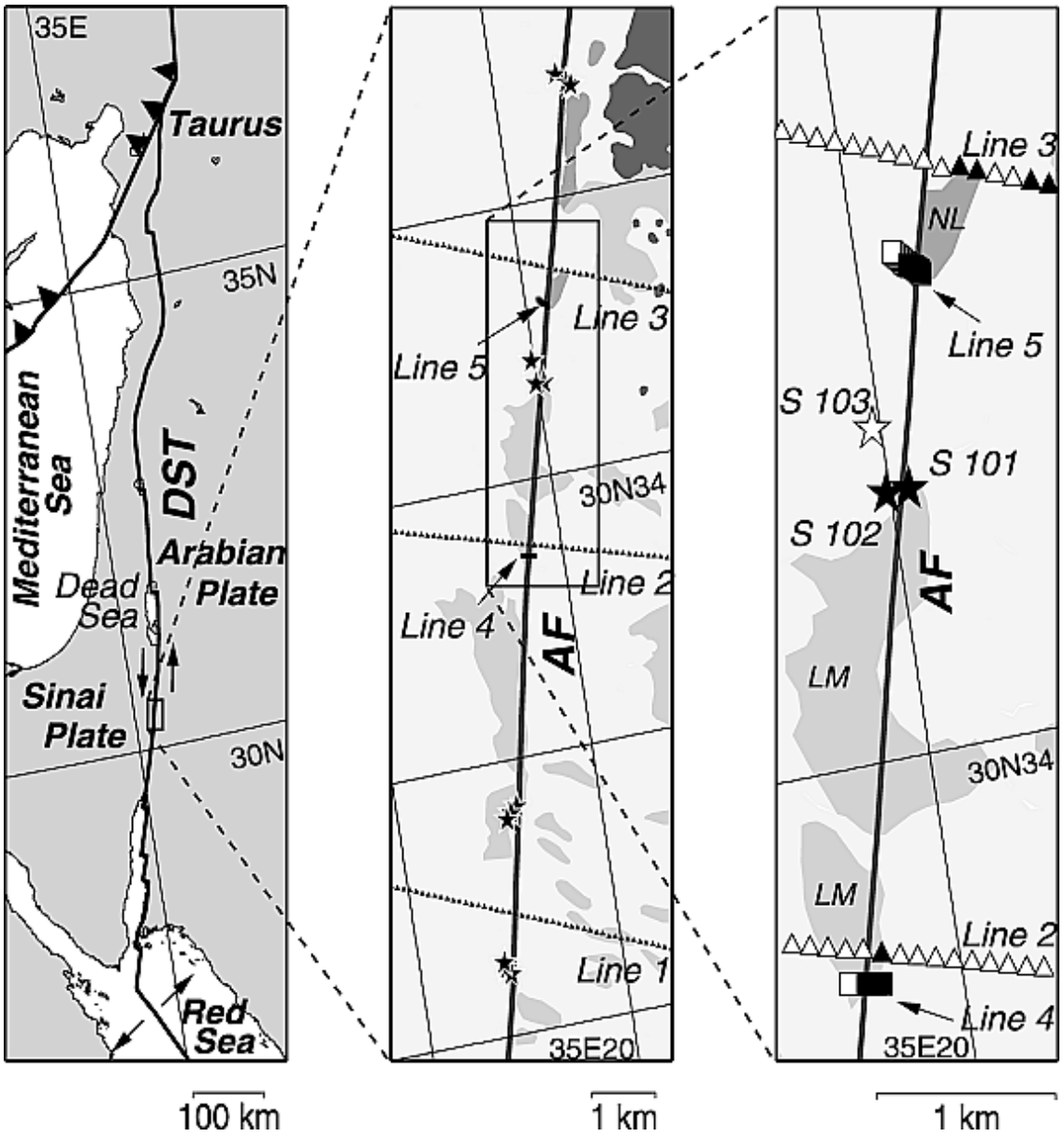

Figure 9: (left) Sketch showing the tectonic setting of the Middle East. (middle) Site map of the active seismic experiment at the Arava Fault (AF) as part of the Dead Sea Transform (DST). Fault trace (dark shaded line) as inferred beneath superficial deposits. Shots are denoted by stars. Vertical sensors on lines 2 and 3 (spacing 100 m) are shown by triangles, and three-component sensors along lines 4 and 5 (spacing 10 m) are shown by squares. (right) Close-up of the region displayed in the middle panel. Solid symbols (stars, triangles, and squares as before) indicate shots generating and receivers observing guided waves; open symbols indicate shots and receivers without such generation or observation, respectively. Geology adopted from Rabb'a [1994] (NL, Na'ur limestone; LM, Neogene marl).

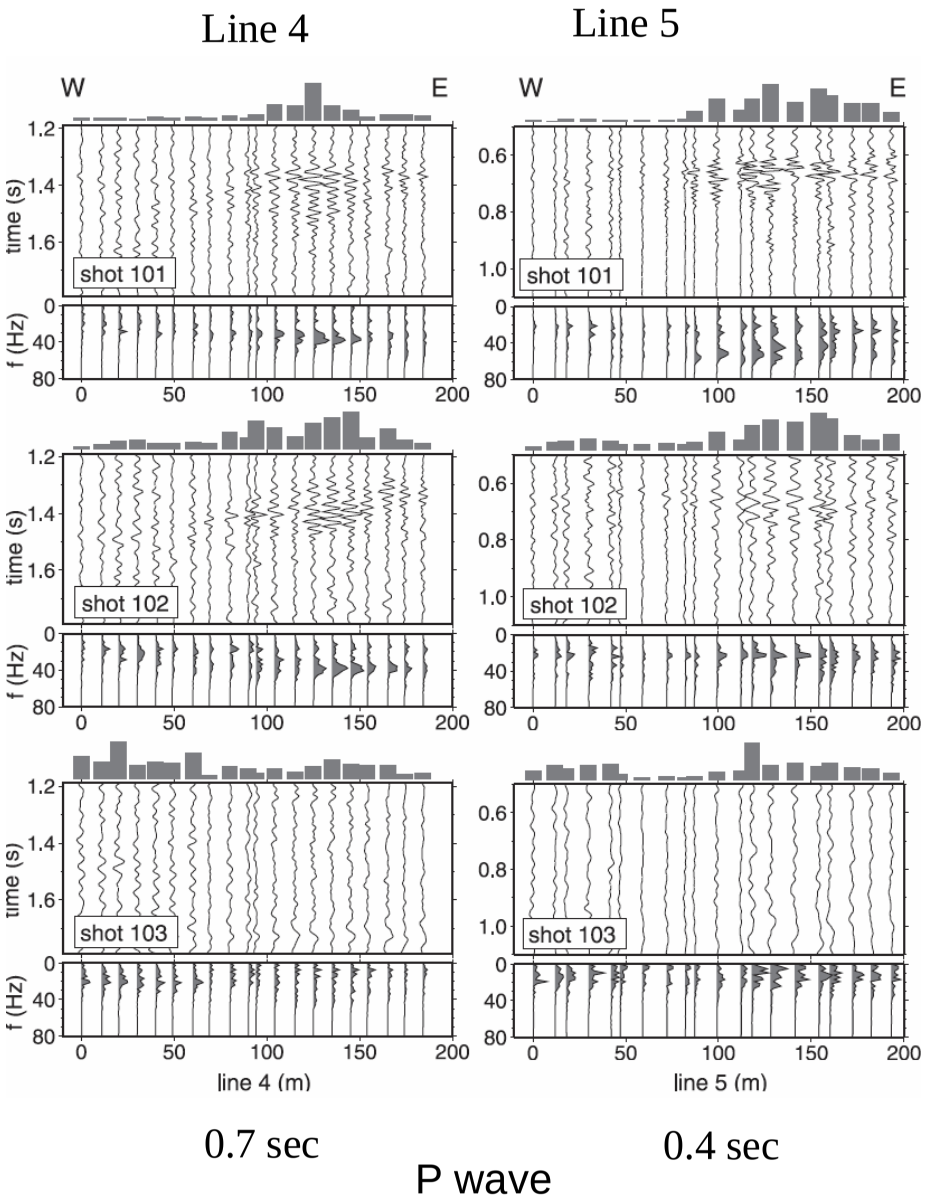

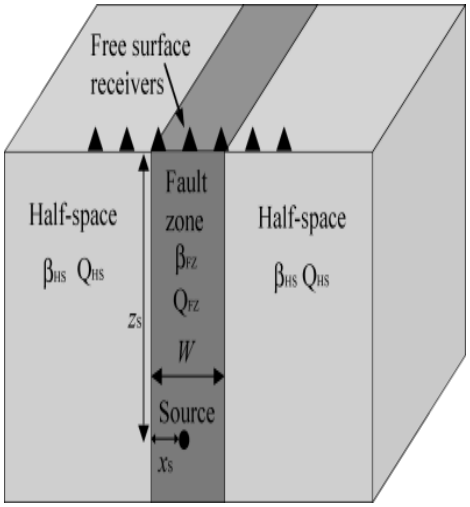

Figure 10: (top) Schematic showing experimental layout. (left) Observations on receiver line 4 (left) and line 5 (right) for the three shots 101 (top), 102 (middle), and 103 (bottom). For each gather, normalized maximum energy (bars, top, within time windows of 1.2 to 1.6 and 0.6 to 0.8 s, respectively), time series (middle), and spectra (bottom) for each trace are shown. Note the high-frequency wave trains from shots 101 and 102 on eastern traces of both lines between 1.3 and 1.6 s (line 4, left) and 0.6 and 0.8 s (line5, right), but no such phase for shot 103 (and all other shots; see text). For positions, refer to map above. Shown are unfiltered vertical component data containing presumed guided waves. P wave onsets (not shown) arrive at around 0.7 s (line 4, left) and 0.4 (line 5, right). Haberland et al., 2003.

References

Haberland C., Agnon , A., El-Kelani , R., Maercklin, N., Qabbani , I., Rumpker, G., Ryberg, T., Scherbaum, F., Weber M., 2003. Modeling of seismic guided waves at the Dead Sea Transform, Jour. Geophys. Res., 108, 2342.

Haberland, Ch., Maercklin, N., Kesten, D., Ryberg, T., Janssen, Ch., Agnon, A., Weber, M., Schulze, A., Qabbani, I., El-Kelani, R., 2007. Shallow architecture of the Wadi Araba fault (Dead Sea Transform) from high-resolution seismic investigations, Tectonophys., 432, 37-50.

Kesten, D., Weber, M., Haberland, Ch., Janssen, Ch., **Agnon, A.**, Bartov, Y., Rabba, I., The DESERT Group, 2008. Combining satellite and seismic images to analyse the shallow structure of the Dead Sea Transform near the DESERT transect, Int J Earth Sci (Geol Rundsch), 97, 153-169.

Le Beon, M., Klinger, Y., Amrat, A. Q., **Agnon**, **A.**, Dorbath, L. , Baer, G., Ruegg, J-C., Charade, O., Mayyas, O., 2008. Slip rate and locking depth from GPS profiles across the southern Dead Sea Transform, J. Geophys. Res., 113, B11403, doi:10.1029/2007JB005280.

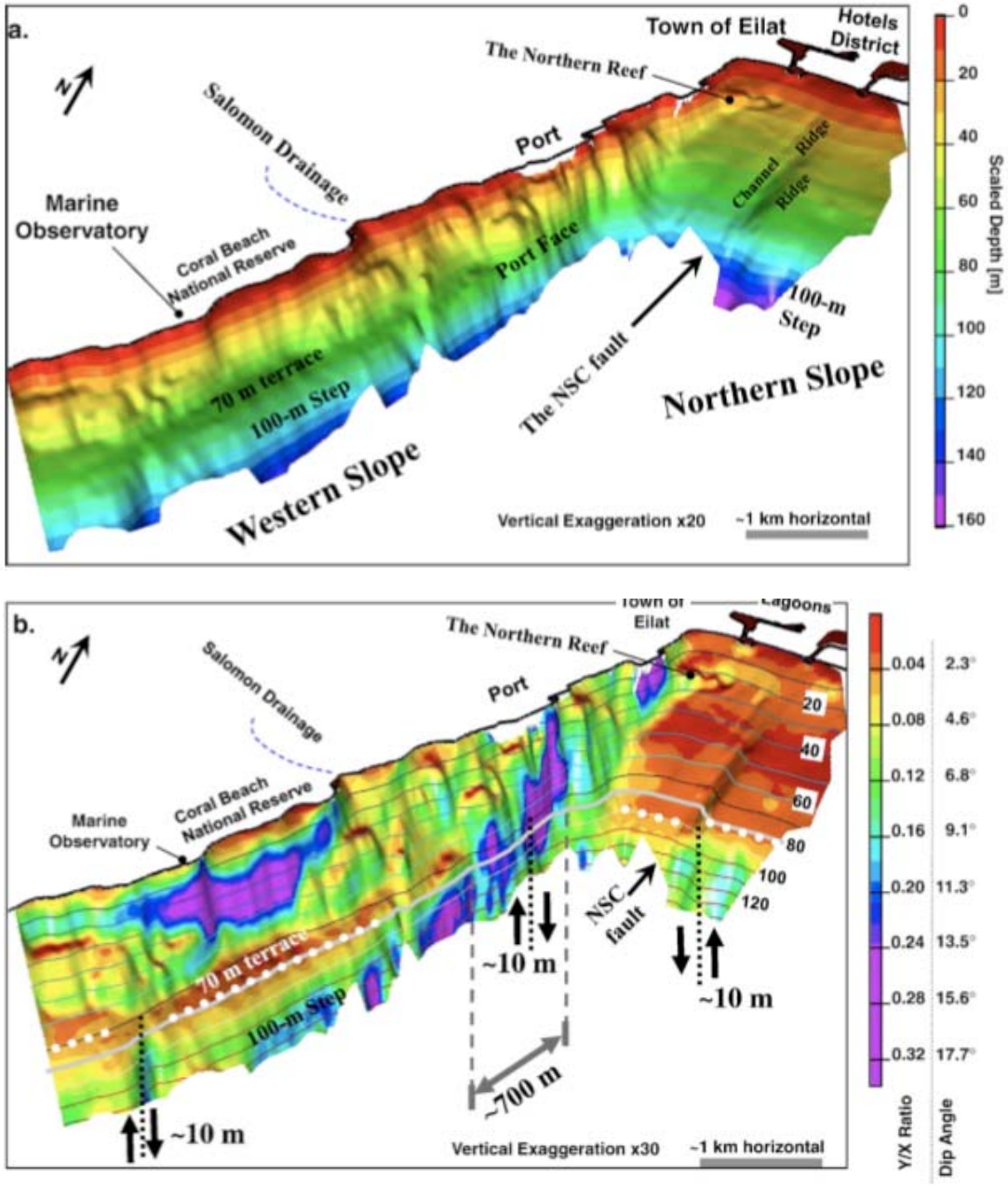

Northern Gulf of Eilat

Figure 1: 3D shaded relief depiction of our bathymetric map viewed from the south east and above. Black line marks the coast line. a. The shaded relief is colored according to approximately-scaled water depth (with water velocity of 1540 m/s), and is vertically exaggerated × 20. Features and locations discussed in the text are noted. The NSC fault trace asses below the gentle step between the ridge and channel (labeled). b. The shaded relief is color coded by the gradient of the bathymetry, overlaid by depth contours, and vertically exaggerated × 30. Terraces are apparent in red, while steep faces are purple. Apparent vertical offsets of the 100-m Step (see also Fig. 3) are roughly estimated by the changes in depth of the 2.3° contour (dashed with white circles), and noted with their sense and order-of-magnitude size (dashed lines and arrows). A gap of about 700 m in the 100-m Step below the port (the "Port Face") is noted in grey. Makovsky et al., 2008.

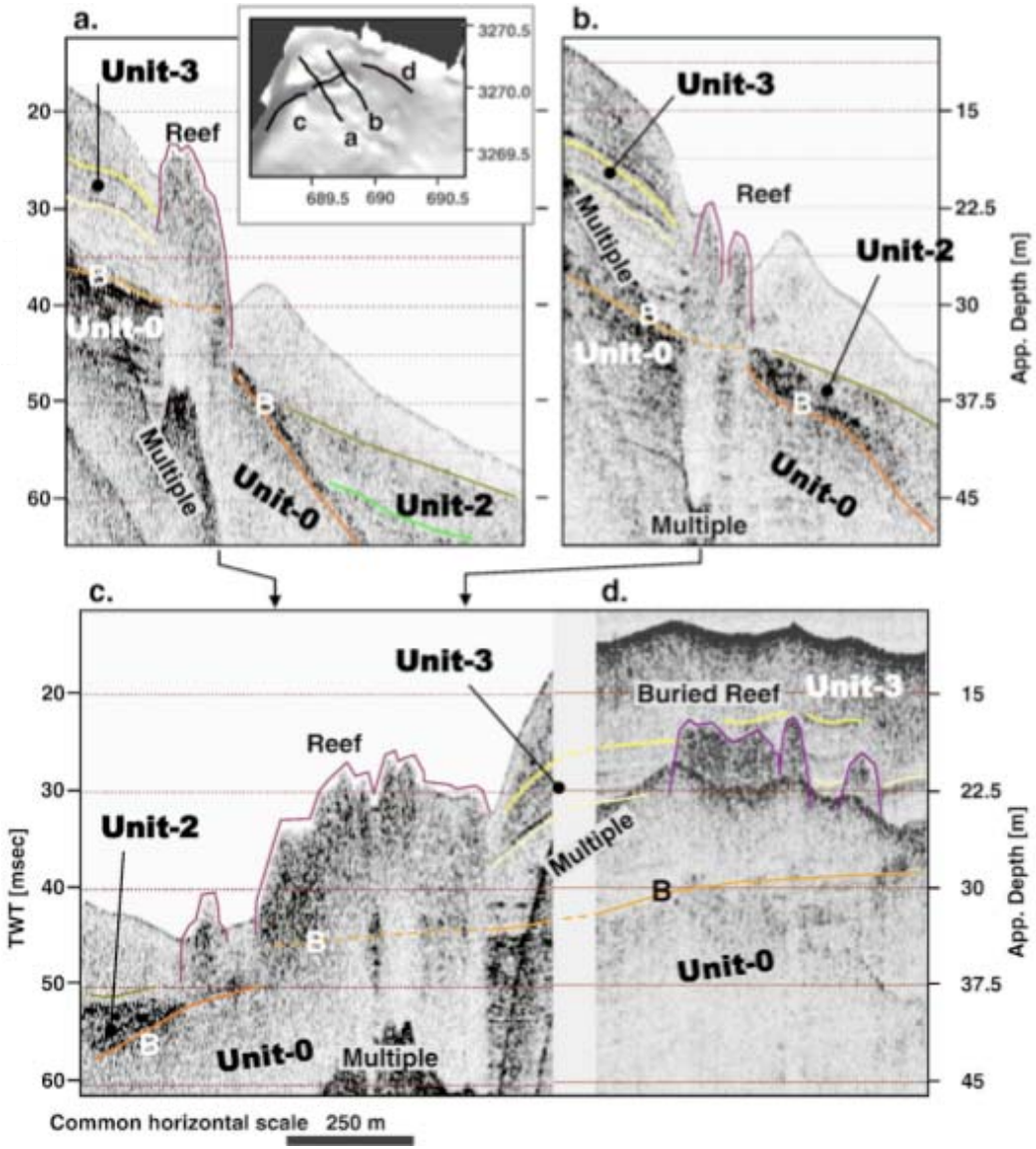

Figure 2: Four Chirp time sections across (a, b), and along (c, d), the Northern Reef. The section amplitudes are corrected by exponential gain, enhancing the internal reflectivity patterns and multiples. The profiles traces are overlaid on the shaded relief of the bathymetry and colored by in the inset map (top middle). Arrows between the sections show the intersections of profile (a) and (b) with profile (c). The sections are overlaid with colored interpretations of the basal surface (B) at the top of Unit-0 (orange), retrograde sedimentary wedges of Unit-2 (greens), reefs (purple), and Unit-3 coastal ramp layers (yellows). The reefs prevent acoustic penetration, appearing to cast a light shade beneath them. The buried reef seems somewhat shallower than the exposed reef, but that is probably an artifact of the higher seismic velocity in the burying sediments being higher than in the water. Note the flat tops of the reef in section (c) representing probably fossil reef tables. The first layers of Unit-3 above the basal surface (sections a, b) approach the reef uniformly not appearing to 'sense' its presence. Stratigraphically higher layers of Unit-3 dip where approaching the reef, probably because the sediments flow was blocked by the reef. Corresponding layers of Unit-3 cover the reef farther to the east. Makovsky et al., 2008.

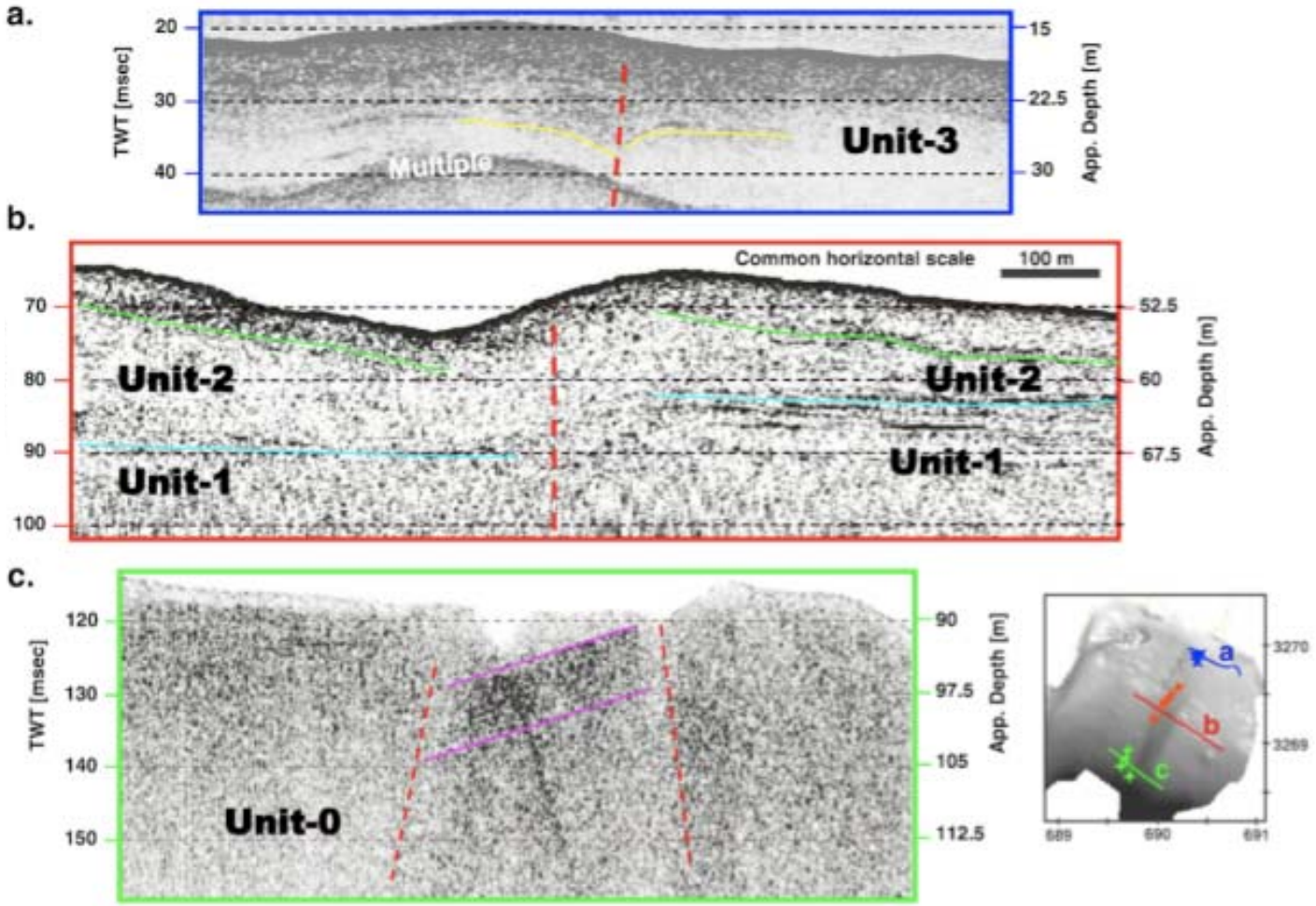

Figure 3: Three about 1-km long time sections across the NSC fault. Each section represents a different apparent style of faulting of the NSC fracture system. The profiles displayed, and locations at which each style of faulting is observed are marked with matching colors on the inset map. The different deformation styles are reminiscent of the near-surface appearance of a strike-slip fault. Interpretation of marker horizons is color-coded as in previous figures. The purple horizons marked in (c) are not correlated with any of the other units, and probably represent deeper horizons of Unit-1. Note that while the yellow horizon in (a) is not clearly offset, just bent inwards, the light blue horizon in (b) is offset by about 5 m across the interpreted fault trace. Due to the retrograde nature of the sedimentation (e.g. Fig. 6) section (a) images younger sediments than section (b), suggesting a differential offset with age (Makovsky et al., 2008).

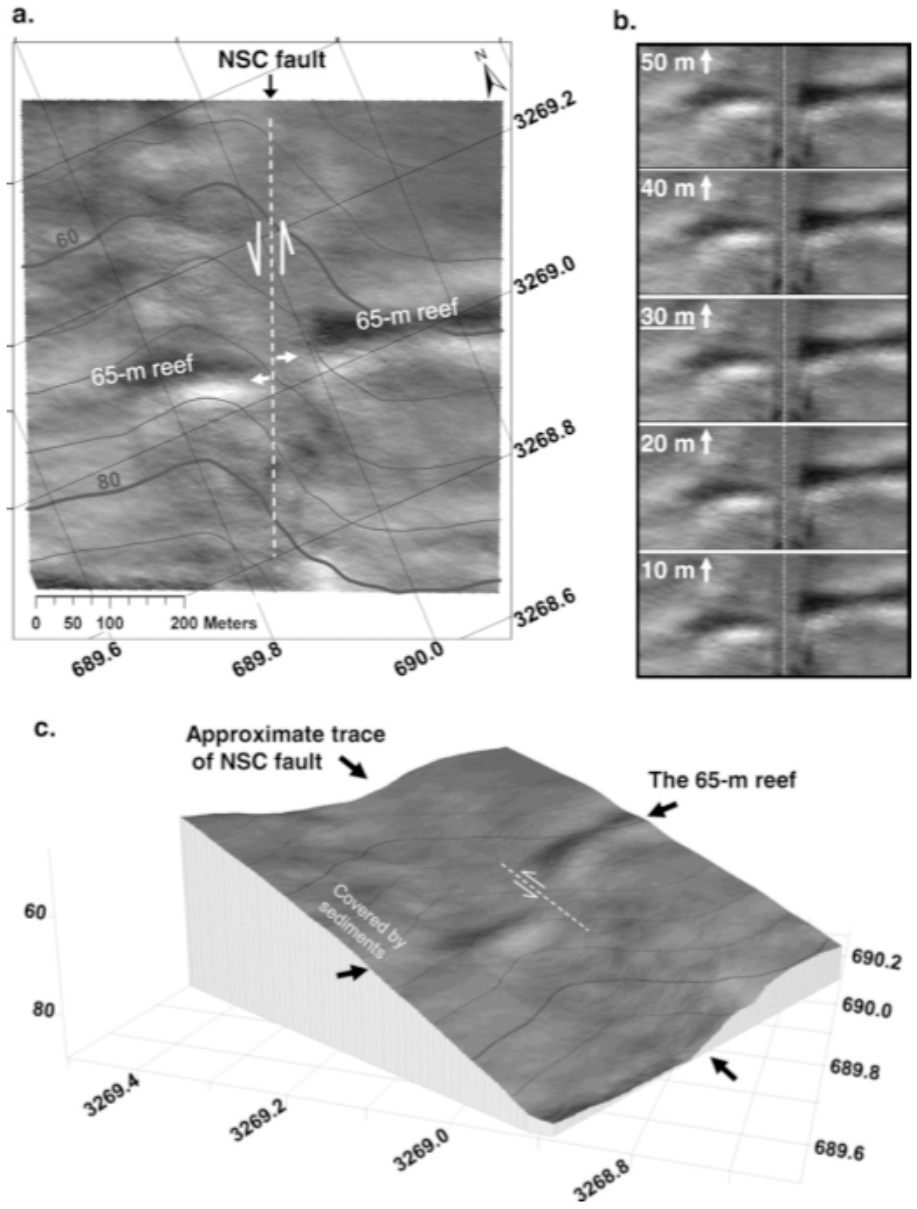

Figure 4: A high resolution bathymetric map produced (see text and Fig. 2b for details) from the dense Echo Sounder survey measurements (see Fig. 1b for location). a. A depth contour map of the Echo Sounder bathymetry (contour spacing of 5 m) overlain on a shaded relief depiction of this map. The map is oriented approximately along the trend of NSC fault bathymetric step (azimuth 23.5), and is centered on its approximate trace (dashed white line). The 65-m Reef appears as a sub-linear, 1 to 2 m high, bump on the seafloor lit on one side and shaded in the other. The reef is truncated and shifted left laterally where it crosses the trace of the NSC fault. b. Progressive reconstructions of the 65-m reef by shifting the western (left) side of the shaded relief depiction of the map in (a) northwards (upwards in a right lateral sense) by changing amounts (noted on each panel) with respect to a fixed eastern (right) side. A thin dotted line marks the contact between the two sides, along which the western panel is shifted. Best continuity of the 65-m Reef is obtained when shifting the western panel by 30 m. Some continuity is obtained also when the shift is 20, and 40 m. This test suggest that 30 ± 10 m left lateral slip was accommodated by the NSC fault since the formation and drowning of the 65-m Reef. c. A 3D-shaded-relief depiction of the map in (a) viewed from the south west. Vertical exaggeration is × 6. The 65-m reef is truncated and shifted both 30 ± 10 m left laterally and 10 ± 1 m down to the west where it crosses the seafloor step that marks the NSC (marked in white). A thin veneer of sediments covers the 65-m reef farther to the west. No significant progradation is observed in the depth of the reef's top, suggesting that most offset occurred after the reef stopped evolving (Makovsky et al., 2008).

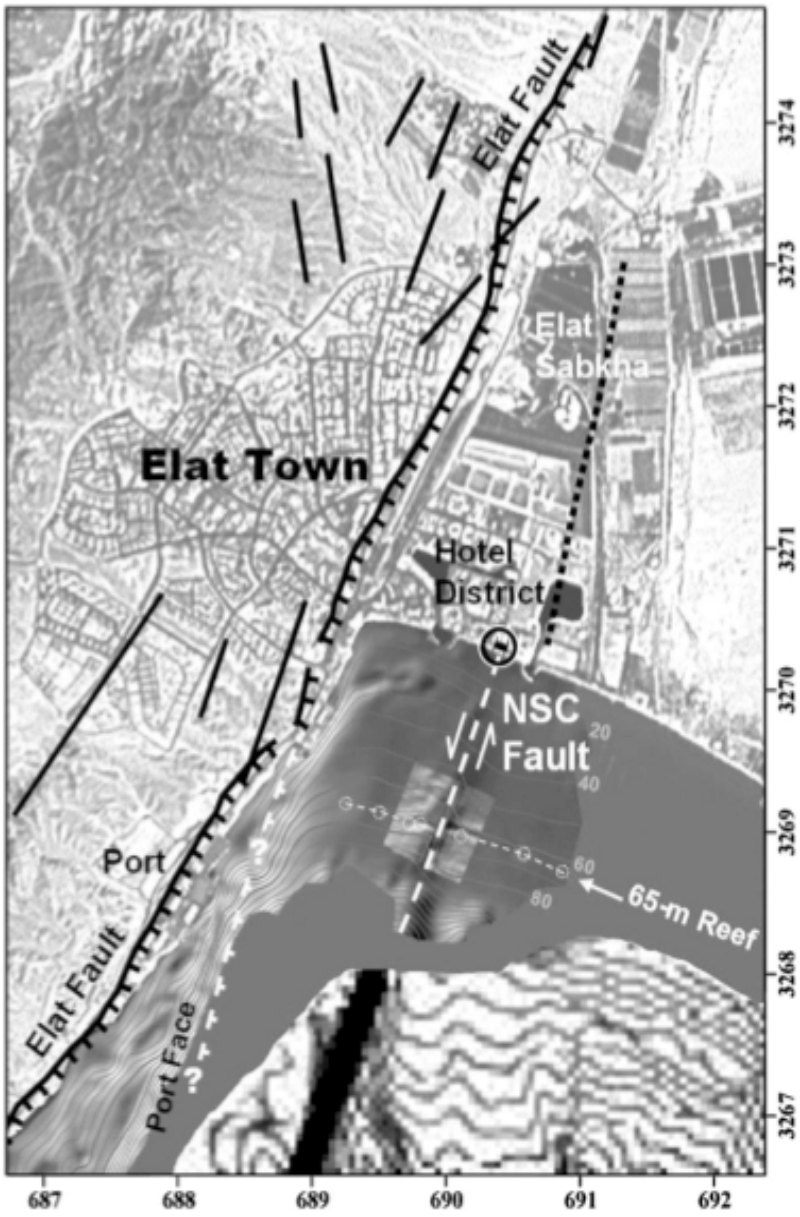

Figure 5: A map incorporating the results presented in this paper in the regional tectonicand civil context. A LANDSAT image of Elat and vicinity overlaid with 10 m bathymetric contours, and shaded relief depictions of the Chirp and Echo Sounder bathymetric maps. Also overlaid are the faults traces of Fig. 1b (black lines), and Ehrhardt et al. (2005) bathymetry (bright area in the bottom). The thick black line is Ehrhardt et al. (2005) interpreted fault. The location on the north coast where Frieslander (2000) imaged a sub-vertical fault is noted with a black bar (surrounded by a black circle), representing the range of uncertainty in the exact surface impingement of this fault. The eastern (right) side of this bar represents the projection of the fault‘s trend from about 100 ms (about 100 m depth). The locations where the 65-m Reef was imaged on our Chirp sub- bottom profile (dotted circles), and conceptual lines connecting these locations (thin dashed lines), are marked as on the inset of Fig. 6. The NSC fault is a major fault that crosses the Northern Slope approximately along the elongated bathymetric step (e.g. Fig. 4), offsets the 65-m Reef, and project into Elat hotel district and Elat Sabkha approximately where the sub-horizontal fault is imaged by Frieslander (2000). This trend of the NSC fault is approximately parallel with the trend of the Avrona fault 15 km to the north where it impinges southward into the Avrona Sabkha. The Elat fault, defined by Garfunkel (1970) as a predominantly normal fault, may be splaying south- ward along the Port Face and accommodating a significant down to the east slip Makovsky et al., 2008.

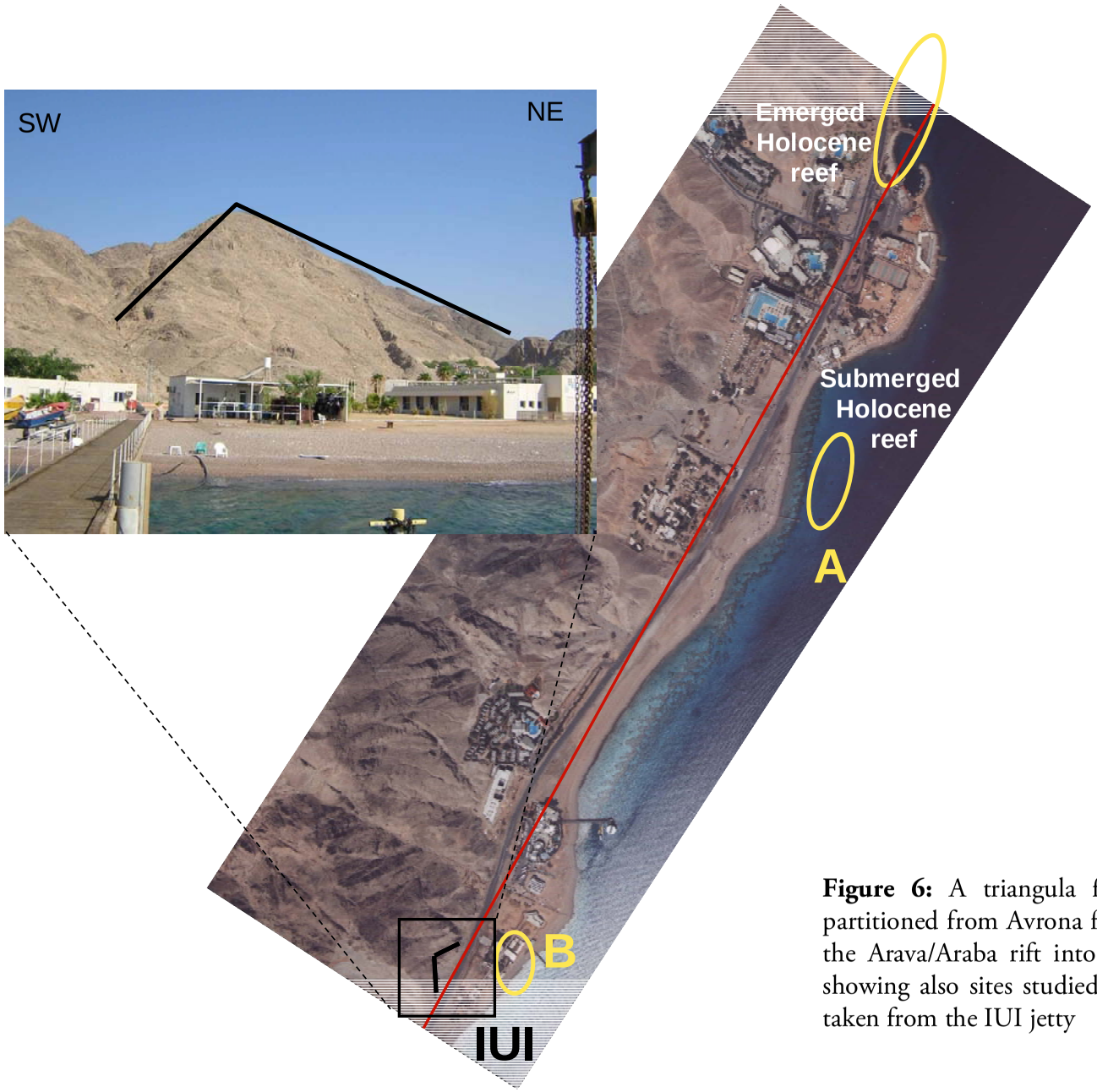

Figure 6: A triangula facet of Elat's fault - a normal fault partitioned from Avrona fault segment - the southern extension of the Arava/Araba rift into the Gulf of Elat-Aqaba. A: Airphoto showing also sites studied by Shaked et al. (2002, 2005). photo taken from the IUI jetty

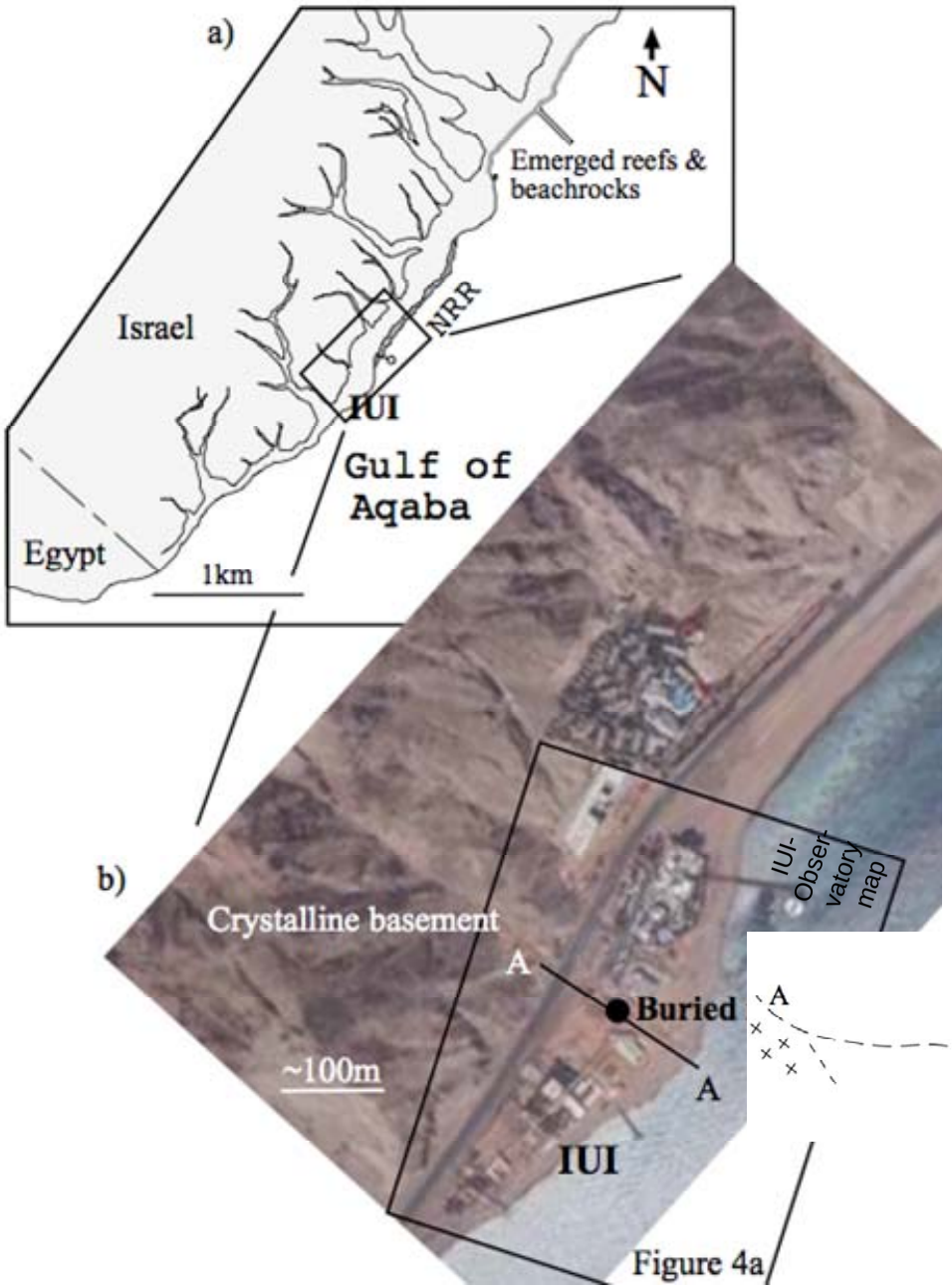

Figure 7: The IUI shoreline: a) Outline of the shore near the IUI showing the drainage patterns, location of the IUI and the modern nature reserve reef (NRR), and the emerged reefs that constrains the Holocene sea level. b) Aerial photo of the IUI beach with the location of the pits and boreholes that exposed the buried reef marked as a black circle. The box marks the area mapped in the next figure. c)Topographic profile across the IUI terrace at its widest part (A-A). Grey marks the length of the northern sediment trench. Shaked, 2002.

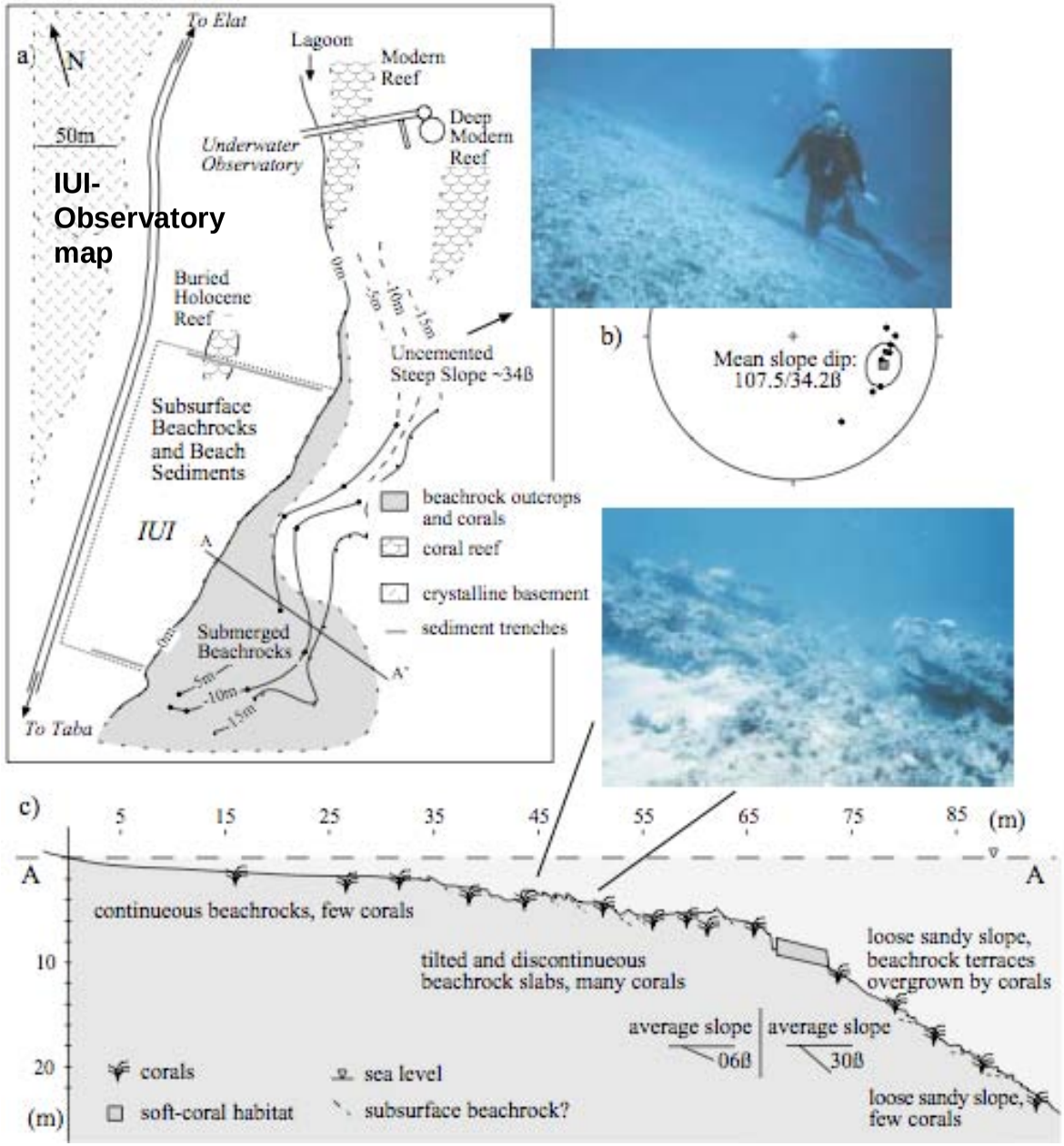

Figure 8: a) Geomorphic map of the shallow slope off-shore from the IUI. b) The north- facing slope of unconsolidated material, its average dip 34°. Note the air bubbles above the diver, indicating vertical. c) A cross section off the south-facing slope and photo from the shallow part showing tilted beachrock strips overgrown by corals. Shaked, 2002.

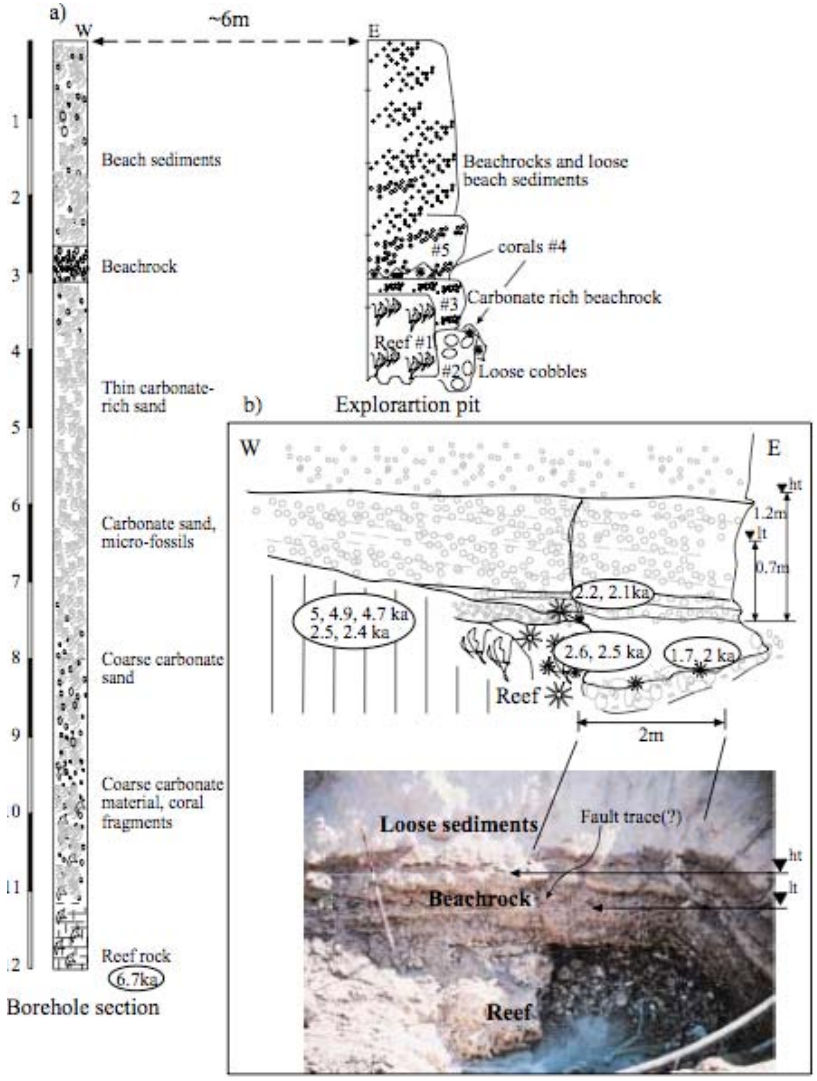

Figure 9: (top) Stratigraphy of the IUI buried reef: a) Log of borehole (left) and ~6m E of it stratigraphic section at the research pit. b) Cross section (north wall) and photograph of the buried reef at the IUI research pit. lt= low tide mark; ht= high tide mark. Shaked, 2002.

Figure 10: (right and bottom) Samples from the buried reef. a) The edge of the reef front structure comprising a large Lobophylia (2.8ka) covered by carbonate rich clastic sediment and overgrown by a small Astreopora and Gyrosmilia. b) and c) Microscope photos of the Gyrosmilia that overgrows the reef front (2.3ka). d) A delicate Acropora overgrowing a granite cobble east of the reef structure. Many similar corals were found at the site. The perfect preservation of every detail of the coral indicates that it has never been transported or exposed to erosion. Shaked, 2002.

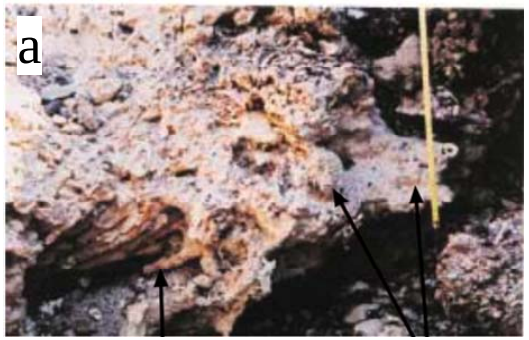

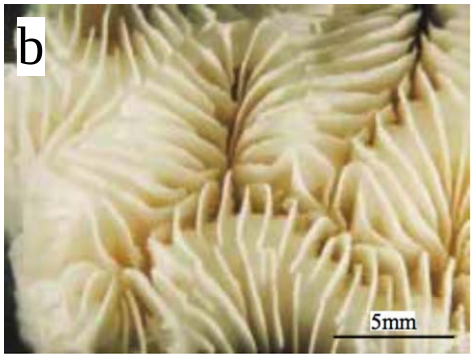

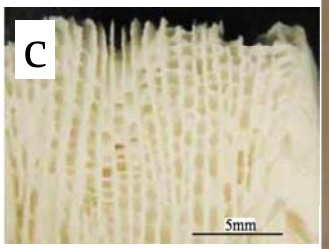

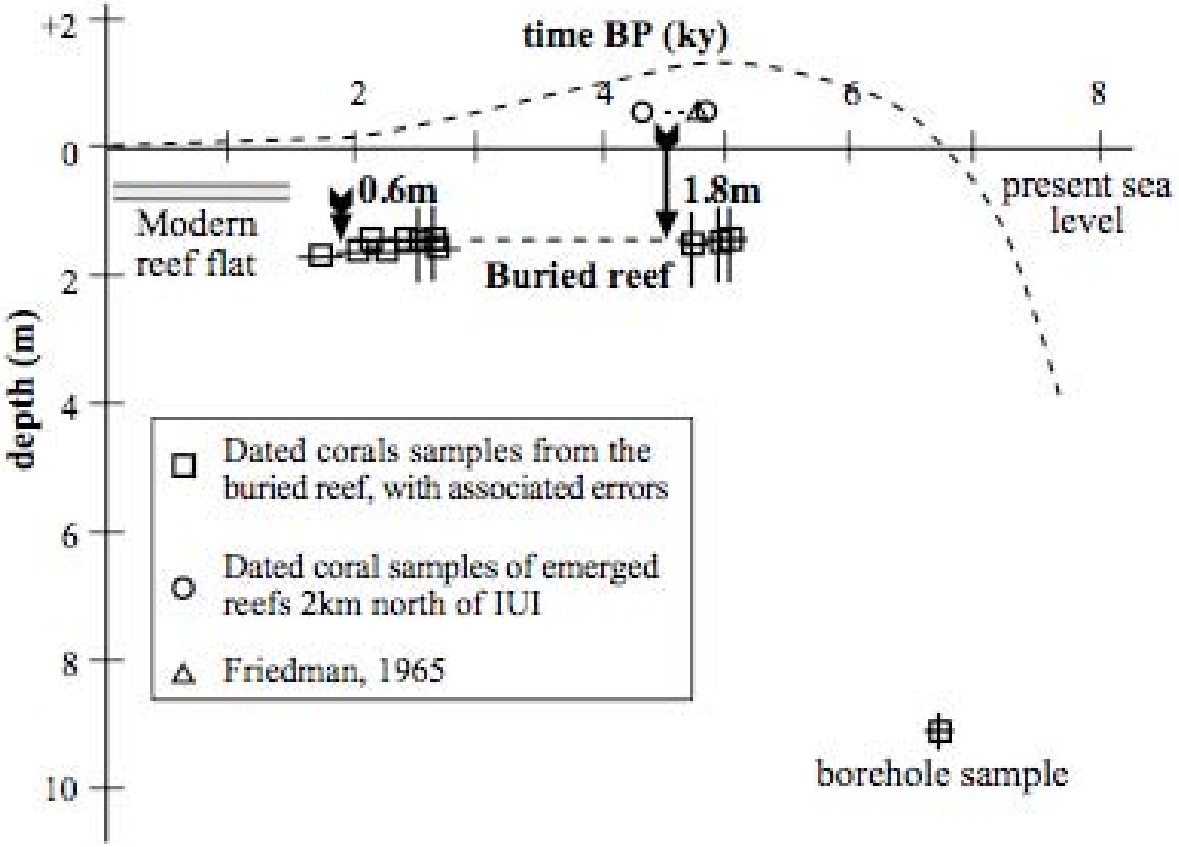

Figure 11: Elevation versus age of coral samples from the buried reef (squares) and emerged reef outcrops ~2km to the north (circles and triangles). The emerged outcrops represent the in-situ position of ~5ka reefs around the Gulf of Aqaba. The length of the arrows is the estimated down faulting of the buried reef relative to emerged Holocene reefs, and to the modern reef of Elat (gray bar). Shaked, 2002; Shaked et al., 2004.

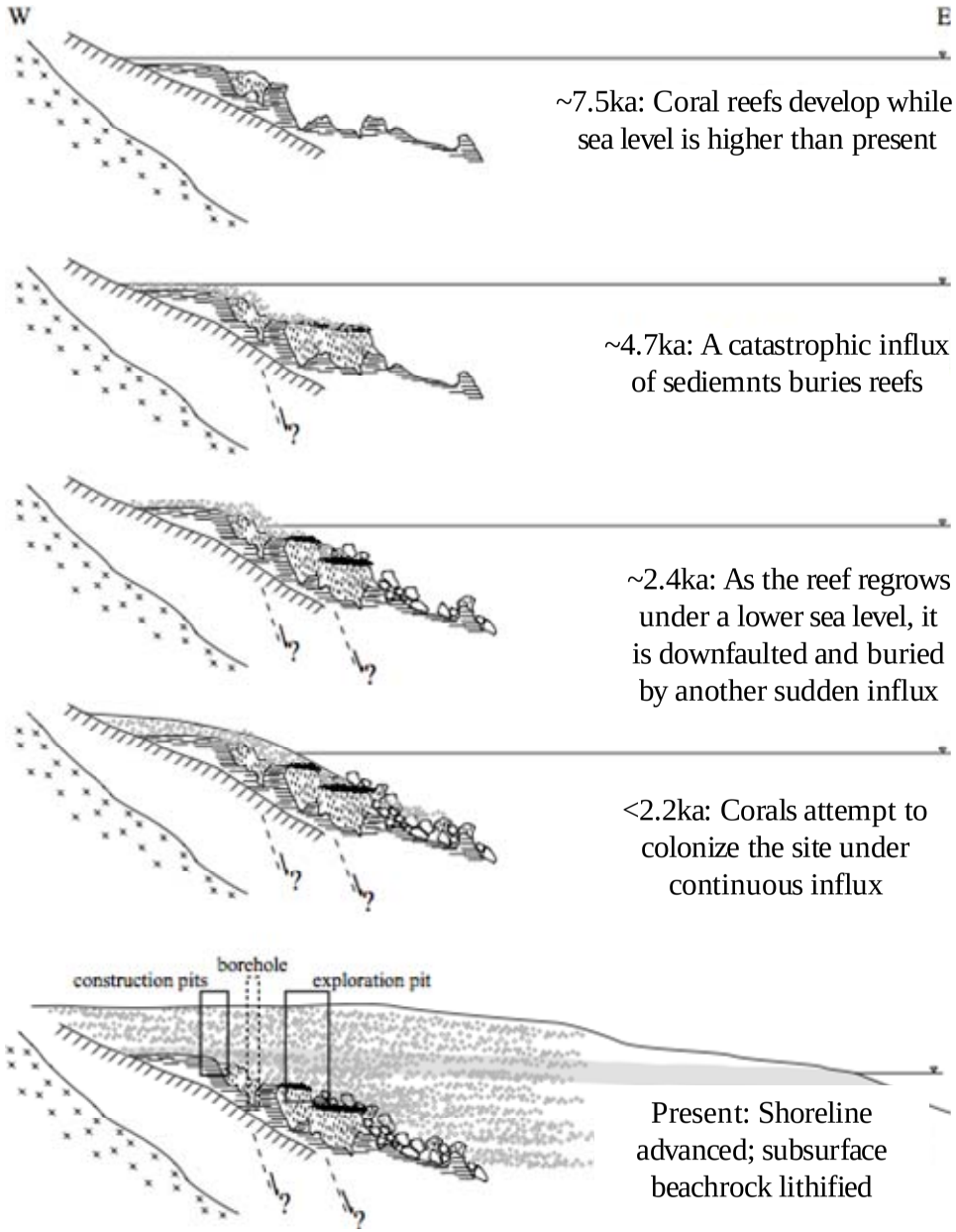

Figure 12: Illustration (not to scale) of reconstructed events at the IUI buried reef site. Boxes at present-day section denote the stratigraphy found at construction pits and the exploration pit. The dashed box of the borehole stratigraphy is in reality normal to the section and only shows the older reef beneath lagoon sediments.

Shaked, 2002

References

Makovsky, Y., Wunch, A., Ariely, R., Shaked, Y., Rivlin, A., Shemesh, A., Ben-Avraham, Z., Agnon, A., 2008. Quaternary transform kinematics constrained by sequence stratigraphy and submerged coastline features: The Gulf of Aqaba, Earth Planet. Sci. Lett., 271, 109-122.

Shaked, Y., 2002. Neotectonics and eustasy at the Gulf of Elat-Aqaba. PhD Thesis, Hebrew Univ., Jerusalem,

Shaked, Y., Marco, S., Lazar, B., Stein, M., Cohen, C., Sass, E., Agnon, A., 2002. Late Holocene shorelines at the Gulf of Aqaba: Migrating shorelines under conditions of tectonic and sea level stability, Eur. Geophys. Soc. Stephan Mueller Spec. Publ. Ser., 2, 1–10.

Shaked, Y., Agnon, A., Lazar, B., Marco, S., Avner, U., Stein, M., 2004. Large earthquakes kill coral reefs at the north-west Gulf of Aqaba, Terra Nova, 16: 133-138.

Shaked Y, Lazar B, Marco S, Stein, M., Tchernov, D., Agnon, A., 2005. Evolution of fringing reefs: space and time constraints from the Gulf of Aqaba Coral Reefs 24: 165-172.

Late Quaternary Seismicity of The Southern Arava Valley, The Dead Sea Fault

Rivka Amit[1*], Yehouda Enzel[2*], Porat Naomi[1*], Yariv Hamiel[1*], Ezra Zilberman[1]

[1]Geological Survey of Israel

[2]The Hebrew University of Jerusalem

rivka@gsi.gov.il

*Field guide

Late Quaternary paleoseismicity of the southern Arava was deduced from offsets on faults detected in trenches, in a fault zone that is 6 km wide and 40 km long, extending through the rift valley from the north-western coast of the Gulf of Elat (Aqaba) to the north-east (Amit *et al.,* 1995; Amit *et al.,* 2002; Zilberman *et al.,* 2005). The fault zone may be subdivided into three subzones: a central sub-zone, 5 km wide, trending northeast, characterized by sinistral faults expressed by push-ups and pull-aparts, and two marginal zones characterized by normal faults that trend northwest and north–northeast on both sides of the rift valley (Fig. 1). Amit *et al.* (2002) reported 20 different paleo-earthquakes between 45-1 Kyr BP in the southern Arava segment. The cumulative normal slip versus time that was calculated from these data shows that a constant slip rate of 0.5 mm/year can account for the total normal slip. The lower-than-average amount of normal slip per event recorded during the last 16 Kyr (12 events, average slip of 0.65m per event) is compensated by the shorter recurrence interval in that period (1,500 years), as compared to the earlier period of 45-16 Kyr (8 events, average slip of 1.4m, and a recurrence interval of 3,000 years) (Fig. 2). The difference in slip per event between the two periods is statistically significant ($p < 0.002$ in the Mann-Whitney test, where p is the probability that the two samples are drawn from the same population).

Assuming an average slip rate of 5 mm/year for the left lateral motion along the DSF, the average cumulative normal slip rate in the southern Arava of 0.5 mm/year suggests that normal faulting is only ~10% of the total strike-slip motion in the last 45 Kyr. This is supported by the calculated rate for small and large earthquakes along the DSF in modern times (Hofstetter *et al.,* 2003; Salamon *et al.,* 2003), and by the amount of transverse extension along the fault (e.g. Joffe and Garfunkel, 1987). Similar dip slip to strike slip ratio was observed in the north-eastern Sea of Galilee basin (Marco *et al.,* 2005).

The transformation of displacement detected in trenches across faults to earthquake magnitude was calculated using the regressions presented by Wells and Coppersmith (1994). The calculated magnitudes for all paleo-earthquakes in the Arava segment are in the range of $5.9<M_w<7.1$, with average magnitude of $M_w6.5$ for 16-1 Kyr, and 6.8 for 45-16 Kyr BP. Due to the nature and inaccuracy of the displacement-magnitude relation (Wells and Coppersmith, 1994), we assume an error in magnitude of ±0.6 (~10%) for all paleo-events. The earthquake catalogues that are

based on historical records report a single large earthquake (M>6) that occurred in the year of 1068 AD in the southern Arava (e.g., Guidoboni and Comastri, 2005; Zilberman *et al.,* 2005), which is included in the above mentioned record. Due to the remoteness of this desert area in ancient times it is hard to find a reliable historic evidence for earlier events. Fig. 3 shows the calculated frequency-magnitude relation for the Southern Arava segment using the instrumental and paleo-seismic records. The instrumental record includes 123 events and was divided to magnitudes between 2-2.9, 3-3.9, and 4-4.9. The instrumental data were taken from the Geophysical Institute of Israel earthquake catalogue (www.gii.gov.il). As the catalogue is complete for earthquakes with $M_L \geq 2$ only since 1983, we used instrumental data that were recorded between the years of 1983 and 2007. We found that the data points as retrieved from paleo-seismic record for the Southern Arava segment lie on the linear extrapolation of the frequency-magnitude relation of the instrumental record, with a calculated *b*-value (the slope of the frequency-magnitude relations) of 1. This value is in agreement with b=0.96 that was found for the DSF in Israel using instrumental data only (Shapira and Hofstetter, 2002).

The marginal fault zone – Nahal Shehoret

The alluvial fan of *Nahal* Shehoret is dissected by sub-parallel normal faults arranged in a domino structure. The displaced alluvial surfaces are of Holocene and Pleistocene ages (Fig 4). The domino structure has a surficial expression of shallow saddles scattered across the alluvial surfaces and arranged along straight lineaments directed north - south. Eight trenches were excavated from west to east across several fault scarps in this zone. The faults were trenched from west to east. To the west, faults displace alluvial surfaces of Middle Pleistocene age and to the east faults displace Upper Pleistocene and Holocene alluvial surfaces and Holocene playa deposits. The total vertical displacements on these normal faults ranges from 7.5 m at trench T-6 (Fig. 5), where a fault displaces an Upper Pleistocene alluvial surface, to 0.5 m at trench T-15, where a fault displaces a Holocene alluvial surface. All of the faults are multiple-event fault types except the youngest Holocene fault, which is a single-event type (Table 1). The oldest fault, exposed in trench T-8 (Fig. 1), is oriented NNW and was active after 80ka; based on the catenary relationship it was determined that its activity ceased at most 40ka ago. The fault with the youngest activity is exposed in trenches T-5,T-6,T-17 and T-16. All these trenches were excavated across a N-S lineament of about 3.5 km long. The orientation of this lineament contrasts with the NNW orientation of the fault line exposed in trench T-8 (Amit et al., 2002)

Trench T-17 (Fig. 4)

Trench, T-17, was excavated on the continuation of the fault line exposed in trench T-6 (Fig. 6). The total amount of displacement which is 100 m north to trench T-6 reaches 3.4 m. The normal fault is characterize by an angular unconformity associated with faulting accompanied by

back tilting and followed by normal drag along the fault plane. The tilted of the brittle materials mainly resulted in the opening of tension fissures related to the normal fault between the tilted blocks. Three dicrete colluvil wedges (Fig 6; C1-C3) were deposited as a result of three faulting events post 63.9± 10.9 ka, the age of the surface on which the Reg soil developed across the tilted blocks. The age of the faulting event related to the deposition of unit C1 can not be precisely determined by OSL. This difficulty is because of poor bleaching of the sediment as a result of rapid burial of the collapsed soil material from the hanging wall and soil material dragged toward the fault on the down faulted block. There for the OSL age of wedge C1, composed of colluvial material represents the age of surface Qa1 and not the age of the faulting event. This event displace the surface by 1.5 m, occurred after 63.9± 10.9 ka, the age of the surface. A soil developed in unit C1 during an interval of 7-10 ky. The estimated of the time to form the soil is used to bracket the timing of the first tectonic event detected in this trench to between 7-10ky before the second tectonic event 36 ± 4.5 ka; thus the first event occurred at 45±2 ka. Colluvial unit C2 was dated at 36 ±4.5 ka A third small event occurred later; according to the very weak soil profile developed in the colluvium, the event might have occurred during the past 10ky. The two events are related to the major faulting activity detected in trench T-6. Later displacements were smaller, up to 0.4 m, as also evident in other trenches on this lineament .
A similar trend is also discernible in trench T-15, which was excavated on the same fault line as trench T-17 and T-6 (Table 1). In this case, faulting displaced a Holocene surface. Only one event with a displacement amount of 0.5 m is evident. Based on the relative age dating of soils, it occurred during the Holocene (about 8ka).

The westernmost part of the marginal fault zone was active until 80 ka (Fig. 1,4; trench T-8). The next set of fault trace ~0.5 km to the east was active between 37 and 5 ka, during the late Pleistocene and the middle Holocene (trenches T-10, T-15, T-6). At least two branches represented by trenches T-10 and T-17 were active together. A clear trend of decreasing with time in the amount of displacement is evident across this fult zone. An important observation is that the amount of displacement and number of faulting events vary along a single fault trace.

The central fault zone - Avrona Playa

The central part of the Elat fault zone is characterized by extension and compression structural features, such as grabens and push-up ridges. Flower structures typical of strike-slip faults are clearly defined in the subsurface. Two environments were chosen for paleoseismic analysis. One is a Holocene alluvial fan of Nahal Shehoret that is crossed by a graben structure (Fig. 7). The other, located to the east, is the Avrona playa, across which push-ups, pull-apart and normal faults occur (Fig. 8).

The youngest surface ruptures in the southern Arava valley were detected in the Avrona playa area (Fig. 1). The playa forms one of several en-echelon tectonic basins bounded by subparallel left-stepping faults. It is a 10 km long and 0.5-2 km wide basin that is crossed diagonally by the Elat fault zone in a NNE direction. The playa area at present forms a broad elevated elongated ridge. Its relief is composed of low longitudinal sub-ridges (0.5-4 m high and up to 5 km long) and shallow braided channels flowing along and across these ridges. Wadi Avrona and Wadi Raham drain the playa toward the Gulf of Elat through the Elat coastal sabkha. A detailed analysis of the tectonic history, which deformed the Avrona playa, and changed it from a closed basin with internal drainage system to an open basin, is presented in Amit et al. (1999) (Fig. 8,9). The paleoseismic data is summarized briefly next.

A 2 km long by 1 m high fault scarp dissects a transitional, non-sterile, vegetated playa zone composed of sand to sandy-loam sediment. This fault was evaluated to be the youngest in the playa area. A trench excavated at this site exposes a multiple-event normal fault with one main fault plane (Fig. 10). Five partially preserved colluvial units were identified adjacent to the fault plane (Fig. 10, units I-V). Each wedge merges with a fluvial unit on the down-faulted block. Continues fluvial erosion on the down faulted block removed most of the colluvial material, leaving only the upper most part of each colluvial wedge. The variation in the pedogenic features in the colluvial units indicates that each wedge formed during different time period. According to the age of unit 3, which overlies the colluvial units, and unit 1a at the base of the section, five tectonic events occurred between 14,200± 300 and 3700± 300 years ago. Each of these events was accompanied by displacements of at least 0.5 m. The deposition of unit 3 marks the beginning of at least 2000 years of quiescence. During this period, fluvial sediments were deposited mainly on the down faulted block. Fluvial activity along the fault scarp decreased over the last 3000 yr. Toward the end of this period, fluvio-eolian sand sheets were deposited over the entire playa area and cover the fault trace. At this stage a soil was developed continuously across the inactive faulted area. Tectonic activity along this fault was renewed sometime between 700 and 1000 years ago, as indicated by a vertical surface displacement of about 1 m (the petrosalic horizon, detected in unit 5a, of the Salorthid soil was used as a stratigraphic maker for the measurement of the displacement). The paleoseismological, geophysical and archaeological evidences indicate that this last event was the historical devastating earthquake which occurred in 1068 AD in the eastern Mediterranean region (Fig. 11) (Zilberman et al., 2005). To conclude, at least six surface rupture events have affected the Avrona playa during the last 14,000 years.

Geodetic measurements of the displacement field along and across the DST

The estimated seismic slip rate along the DSF, based on historical earthquakes account for only 1/3 of the total plate motion (Garfunkel et al., 1981), and the 20th century seismicity accounts for only 10% of the geologic slip (Salamon et al., 1996). These estimations indicate that either a strong earthquake along the DST is overdue or that the missing slip is aseismic. A first direct evidence for creep along the DSF was reported by Finzi (2005). In this study, aseismic slip was detected by Interferometric Synthetic Aperture Radar (InSAR) measurements of surface deformation along the Arava segment within Yotvata, Zofar and Avrona fault step-over zones. However, no creep was detected between these zones. Finzi (2005) suggested that 30-50% of the total slip was released aseismically during the years 1995-2000. However, due to the fact that the look angle of InSAR satellites is almost perpendicular to the direction of the DSF, it makes it very difficult, almost impossible, to measure interseismic surface deformation along the DSF using InSAR observations.

Several attempts were made to geodetically measure the displacement field along and across the DST in Israel. A network of far-field permanent GPS receivers revealed about 3.7 mm/yr left-lateral movement across the DST, but suggested that the fault itself is locked (*Wdowinski et al.,* 2004). Analysis of two campaign GPS measurements in Israel in 1996 and 2002, led *Ostrovsky* (2001) to estimate the present rate of plate movement along the central DST to be 7.5mm/yr. Recent detailed GPS measurements across the Arava segment (southern DST) suggested left-lateral motion on the order of 5mm/yr and a locking depth of 12km (*Le Beon et al.*, 2008). Still, all recent GPS observations along the DST lack near-fault measurements and therefore are unable to resolve the depth or the rate of shallow creep motions. Figure 12 presents the location of new campaign sites along a dense profile (200-1000 m apart) and across the geologically mapped Arava fault zone .

References

Amit, R., E. Zilberman, N. Porat, Y. Enzel (1999). Relief inversion in the Avrona playa as evidence of large-magnitude historical earthquakes, southern Arava Valley, Dead Sea Rift. Quaternary Research 52, 76-91.

Amit, R., Harrison, J.B.J., Enzel, Y., 1995. Use of soils and colluvial deposits in analyzing tectonic events – the southern Arava valley, Israel. Geomorphology, v.12, 91-107

Amit, R., E. Zilberman, Y. Enzel, and N. Porat (2002). Paleoseismic evidence for time dependency of seismic response on a fault system in the southern Arava valley, Dead Sea rift, Israel, *Geol. Soc. Am. Bull.* 114, 192-206.

Finzi, Y., 2005. Current deformation in the southern Dead Sea Transform: Radar interferometry measurements and their tectonic implications. Geological Survey of Israel report, GSI/24/04, 74 p.

Garfunkel, Z., I, Zak, and R., Freund, 1981, Active faulting in the Dead Sea rift, *Tectonophysics,* 80, 1-26.

Guidoboni, E., and A. Comastri (2005). *Catalogue of earthquakes and tsunamis in the Mediterranean area from the 11th to the 15th Century.* INGV-SGA, Italy.

Hamiel, Y., R., Amit, Z.B., Begin, S., Marco, O., Katz, A., Salamon, E., Zilberman, N., Porat (in press), The seismicity along the Dead Sea fault during the last 60,000 years. BSSA

Hofstetter, A., H.K. Thio, and G. Shamir (2003). Source mechanisms of the 22/11/1995 Gulf of Aqaba earthquake and its aftershock sequence, *J. Seism.* 7, 99– 114.

Joffe, S., and Z. Garfunkel (1987). Plate kinematics of the circum Red Sea- a re-evaluation, *Tectonophysics* 141, 5-22.

Le Beon, M., Y. Klinger, A.Q. Amrat, A. Agnon, L. Dorbath, G. Baer, J-C Ruegg, O. Charade, O. Mayyas, 2008. Slip rate and locking-depth from GPS profiles across the southern Dead Sea Transform, *J. Geophys. Res.,* 113.

Marco, S., T.K. Rockwell, A. Heimann, U. Frieslander, and A. Agnon (2005). Late Holocene slip of the Dead Sea Transform revealed in 3D palaeoseismic trenches on the Jordan Gorge segment, *Earth Planet. Sci. Lett.* 234, 189-205.

Ostrovsky, E., 2001. The G1 GPS geodetic-geodynamic reference network: Final processing results. Israel Journal of Earth Sciences, v. 50, 29 - 38

Salamon, A., A. Hofstetter, Z. Garfunkel, and H. Ron (1996), Seismicity of the Eastern Mediterranean region: Perspective from the Sinai subplate, *Tectonophysics*, *263*, 293-305.

Salamon, A., A. Hofstetter, Z. Garfunkel, and H. Ron (2003). Seismotectonics of the Sinai subplate - The eastern Mediterranean region, *Geophys. J. Int.* 155, 149-173.

Shapira, A., and A. Hofstetter (2002). Seismicity parameters of seismogenic zones, *Geophy. Inst. Israel report,* 592/230/02.

Wells, D.L., and K.J. Coppersmith (1994). New empirical relationships among magnitudes, rupture length, rupture width, rupture area, and surface displacement, *Bull. Seismol. Soc. Am.* 84, 974-1002.

Wdowinski, S., Bock, Y., Baer, G., Prawirodirdjo, L., Bechor, N., Naaman, S., Knafo, R., Forrai, Y, Melzer, Y., 2004. GPS measurements of current crustal movements along the Dead Sea Fault. JGR, v. 109, B05403, doi:10.1029/2003JB002640

Zilberman, E., R. Amit, N. Porat, Y. Enzel, and U. Avner (2005). Surface ruptures induced by the devastating 1068 AD earthquake in the southern Arava valley. Dead Sea Rift, Israel, *Tectonophysics* 408, 79-99.

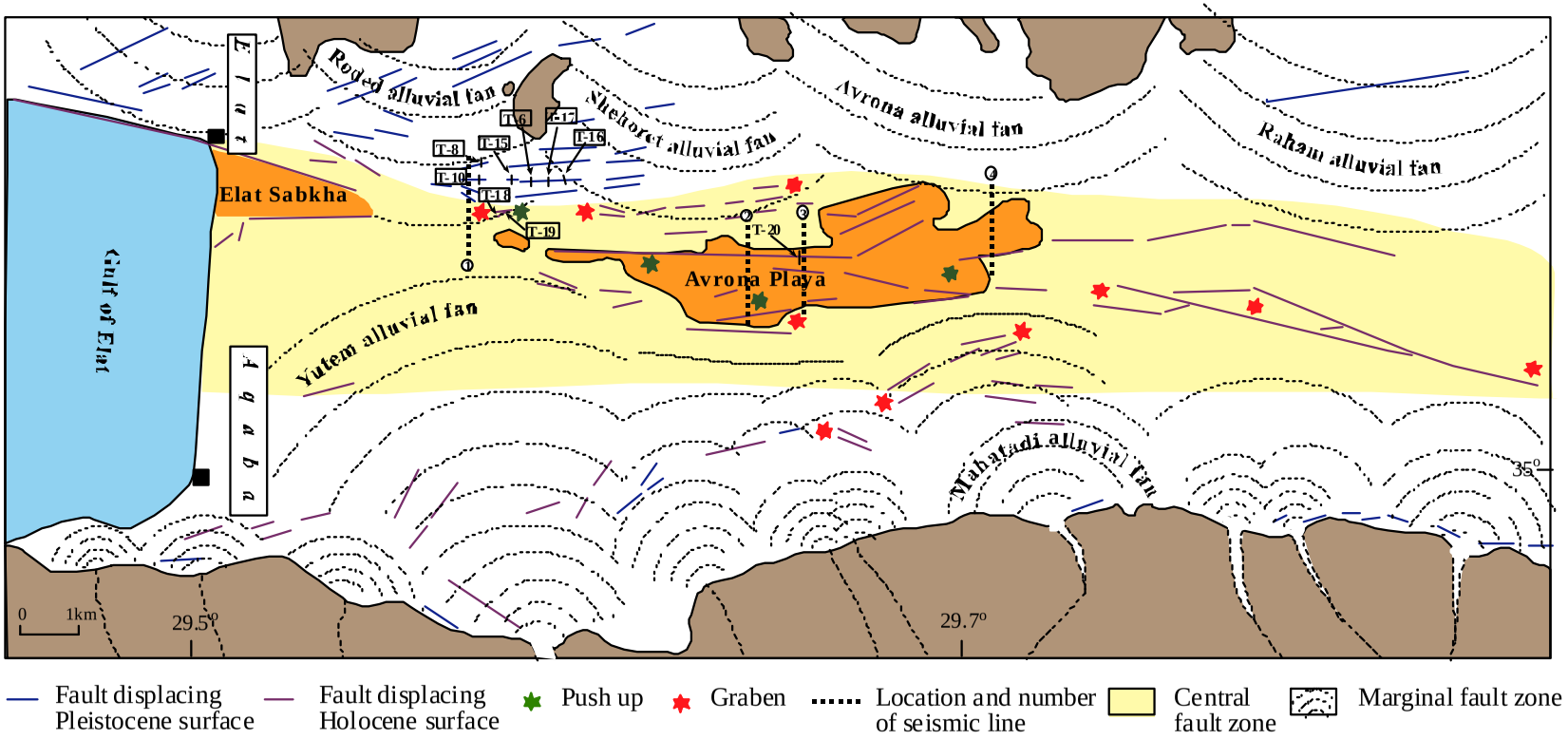

Figure 1: Map of the southern Arava Valley showing the main morphological and morphotectonic elements of the southern Arava Valley. Notice marginal (white color) and central fault zone (Yellow color), the distribution of the trenches across the selected fault lines and the location of seismic lines.

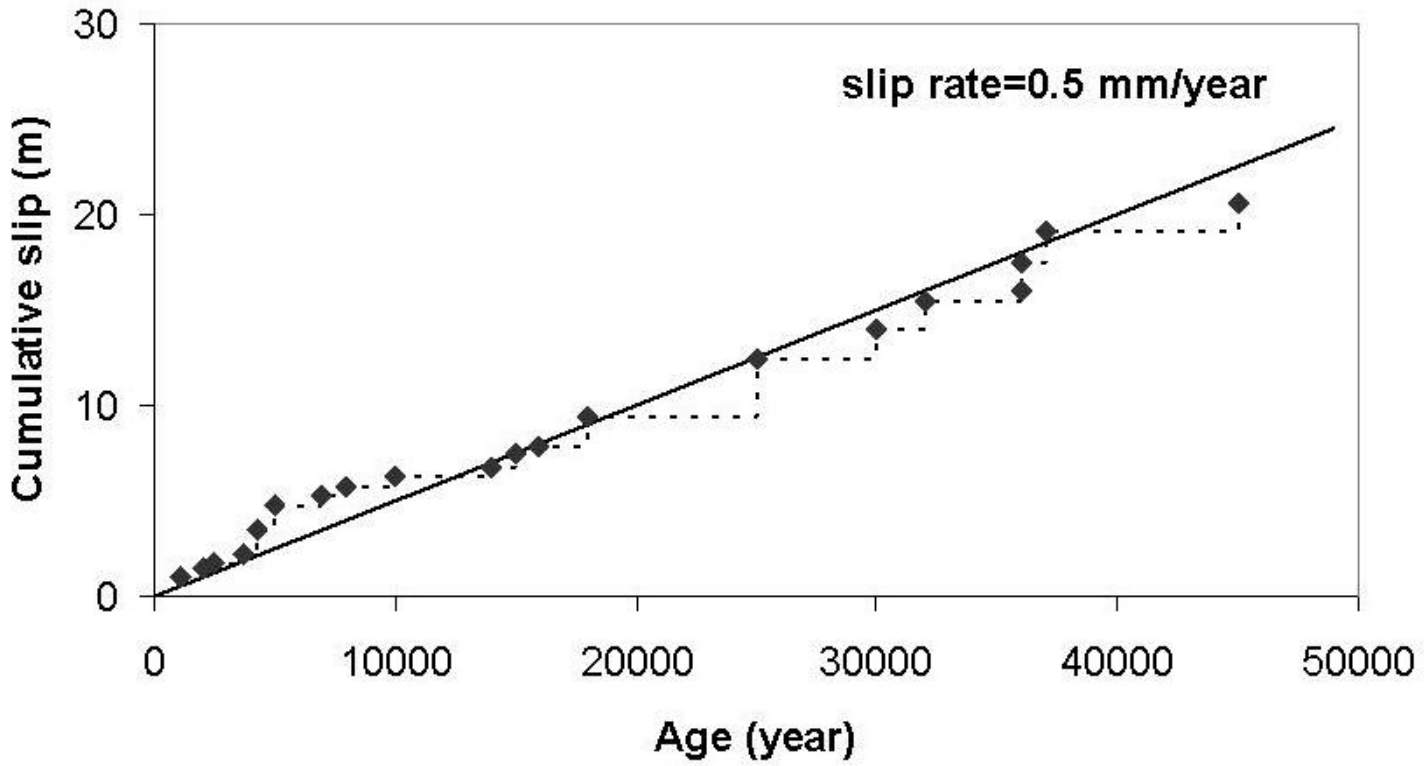

Figure 2: Cumulative normal slip versus time from the southern Arava paleo-seismic data (diamonds). The black line illustrates a slip rate of 0.5 mm/year.

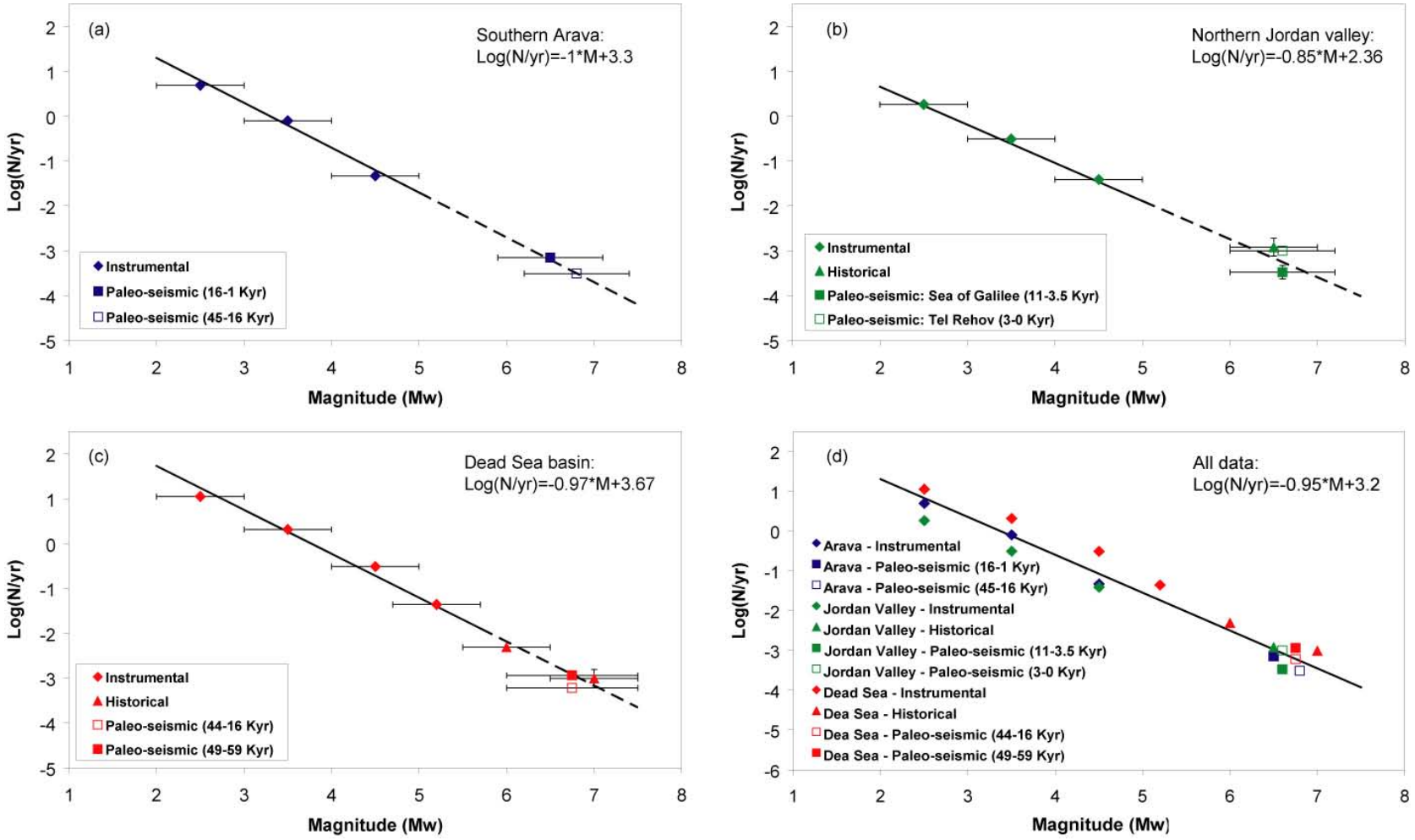

Figure 3: Frequency-magnitude relations for the southern Arava Valley segment (a), the northern Jordan Valley segment (b), the Dead Sea basin (c), and all three segments together (d), using instrumental (diamonds), historical (triangles), and paleo-seismic (squares) records. Black lines denote the regression curves for the instrumental record only (in a-c), and dashed lines denote its extrapolation. Black line in (d) denotes the best fitted model for all data. Note that *b*-value (the slope of the curve) of 0.95 can explain the whole data range for all three segments. (Hamiel et al., in press BSSA)

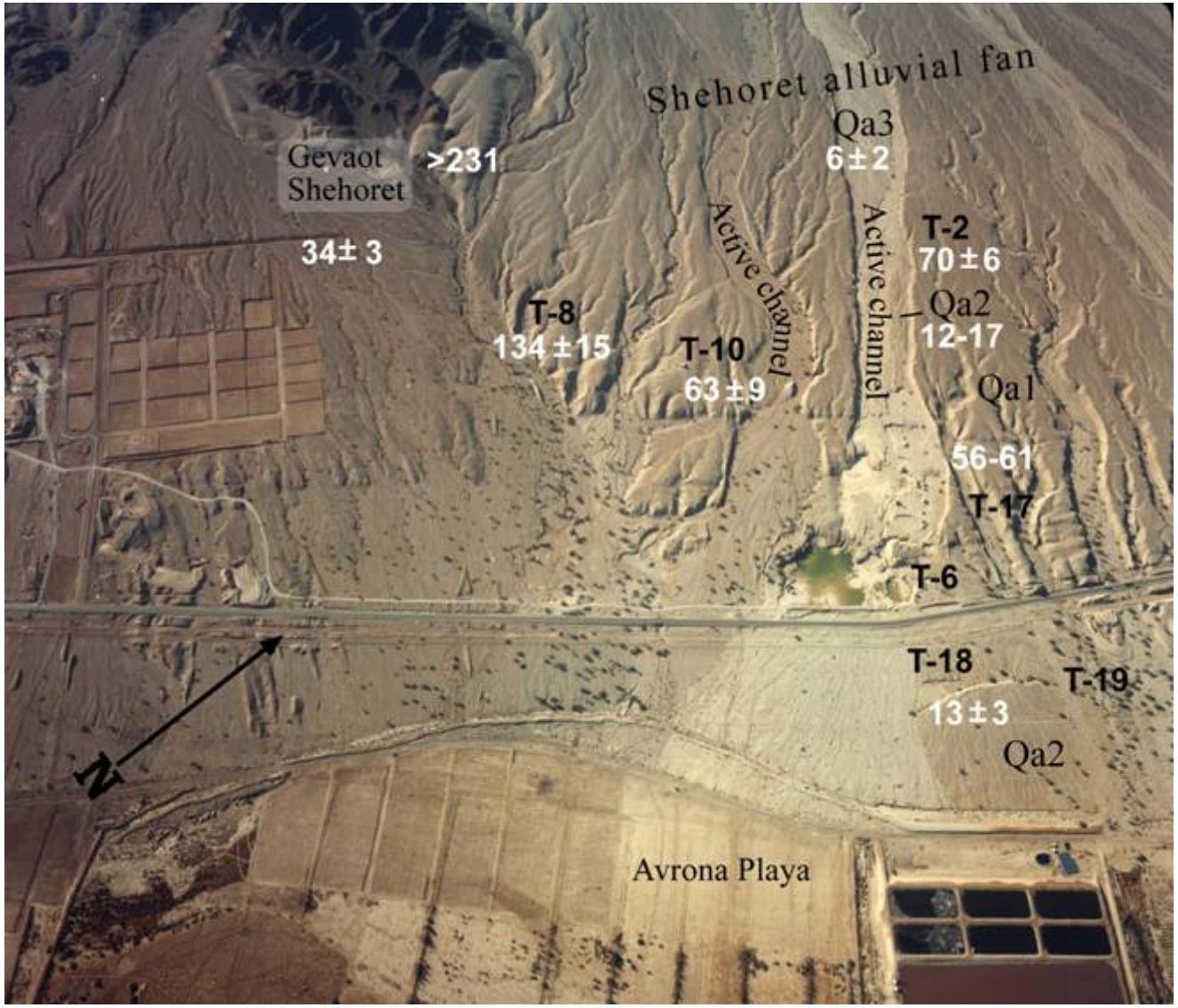

Figure 4: Arial photo of Shehoret alluvial fan. Notice the dated surfaces by OSL ages, trenches location and numbers.

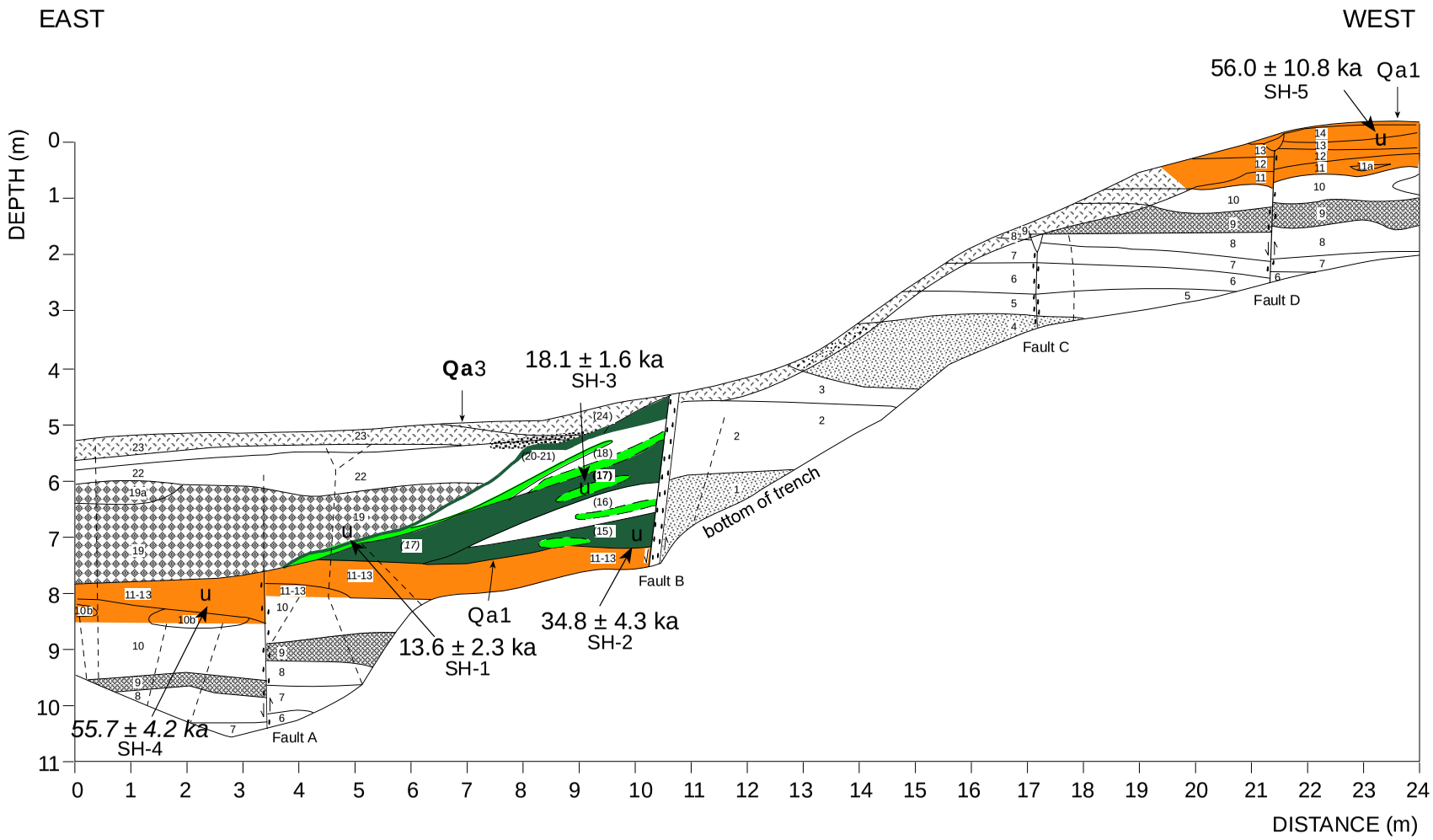

Figure 5: Log of the southern wall of trench T-6 across one of the faults that cross the marginal fault zone.

~ 1 m vertical displacement; Mw ~ 6.6

1.2 ± 0.3 ky

Last earthquake 1068 AD

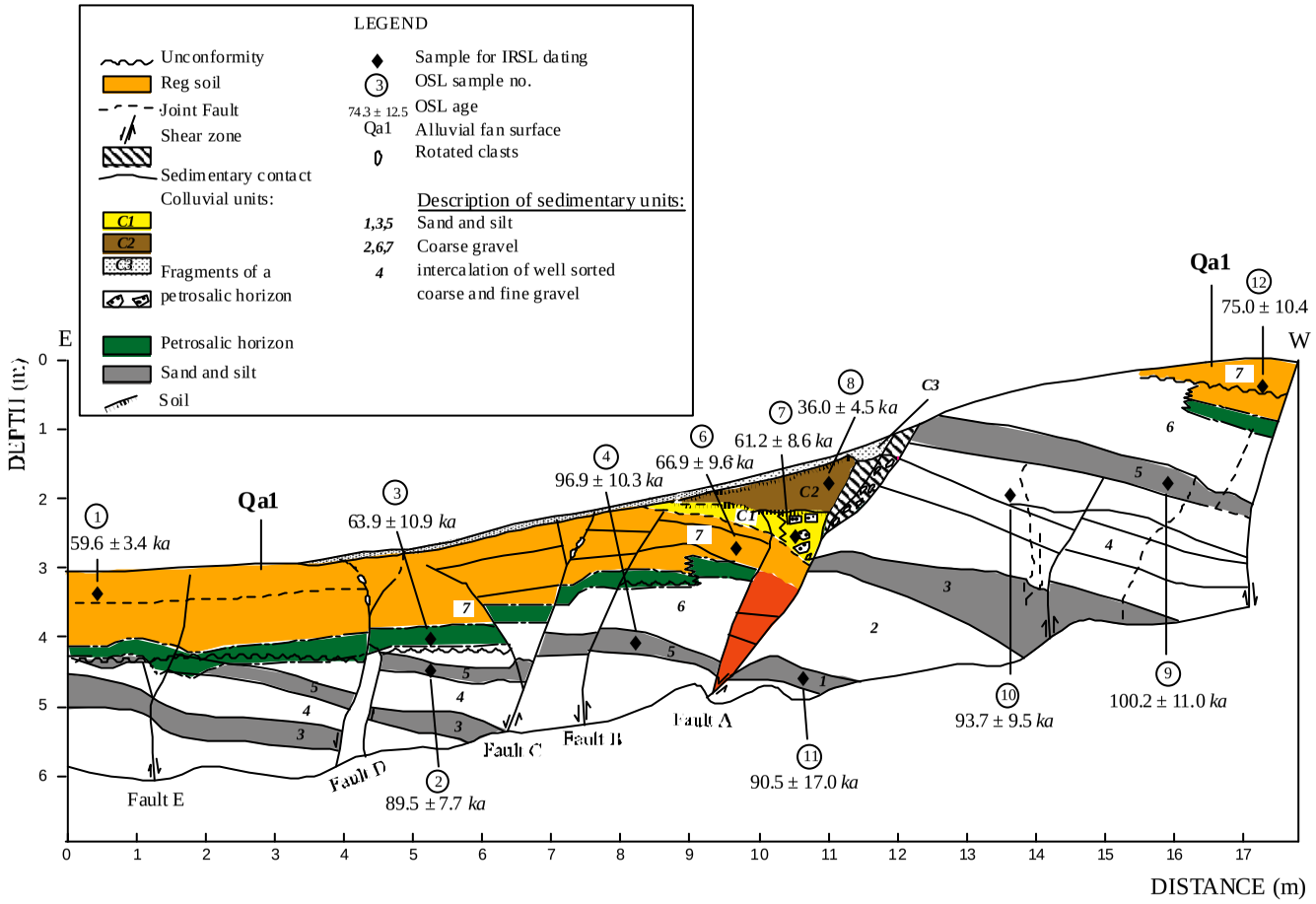

Figure 6: Log of the southern wall of trench T-17 across a fault scarp in the Avrona playa.

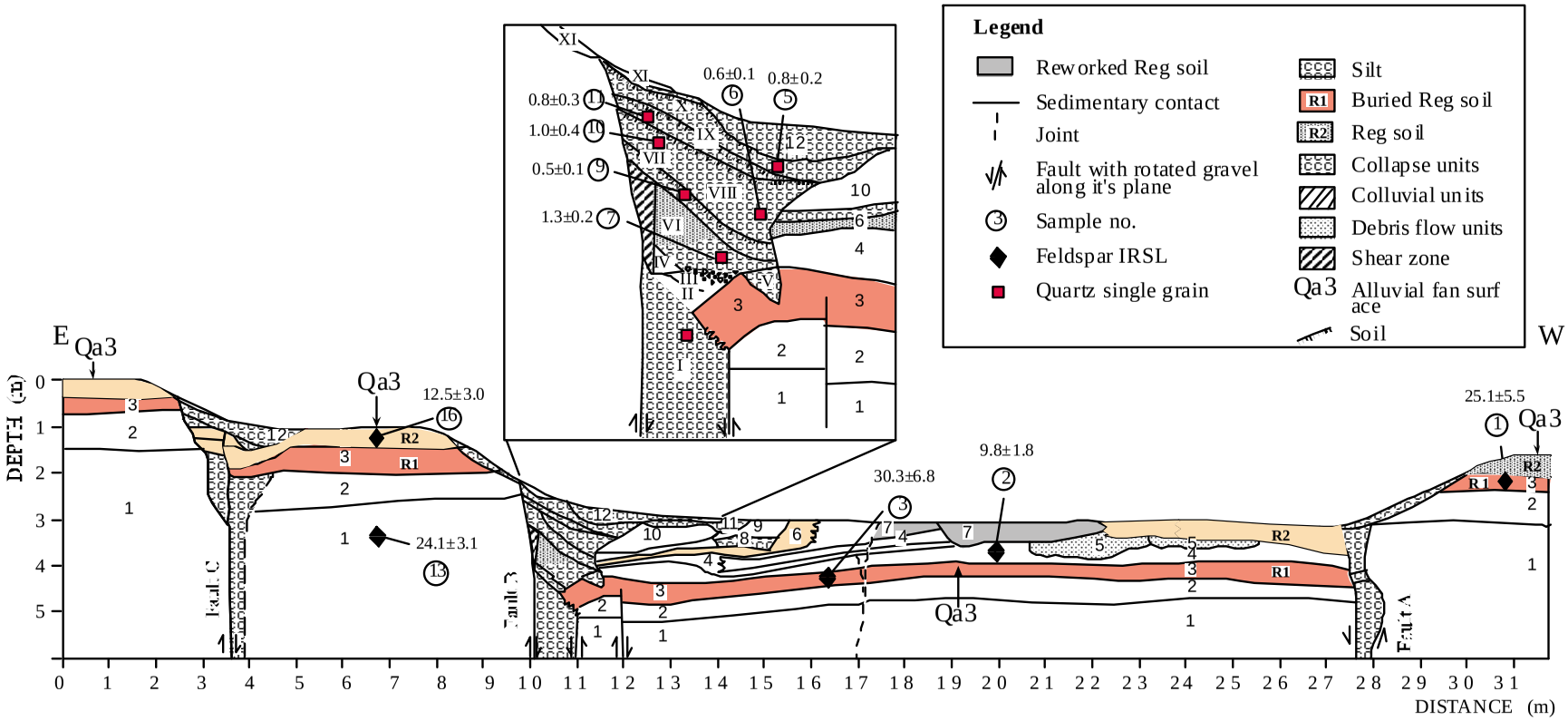

Figure 7: Log of the southern wall of trench T-18, showing a graben structure located in the central fault zone. The box shows details of area adjacent to fault B.

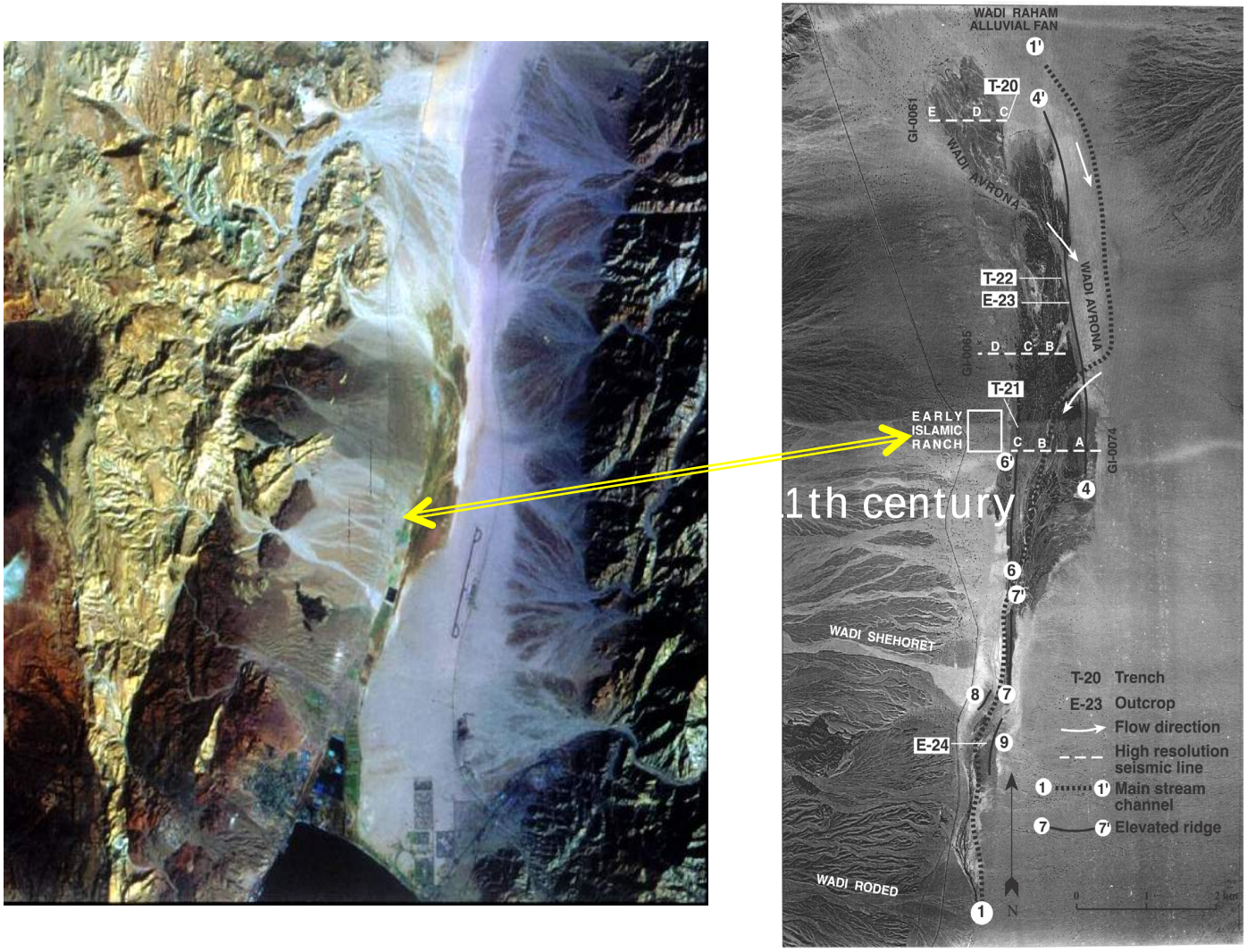

Figure 8: Air photos of the Avrona Playa showing the traces of photogrametric topographic profiles (circles) and the sites of the trenches and exposures (rectangles). The straight lineament that bounds and crosses the playa (dark area) represents a NNE-trending fault of the Avrona Shear Zone. This fault was trenched in T-20. The dark area bounded by straight lineaments corresponds to the uplifted sterile playa sediment. The light-tone areas mark the wide braided Wadi Avrona stream, which occupies a structural depression in the north and splits into several narrow and shallow streams within the playa area. The main faults are designated A-E; geophysical lines are labeled GI-0061, GI-0065 and GI-0074

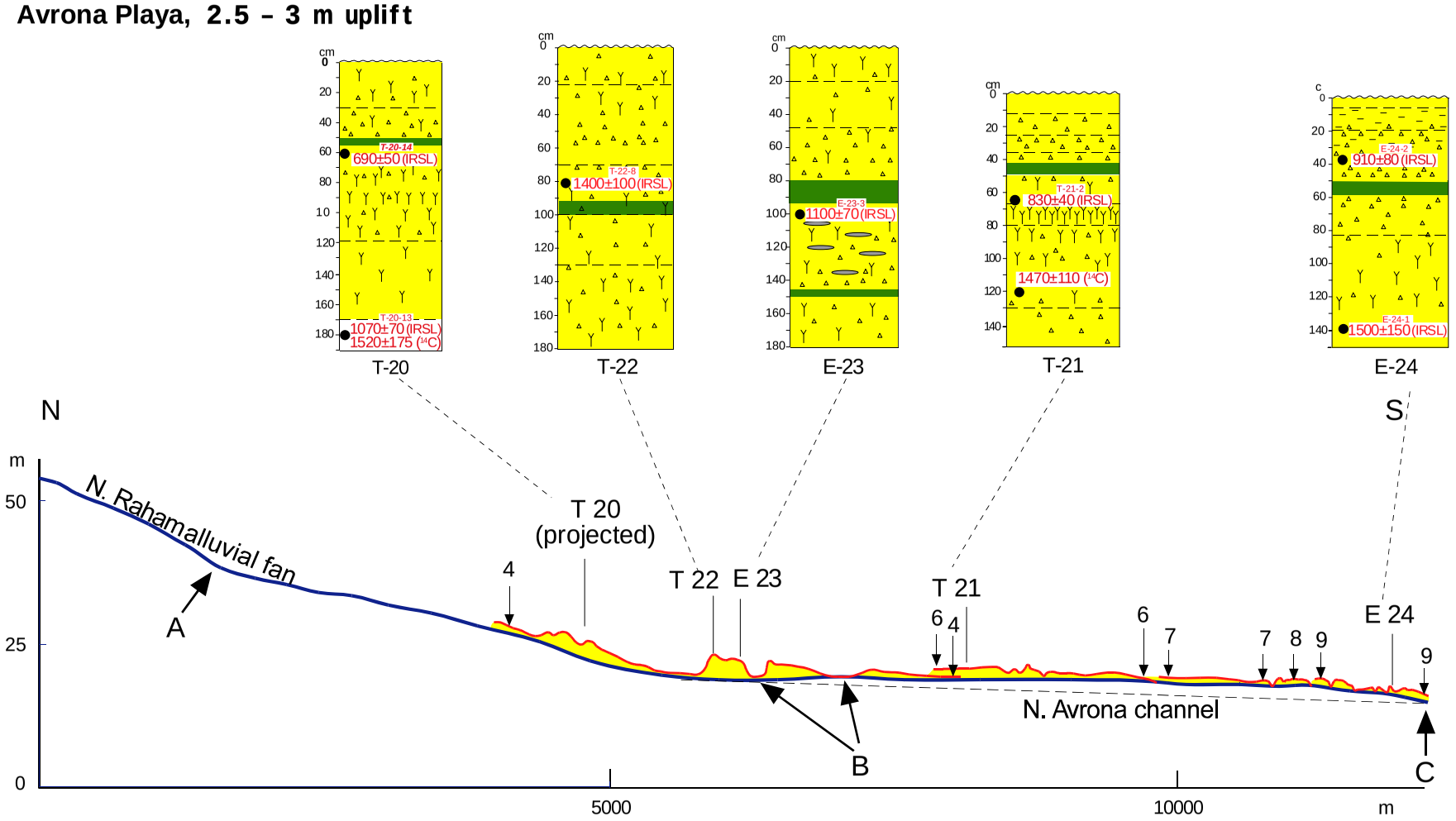

Figure 9: Composite topographic profiles of Wadi Avrona stream channel and the elevated sub-ridge across the playa area. Notice the nick point at A, where the stream crosses the fault that displaces the alluvial fan and the convex profile of the stream channel between points B and C, where the stream crosses the elevated ridge. Numbers refer to segments of the profiles. The soil and sedimentary profiles represent the upper 1.5 m of the elevated playa deposits showing similarity throughout the tectonically deformed area. Notice the petrosalic horizon which serves as a chrono-stratigraphic marker for correlating the elevated playa surface.

~ 1 m vertical displacement; Mw ~ 6.6

1.2 ± 0.3 ky

Last earthquake 1068 AD

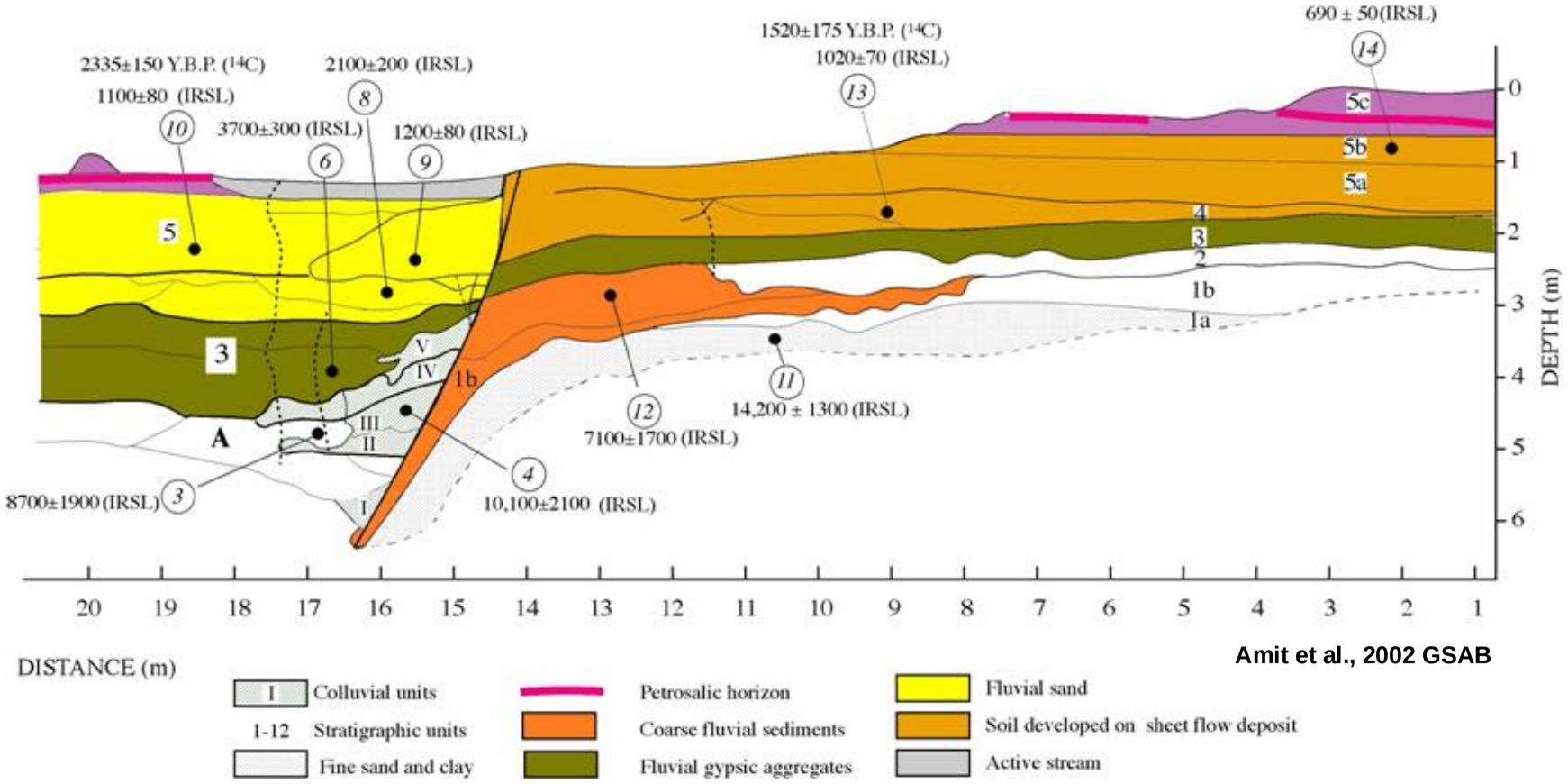

Figure 10: Log of the southern wall of trench T-20 across a fault scarp in the Avrona playa.

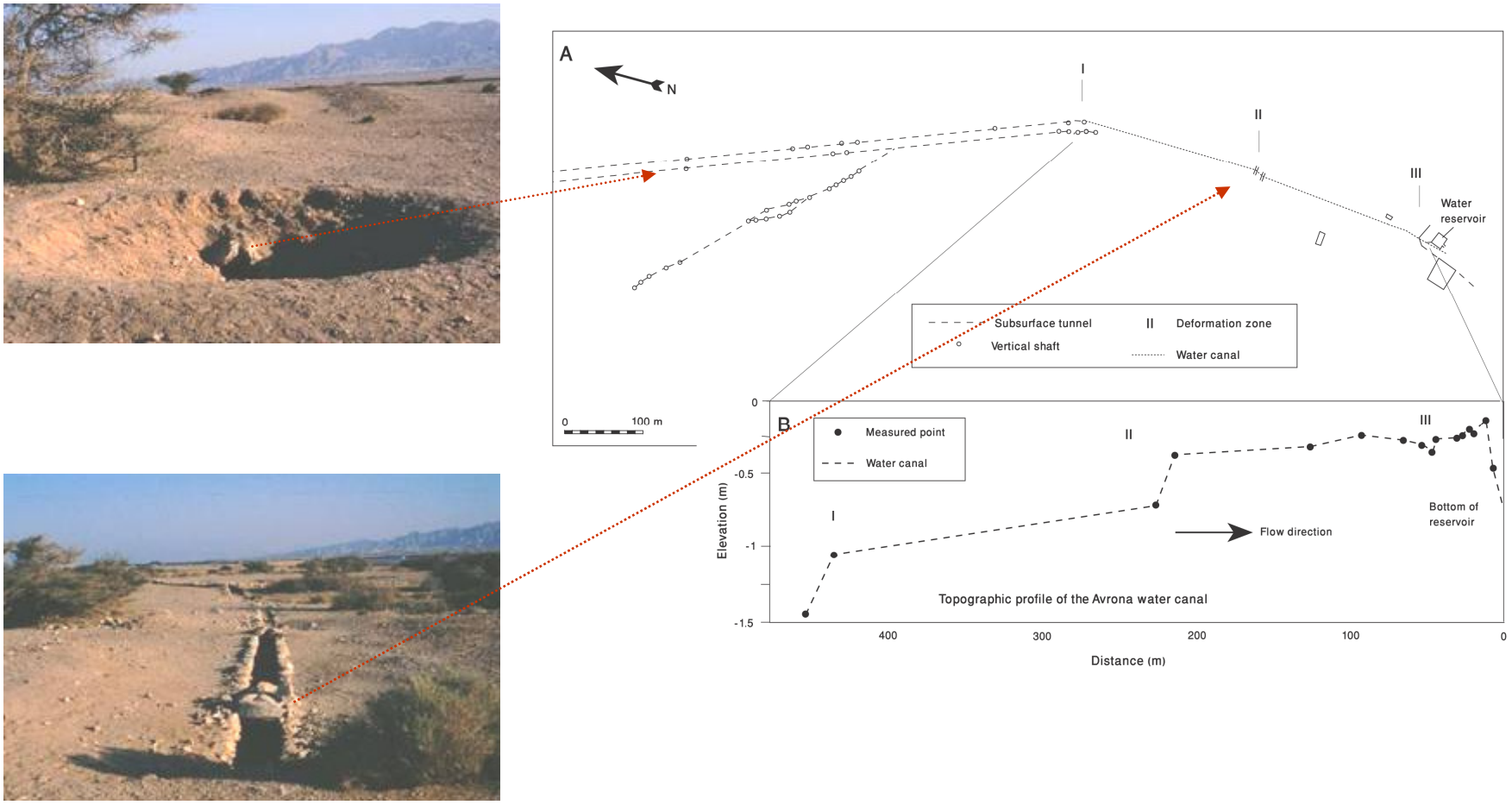

Figure 11: Topographic profile of the water canal in the Avrona Islamic farm. The profiles were measured by EDM total station.

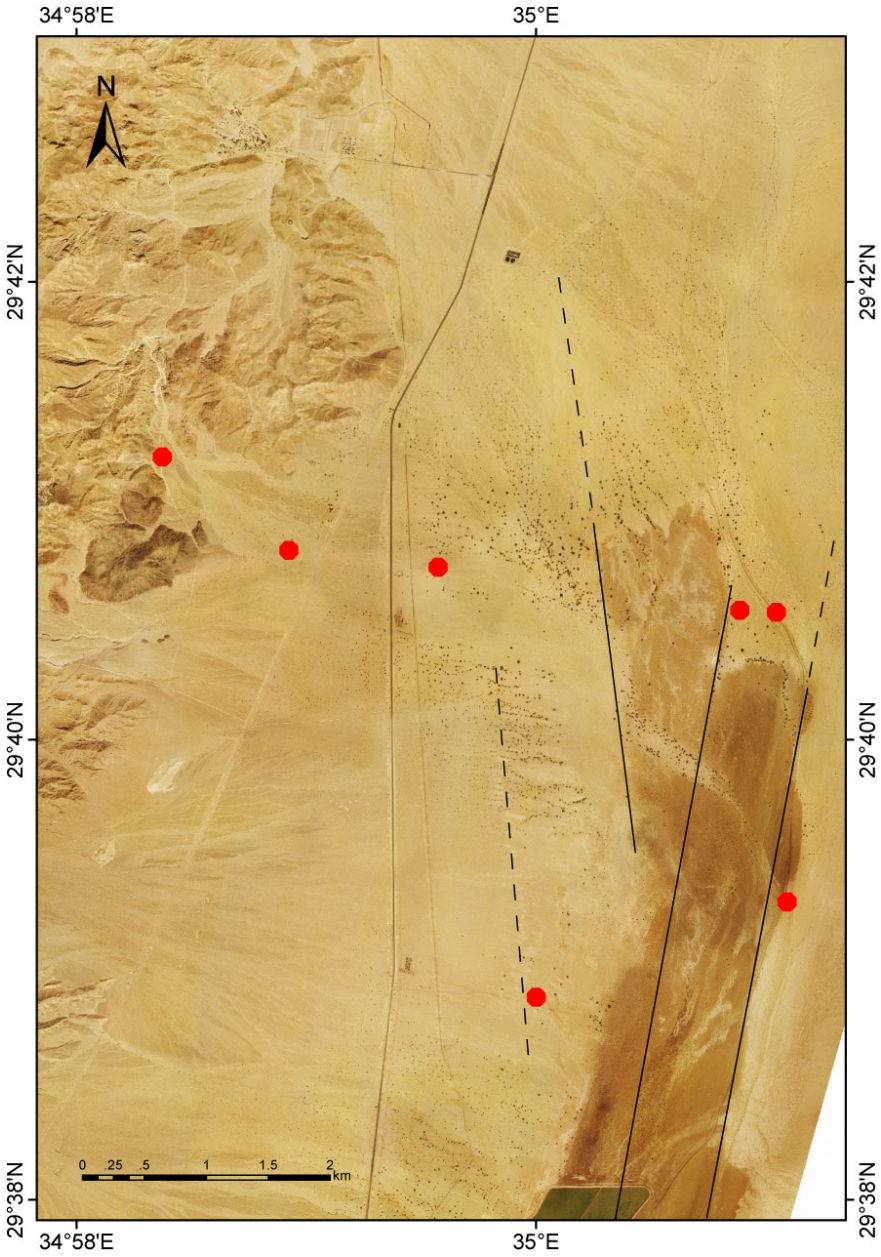

Figure 12: Red dote: location of GPS measurement

Table 1: Eilat fault zone data

Segment	Trench site	Event	Age, ka	Displacement, m	Cumulative displacement, m	Magnitude (M)	Reccurrence, kyr (average)	Slip rate mm/yr (average)		Time start point, ka	Dating methods
Marginal fault zone	T-8	1	84±6	3.5	3.5	7.0	—	—		—	OSL
	T-10	1	25±15	3	4	6.9	5±2	0.2		25	Soils and SLOPEAGE model
		2	15±5	0.7		6.5					
		3	10±5	0.2		6.1					
		4	5±1.5	0.1		5.9					
	T-6	1	37±3.7	1.6	7.6	6.7	3.8±0.6	0.3	0.25	37	OSL, Soils SLOPEAGE model
		2	32±3.4	1.5		6.7					
		3	30±3	1.6		6.7					
		4	18±1.6	1.5		6.7					
		5	16±1.6	0.4		6.3		0.2			
		6	14±1.4	0.5		6.4					
		7	10±5	0.5		6.4					
	T-17	1	45±2	1.5	3.4	6.7	6.6±1.4	0.3	0.2	45	OSL, Soils SLOPEAGE model
		2	36±4.5	1.5		6.7					
		3	5±2	0.4		6.3		0.1			
	T-16	1	36±9	0.5	Active channel	6.4	—	—		—	OSL
	T-15	1	8±2	0.5	0.5	6.4	8±2	0.1		8	Soils
Central fault zone	T-18	1	10±2	0.5	4	6.4	1±0.4	0.3		10	OSL, Soils SLOPEAGE model
		2	8±2	0.2		6.1					
		3	7±2	0.2		6.1					
		4	4.5±2	1.3		6.7					
		5	2.5±1	0.2		6.1					
		6	2±1	0.5		6.4					
		7	1.5±0.5	0.5		6.4					
		8	1±0.5	0.3		6.2					
		9	1±0.5	0.3		6.2					
	T-19	1	4.1±0.8	1	Active channel	6.6	—	—		—	OSL, Soils
	T-20	1	7.1±1.7	0.5	2	6.4	2±0.3	0.3		10	OSL, ^{14}C, Soils
		2	3.7±0.3	0.5		6.4					
		3	1.1±0.1	1		6.6					

Landscape development in an hyper arid sandstone environment along the margins of the Dead Sea fault: implications from dated rock falls

Ari Matmon[1*], Yony Shaked[1], Amotz Agnon[1], Naomi Porat[2], Yehouda Enzel[1], Robert Finkel[3], Nathaniel Lifton[4], and Boaretto Elisabetta[5]

[1]Institute of Earth Sciences, The Hebrew University of Jerusalem
[2]Geological Survey of Israel
[3]Lawrence Livermore National Laboratories
[4]Geosciences Department, University of Arizona, Tucson
[5]Weizmann Institute of Science

arimatmon@cc.huji.ac.il

*Field guide

In this study we explored the spatial and temporal relations between boulders and their original in-situ locations on sandstone bedrock cliffs. This was accomplished by combining field observations with dating methods using cosmogenic isotopes (^{10}Be and ^{14}C) and optically stimulated luminescence (OSL). Our conclusions bear both on the landscape evolution and cliff retreat process in the hyper-arid region of Timna and on the methodology of estimating exposure ages using cosmogenic isotopes.

Geological and morphological setting

Timna is located at the western margin of the southern Arava Valley, a hyper-arid region extending from the Dead Sea basin to the Gulf of Aqaba (Fig. 1). Timna is an uplifted core of late Precambrian igneous rocks (Druckman et al., 1993) overlain by Cambrian and lower Cretaceous clastic sediments. It is a bowl-shaped valley, about 8 km in diameter, and is surrounded by cliffs of upper Cretaceous limestone and dolomite rising up to 600 m above the valley floor.

Landscape development in the Timna area is controlled by the tectonic activity along the southern section of the DSF (Hannan Ginat, personal communication). Erosional truncation of the upper Cretaceous carbonate cap rocks during the Oligocene and Miocene exposed the more erodable lower Cretaceous sandstone. As the southern Arava Valley developed into a topographic base level, the sandstone was eroded and transported towards that base level, the Timna Valley was incised, and the Precambrian basement and Cambrian sediments were exposed at the base of the Timna Valley.

The Cambrian sandstone in Timna reaches a thickness of about 100 m (Druckman et al., 1993) and forms cliffs that dominate the landscape. Within the Cambrian sandstone terrain, erosion is dominated both by detachment of massive boulders from the sandstone cliffs and by slow weathering of the cliff faces, as evident from 0.1 m-scale cavities (tafoni). Generally, boulders detached from sandstone cliffs are found in piles, and are usually coated with varnish. In many

locations, the cliff face and the faces on the boulders match perfectly both in detail and overall morphology. Some of these boulders can be accurately traced to their original position on the cliff from which they were detached (Fig. 2).

We concentrated on three boulder sites in the Timna area (Figs. 1 and 3). The first, the Lower Valley, contains two boulder piles (one close to the source sandstone cliff face, which we call the "Closer Pile", and one farther away, the "Farther Pile") detached from a cliff that rises 10-14 m above the valley floor. The boulders at this site were deposited at the mouth of the Lower Valley (30X60 m), creating a dam, and causing upstream accumulation of sandy sediments on the valley floor. The second site, the Upper Valley, contains several boulder piles. We concentrated on a single boulder pile detached from a nearby 10 m cliff. At both locations boulders are not significantly affected by erosion and perfectly match the cliff faces (Fig. 2). Unlike the first two sites that contain unweathered boulder piles, the third site we examined contains three weathered boulders that are located at distances of 20, 14, and 4 meters from the source cliff.

Results

We recognize three discrete rock fall events, at 31 ka, 15ka, and 4ka (Figs. 4 and 5). In this hyper arid region the most plausible triggering mechanism for rock fall events is strong ground acceleration caused by earthquakes generated by the nearby Dead Sea fault (DSF). Our record, however, under represents the regional earthquake record implying that ongoing development of detachment cracks prior to the triggering event is slower than the earthquake cycle.

Cliff retreat rates calculated using the timing of rock fall events and estimated thickness of rock removed in each event range between 0.14 m ky^{-1} and 2 m ky^{-1} (Fig. 8) When only full cycles are considered, we derive a more realistic range of 0.4 m ky^{-1} to 0.7 m ky^{-1}. These rates are an order of magnitude faster than the calculated rate of surface lowering in the area. We conclude that sandstone cliffs at Timna retreat through episodic rock fall events that preserve the sharp, imposing, landscape characteristic to this region and that ongoing weathering of the cliff faces is minor.

A 10%-20% difference in the ^{10}Be concentrations in samples from matching boulder and cliff faces that have an identical exposure histories and are located only a few meters apart, indicate that cosmogenic nuclide production rates are sensitive to shielding and vary spatially over short distances. However, the uncertainties associated with age calculations for boulder and matching cliff face pairs yielded ages that are similar within 1 . The use of external constraints, in the form of field relations and OSL dating helped to establish each pair's age. The agreement between calculated ^{14}C and ^{10}Be ages indicates that the accumulation of ^{10}Be at depth by the capture of slow deep-penetrating muons was properly accounted for in the study.

Rock falls and earthquakes

Many processes, including tectonic, climatic, and environmental factors can cause rockslides (Wieczorek et al., 1996). Many of these factors can be eliminated in the case of rockslides in Timna. Snowmelt, freeze and thaw effects, ground water seepage, and tree root wedging can be ruled out due to the hot and hyper-arid conditions in the area. Although rain storms and the resulting expansion of clay and salt particles in cracks is a plausible mechanism, we would expect boulders to detach one at a time rather than in groups that form large piles as is the case in Timna. Furthermore, the frequency of clay and salt wetting events is not high enough to generate proper stress in the fractures to allow boulder release. Several observations, mainly the large size of the boulders (many of the boulders have at least one dimension longer then 5 meters) and the agreement in ages of boulder piles in the sampling locations suggest that each pile of boulders was detached from its source cliff in a single event. The proximity of Timna to the DSF, where >M6 earthquakes are common, suggests that ground shaking due to seismic events is the most likely cause for the Timna boulder slides.

Rock falls are sensitive recorders of strong ground motion resulting from earthquakes (Bull and Menges, 1977). Synchronous rock falls may indicate the occurrence of past earthquakes and rock fall timing may constrain earthquake recurrence intervals and magnitude. The relation between seismic events and the formation of boulders in rock falls is well established. A worldwide correlation between landslide size and distribution and variables such as earthquake magnitude and the specific ground-motion characteristics was determined by Keefer, (1984). A coseismic lichenometry model was developed in New Zealand following the discovery that lichens growing on rocky hill slopes recorded synchronous pulses of rock falls generated by historical earthquakes. The lichenometry model was used to date boulders and rock falls associated with earthquakes (Bull, 1996a,b; Bull et al., 1994; Kong, 1994; Smirnova and Nikonov, 1990).

Current measurements in the southern Arava Valley along the DSF system show no seismic activity (Shapira, 1997). However, historical evidence documents several large seismic events (Ambraseys, 1994; Amiran, 1994; Fig. 6). Paleoseismic studies in the southern Arava Valley suggest that late Pleistocene earthquakes ranged in magnitude between 6.7 and 7.1 and the average recurrence interval was 2.8±0.7 ky (Amit et al., 2002). These studies indicate that Holocene earthquakes were more frequent, with an average recurrence interval of 1.2±0.3 ky, but with smaller magnitudes that ranged between M5.9 and M6.7. Several studies in the northern Arava Valley also suggest frequent Holocene and late Pleistocene seismic activity (Amit et al., 1996; Ambraseys, 1994; Ken-Tor et al., 2001; Migowski et al., 2004; Enzel et al., 1996; Gluck et al., 1999).

The time interval between the three boulder forming events recorded in this study is much longer than the recurrence interval of >M6 earthquakes in the region. However, this discrepancy does not

rule out seismic motion as the mechanism for the boulder formation. We suggest that the interval between boulder forming events represents the time that is necessary for fractures to develop to the point of minimum friction between boulders and bedrock (Fig. 7). During this time, earthquakes occur and gradually enhance the opening of fractures that surround boulders. Once these fractures are sufficiently developed, the next major earthquake releases the boulders. The spacing between the fractures determines the thickness of collapsed wall during each rock fall event and the level of sandstone lithification determines the resistance of the fresh exposed rock to weathering. Continued study of additional rock piles at Timna may help better constrain the temporal frequency of rock fall events, and improve the correlation between rock falls and earthquakes.

Conclusions

The combined ages of boulders from the three investigated sites suggest that they were deposited in three events at 31 ka, 15 ka, and 4 ka. The most likely mechanism for boulder formation in this tectonically active hyper-arid region is by tectonically induced ground motion. Paleoseismic studies in the area suggest a recurrence interval of 1000-2000 yr for earthquakes >M6. The cosmogenic and OSL age dating of the boulders suggests that boulder-formation events do not occur as frequently as >6M earthquakes occur in this area Therefore, it is apparent that boulder falls in the study area do not represent a full seismic record. We suggest that boulder formation events occur during earthquakes only after blocks of rock are sufficiently separated from bedrock by large and well-developed cracks. These cracks allow the detachment of the boulders when the next earthquake occurs.

Cliff retreat rates determined from the rock falls in Timna range between 0.14 and 2 m ky^{-1}. A more constrained range of 0.4 to 0.7 m ky^{-1} is calculated from the complete collapse cycles. These retreat rates are similar to those calculated in other arid regions. Field observations suggest that the retreat occurs mainly during rock fall events and that continuous weathering of the rock faces is less important. Since cliff retreat rates in Timna are an order of magnitude larger than the calculated rate of surface lowering, as calculated in the Lower Valley site, the sharp and imposing landscape characteristic to this region is preserved.

References

Ambraseys, N.N., C.P. Melville, R.D. Adams, The seismicity of Egypt, Arabia, and the Red Sea - A historical review, Cambridge University Press, Cambridge, UK, (1994), 181 p.

Amiran, D., Earthquakes in Israel, Qadmoniot 29 (1994) 53-61.

Amit, R., E. Zilberman, Y. Enzel, N. Porat, Paleoseismic evidence for time dependency of seismic response on a fault system in the southern Arava Valley, Dead Sea rift, Israel, Geol. Soc. Am. Bull. 114 (2002) 192-206.

Amit, R. J.B.J. Harrison, Y. Enzel, N. Porat, Soils as a tool for estimating ages of Quaternary fault scarps in a hyper arid environment - the southern Arava Valley, the Dead Sea rift, Israel, Catena 28 (1996) 21-45.

Bull, W.B., C.M. Menges, Geomorphic evidence for Holocene faulting in the central Mojave Desert, California, GSA, Abstr. Programs 9 (1977) 915.

Bull, W.B., Dating San-Andreas faults with lichenometry, Geology 24 (1996a) 111-114.

Bull, W.B., Prehistoric earthquakes on the Alpine Fault, New Zealand, J. Geophys. Res. 101 (1996b) 6037-6050.

Bull, W.B., P.N. J. Ki, F. Kong, T. Moutoux, W.M. Phillips, Lichen dating of coseismic landslide hazards in alpine mountains, Geomorphology 10 (1994) 253-264.

Druckman,Y., T. Weissbrod, Z. Garfunkel, Geological map of Israel, scale 1:100,000, sheets 25,26, Yotvata and Elat, (1993) Geol Surv. Isr.

Enzel, Y., R. Amit, N. Porat, E. Zilberman, J.B.J. Harrison, Estimating the ages of fault scarps in the Arava, Israel, Tectonophys. 253 (1996) 305-317.

Gluck, D., Y. Enzel, A. Heimann, Late Pleistocene and Holocene earthquakes at the southwestern margin of the Dead Sea Basin, Israel, EOS, Trans. Am. Geophys. Union 80 (1999) Suppl. 1024.

Keefer, D.K., Landslides caused by earthquakes, Geol. Soc. Am. Bull. 95 (1984) 406-421.

Ken-Tor, R., A. Agnon, Y. Enzel, M. Stien, S. Marco, J.F.W. Negendank, High resolution geological record of historic earthquakes in the Dead Sea basin, J. Geophys. Res. 106 (2001) 2221-2234.

Kong, F., Analysis of lichen size data for dating and describing prehistorical seismic shaking, M.S. thesis, University of Arizona, Tucson, (1994).

Migowski, C., A. Agnon, R. Bookman (Ken-Tor), J.F.W. Negendank, M. Stein, Recurrence pattern of Holocene earthquakes along the Dead Sea Transform revealed by varve-counting and radiocarbon dating of lacustrine sediments, Earth Planet. Sci. Lett. 222 (2004) 301-314.

Shapira, A., Seismicity pattern of the Dead Sea transform - A review, Dead Sea, Israel, in: 13th GIF meeting on the Dead Sea rift as a unique global site, Proc., (1997), 160 p.

Smirnova, T.Y., A. Nikonov, A revised lichenometric method and its application dating great past earthquakes, Arctic and Alpine Res. 22 (1990) 375-388.

Wieczorek, G.F., J.B. Snyder, R.B. Waitt, M.M. Morrissey, R.A. Uhrhammer, E.L. Harp, R.D. Norris, M.I. Bursik, L.G. Finewood, Unusual July 10, 1996, rack fall at Happy Isles, Yosemite National Park, California, Geol. Soc. Am. Bull. 112 (1996) 75-85.

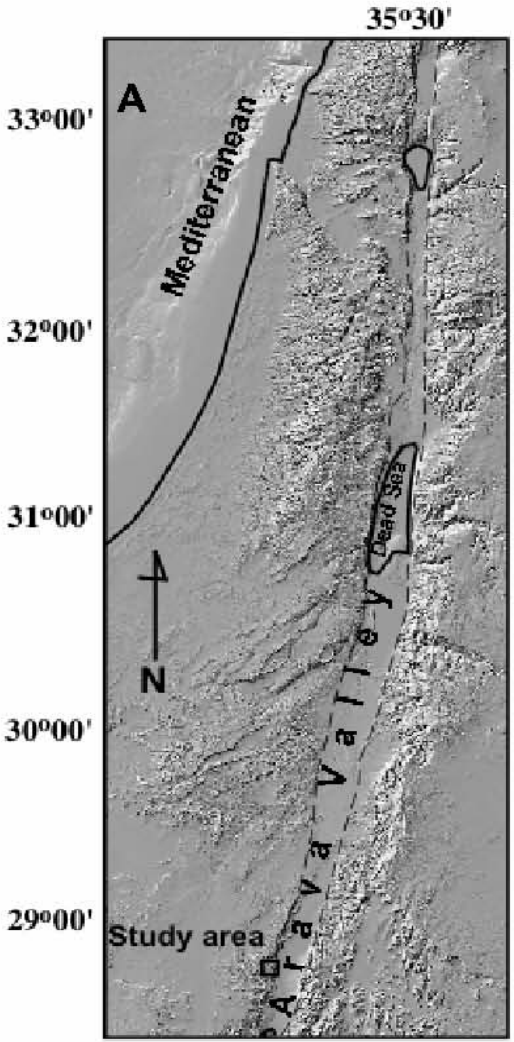

Study area location. A. DEM of Dead Sea fault (DSF) region. B. Aerial photo of the study area.

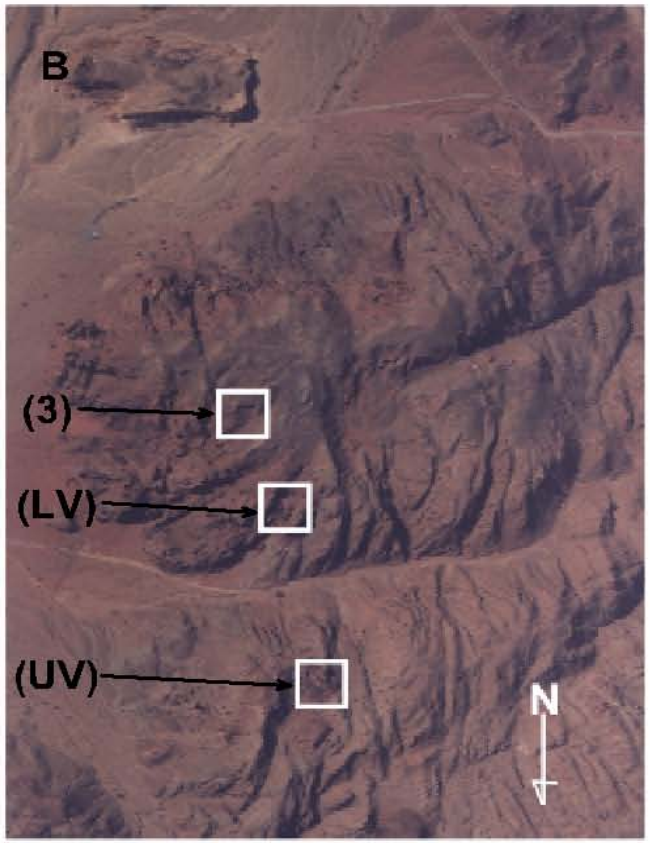

Open white squares indicate sampling sites

Timna is located at the western margin of the southern Arava Valley, a hyper-arid region extending from the Dead Sea basin to the Gulf of Aqaba. Timna is an uplifted core of late Precambrian igneous rocks [Druckman et al., 1993] overlain by Cambrian and lower Cretaceous clastic sediments. Within the Cambrian sandstone terrain, erosion is dominated by detachment of massive boulders from the sandstone cliffs and by slow weathering of the cliff faces, as evident from 0.1 m-scale cavities (tafoni).

Figure 1

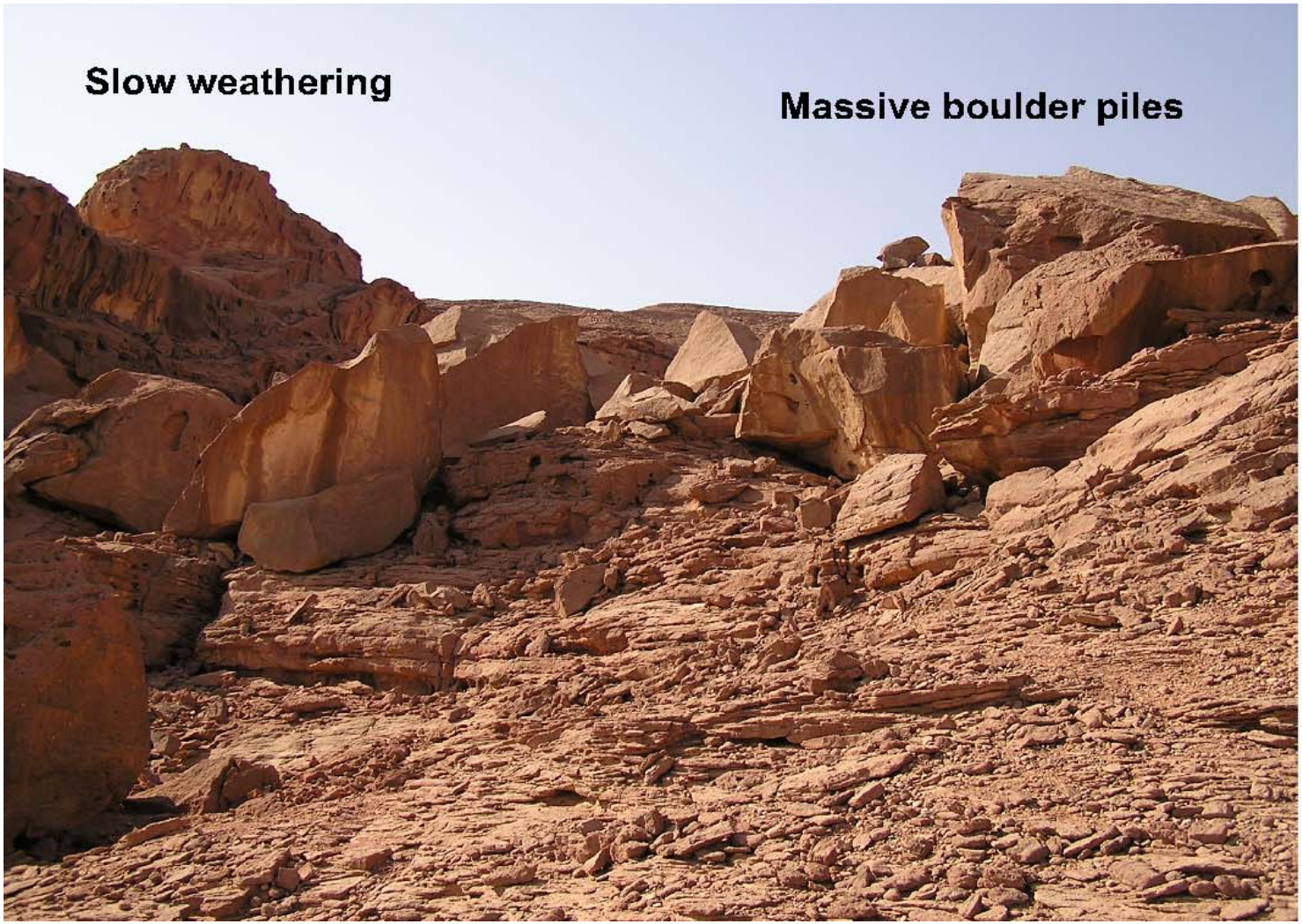

A. Small quartzite pebbles on the boulder face can be matched to cavities on the cliff face and vice versa. B. The relief of fracture ribs is apparent on a sampled boulder. Both examples indicate insignificant erosion of boulders since detachment.

Figure 2

We assume a relatively simple, two stage, cosmogenic nuclide accumulation history of the sampled boulders and cliff faces in Timna: the first stage, prior to detachment, when each sampled boulder and its source cliff were identically shielded and accumulated similar amounts of cosmogenic nuclides, and the second stage, after detachment,when cosmogenic nuclides accumulated at surface production rates which were reduced differently for the boulder and the cliff face because of differences in topographic shielding and geometry. Cosmogenic nuclide concentrations can be interpreted in terms of the exposure age of the boulders and cliff faces:

$$N_{measured} = \frac{P_{eff}}{\lambda}(1 - e^{-\lambda t}) + (N_{inherited})e^{-\lambda t} \qquad (1)$$

We estimated the pre-detachment accumulation of ^{10}Be, produced at depth mainly by muons, following Granger and Muzikar [2001]:

$$N_{Be} = \frac{B_0}{\frac{1}{\tau_{Be}} + \frac{E\rho}{L_0}} + \frac{B_1}{\frac{1}{\tau_{Be}} + \frac{E\rho}{L_1}} + \frac{B_2}{\frac{1}{\tau_{Be}} + \frac{E\rho}{L_2}} + \frac{B_3}{\frac{1}{\tau_{Be}} + \frac{E\rho}{L_3}} \qquad (2)$$

where B_i is the production in atoms g^{-1} yr^{-1}, L_i is the attenuation length in g cm^{-2} (B_1=0.0055, B_2=0.0137, and B_3=0.0187. L_0 = 165 g cm^{-2}, L_1 = 738 g cm^{-2}, L_2 = 2688 g cm^{-2}, and L_3 = 4360 g cm^{-2}. r = 2.2 g cm^{-3}), E is the surface lowering rate in cm yr^{-1}, ρ is the rock density in g cm^{-3}, and τ_{Be} is the mean life of ^{10}Be (2.18+/-0.09 My). In both the Upper and Lower Valley sites, the source cliff face rises ~10 m above the sample. Therefore, we calculated the accumulation of ^{10}Be at depth assuming steady erosion rate of the upper surface and a minimum depth of 10 m.

Production by nucleons is insignificant at depths of 10 meters and more. Therefore, the first term in equation (2) is insignificant. Sea level, high-latitude (SLHL) production of ^{10}Be by muons is calculated to be 0.116 atoms g^{-1} yr^{-1} for negative muons and 0.026 atoms g^{-1} yr^{-1} for fast muons [Granger and Smith, 2000]. Production rates are scaled for local atmospheric shielding using an atmospheric attenuation length of 240 g cm^{-2}. A resulting scaling factor of 1.19 is determined from the average barometric pressure in the Timna area. The production rate at a depth of 10 m is calculated using [Granger and Muzikar, 2001]. We estimate the predetachment accumulation at 17.41.4)X10^3 atoms (g quartz) $^{-1}$. The similarity in ^{10}Be and ^{14}C ages from boulder Timna 2 indicates that our estimate is good.

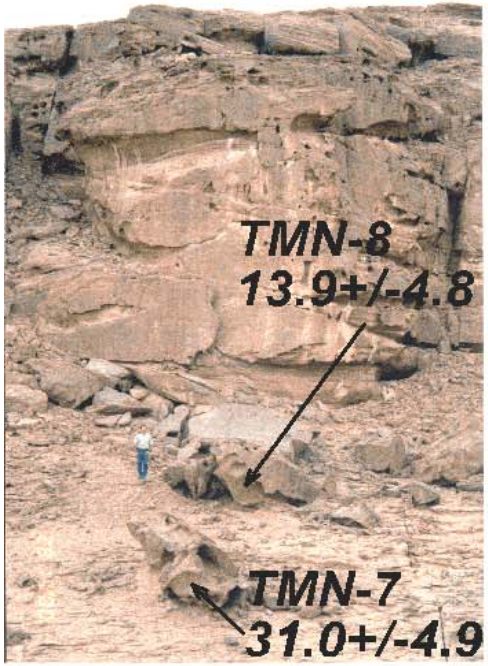

We concentrated on three boulder sites in the Timna area . The first, the Lower Valley, contains two boulder piles detached from a cliff that rises 10-14 m above the valley floor. The boulders at this site were deposited at the mouth of the Lower Valley (30X60 m), creating a dam, and causing upstream accumulation of sandy sediments on the valley floor. At the second site, the Upper Valley, we concentrated on a single boulder pile detached from a nearby 10 m cliff. At the third site we examined three weathered boulders that are located at distances of 20, 14, and 4 meters from the source cliff.

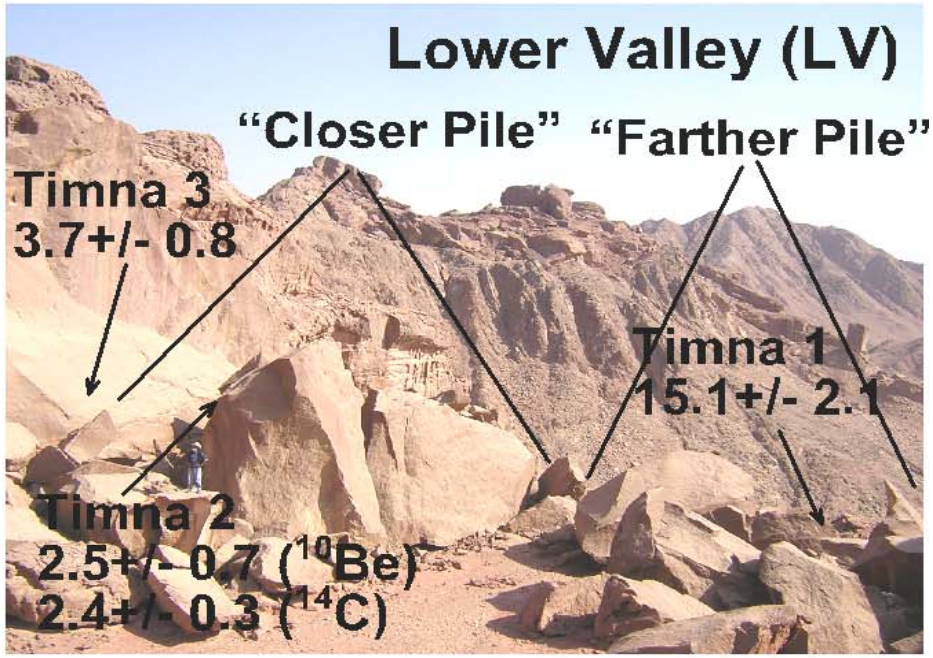

(all ages are in ky)

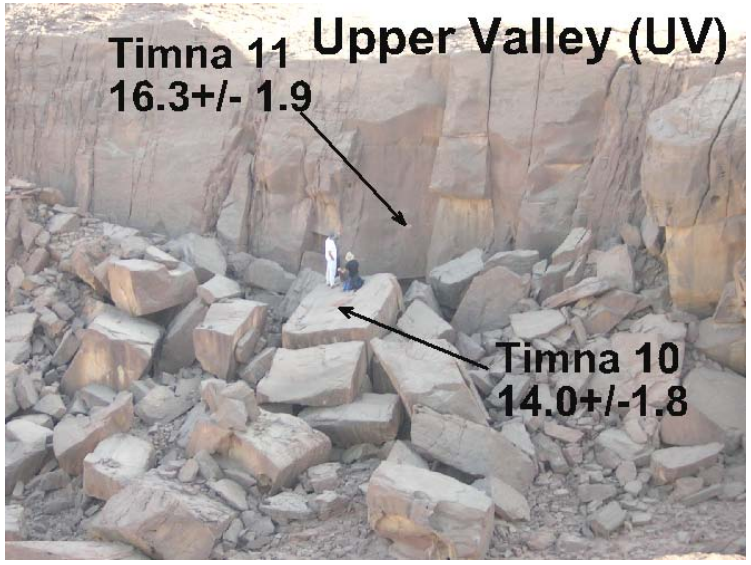

Figure 3

Cosmogenic ^{10}Be and ^{14}C results for boulders and cliff face samples from Timna Valley

Sample Name	Measured ^{10}Be (10^3 atoms g^{-1})	Un-corrected ^{10}Be age[a] (ka)	Measured ^{14}C (10^3 atoms g^{-1})	Total scaling factor[b]	^{10}Be Erosion rate (mm ky^{-1}) [a]	^{10}Be Peff (atoms g^{-1} yr^{-1}) [c]	Corrected ^{10}Be age[d] (ka)	^{14}C age[e] (ka)
] [[								
Timna 1	55.3±3.3	18.4±2.2		0.46		2.52	15.1±2.1	
Timna 2	28.3±2.3	10.4±1.3	32.9±4.0	0.80		4.33	2.5±0.7	2.4±0.3
Timna 3	34.1±2.7	11.8±1.5		0.84		4.53	3.7±0.8	
] [[								
Timna 10	49.2±2.0	17.6±1.9		0.42		2.28	14.0±1.8	
Timna 11	54.6±2.0	17.7±1.9		0.42		2.30	16.3±1.9	
] [[								
Timna 20	239.3±8.0			1	20.7±2.2			
Timna 21	180.2±6.3			1	27.9±2.9			

[a] Model un-corrected ages and erosion rates were calculated using a SLHL ^{10}Be production rate of 5.37 atoms g^{-1} yr^{-1} [Schaller et al., 2001]. SLHL production rate was scaled for latitude and altitude using Lal [1991] for nucleonic production, Granger and Smith [2000] for muonic production, and Pigati and Lifton [2004] for paleomagnetic intensity variations. Site surface production rate of 5.42 atoms g^{-1} yr^{-1} was calculated. Attenuation of muons in the atmosphere was scaled to the sites elevation using a factor of 1.19. Sample density: 2.2 g cm^{-3}.

[b] Total scaling factor includes: (1) topographic shielding factor which was measured for each sample in 8 major directions and calculated using Dunne et al. [1999]. Following Masarik and Weiler [2003], boulder geometry factor was calculated for boulder sample Timna 2 (6%) and boulder sample Timna 10 (2%).

[c] ^{10}Be Peff calculated by multiplying site's surface production rate (5.42 atoms g^{-1} yr^{-1}) by the total scaling factor.

[d] Corrected age calculated considering the pre-detachment production of ^{10}Be at depth mainly by muons (17.4+/-1.4 atoms g^{-1}; see text for explanation), and using ^{10}Be Peff. Cosmogenic age uncertainties include analytical errors and a 10% uncertainty in production rate.

[e] Age calculated using a sea level, high latitude production rate of 16.1+/-0.2 atoms g^{-1} yr^{-1} and a spallogenic/ muogenic ratio of 0.83:0.17 [Heisenger et al., 2002].

Sample	Location	Depth (m)	K (%)	U (ppm)	Th (ppm)	ext. ! (∝Gy/a)	Ext. _ (∝Gy/a)	Cosm. (∝Gy/a)	Ext. ∀ +cosm. (∝Gy/a)[2]	De (Gy)[1]	# of aliquots[3]	Dose rate (∝Gy/a)[4]	Age (ka)
TMN-1	Pit – 1 (Lower Valley, Farther pile)	0.15	1.5	1.4	8.5	1429	914	253		11.1±2.3	17/18	2607±49	4.3±0.9
TMN-2	Pit – 1 (Lower Valley, Farther pile)	0.3	1.3	0.9	6.6	1208			1146	14.9±1.7	10/16	2361±119	6.3±0.8
TMN-3	Pit – 2 (Lower Valley, Closer pile)	0.1	2.4	1.4	7.5	2047	1088	264		11.0±2.0	9/13	3409±53	3.2±0.6
TMN-4	Pit – 2 (Lower Valley, Closer pile)	0.5	2.3	1.4	7.6	1980			1463	18.0±3.5	18/33	3453±151	5.2±1.0
TMN-5	Modern sediment (Lower Valley)	0								0.3±0.5		~ 3000	0.1
TMN-7	Boulder – (Third site, 20 meters from cliff)	1.2	1.1	0.7	4.7	963			848	57±8.5	10/12	1817±88	31.0±4.9
TMN-8	Boulder – (Third site, 14 meters from cliff)	2.7	2.5	1.0	6.5	2030			1045	40±14	10/12	3084±109	13.9±4.8

Notes: [1]De was measured on the 88-125 ∝m fraction of quartz grains using a Single Aliquot Regenerative Dose (SAR) protocol.
[2]∀and cosmic radiation were measured in the field or calculated from radioisotope contents and the cosmic dose estimated from burial depth. Because of the high dose rates the ages are not sensitive to the estimated cosmic dose.
[3]The number of aliquots used for De calculations out of the measured aliquots.
[4]Including an _ dose contribution of 8-10 ∝Gy/a.

Samples Timna 20 and Timna 21 were collected from the upper surface above the Lower Valley. Assuming steady rate erosion, these samples yield an average erosion rate of 24.3+/-3.6 mm ky^{-1}.

Figure 4

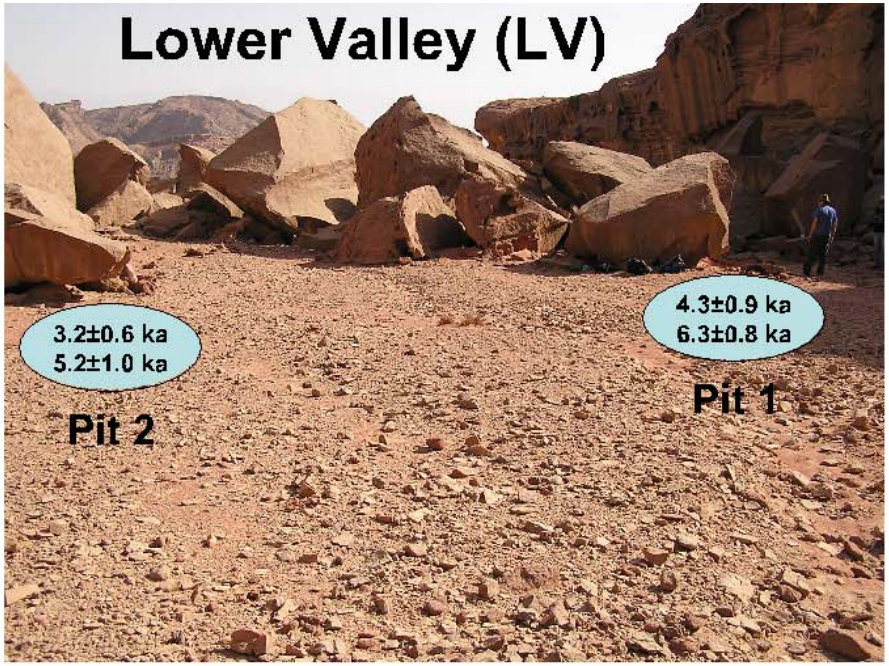

Samples for OSL dating were collected from the Lower Valley site and from the third site. Two shallow pits were dug in the sediments that accumulated upstream of the boulders in the Lower Valley site: Pit-1 behind the "Farther Pile" and pit-2 behind the "Closer Pile". The pits were dug down to bedrock. Samples were collected at depths ranging from 0.15 to 0.5 m. In the third site, samples were collected from beneath each one of the boulders.

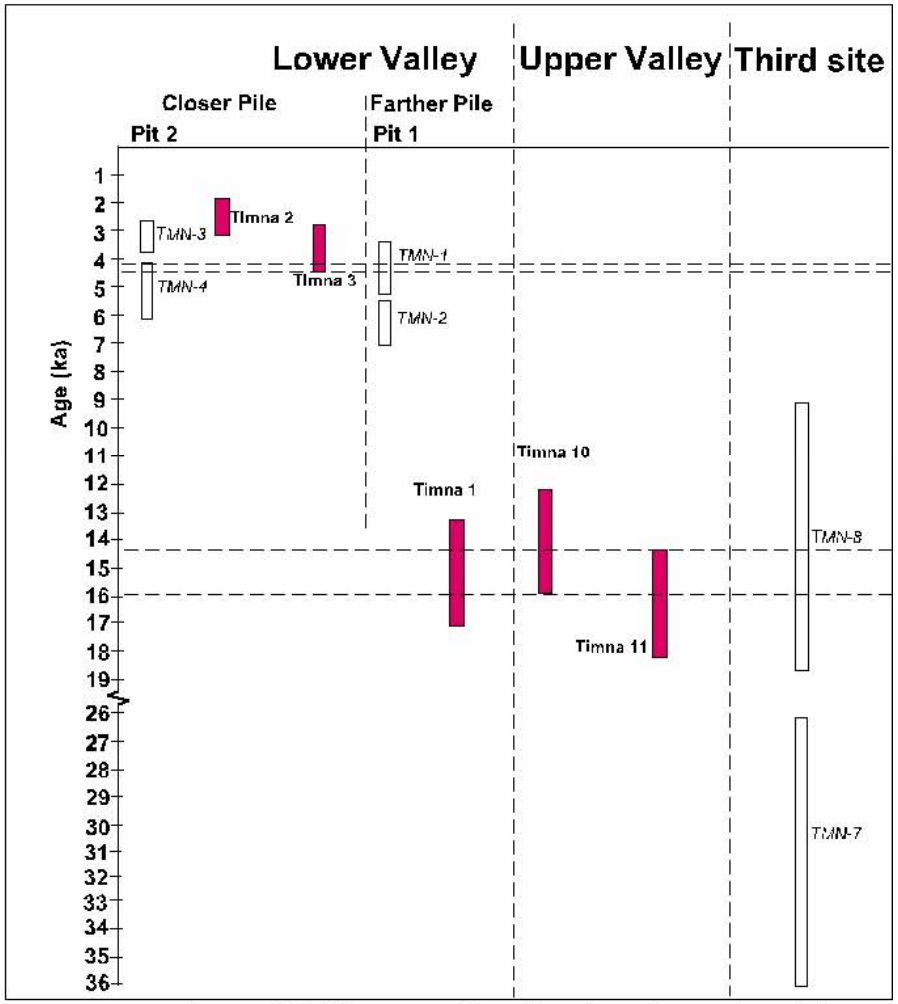

Cosmogenic and OSL age distribution from boulders, cliff faces and sediment in the three studied sites in Timna.

Figure 5

Many processes, including tectonic, climatic, and environmental factors can cause rockfalls [Wieczorek et al., 1996]. Most can be eliminated inTimna. Snowmelt, freeze and thaw effects, ground water seepage, and tree root wedging can be ruled out due to the hot and hyper-arid conditions in the area. The frequency of rain storms and the resulting expansion of clay and salt particles in cracks is too low to generate proper stress and allow boulder release. Several observations, mainly the large size of the boulders and the age clustering of boulder piles in the sampling locations suggest that each pile of boulders was detached from its source cliff in a single event. The proximity of Timna to the DSF, where >M6 earthquakes are common, suggests that ground shaking due to seismic events is the most likely cause for the Timna boulder slides.

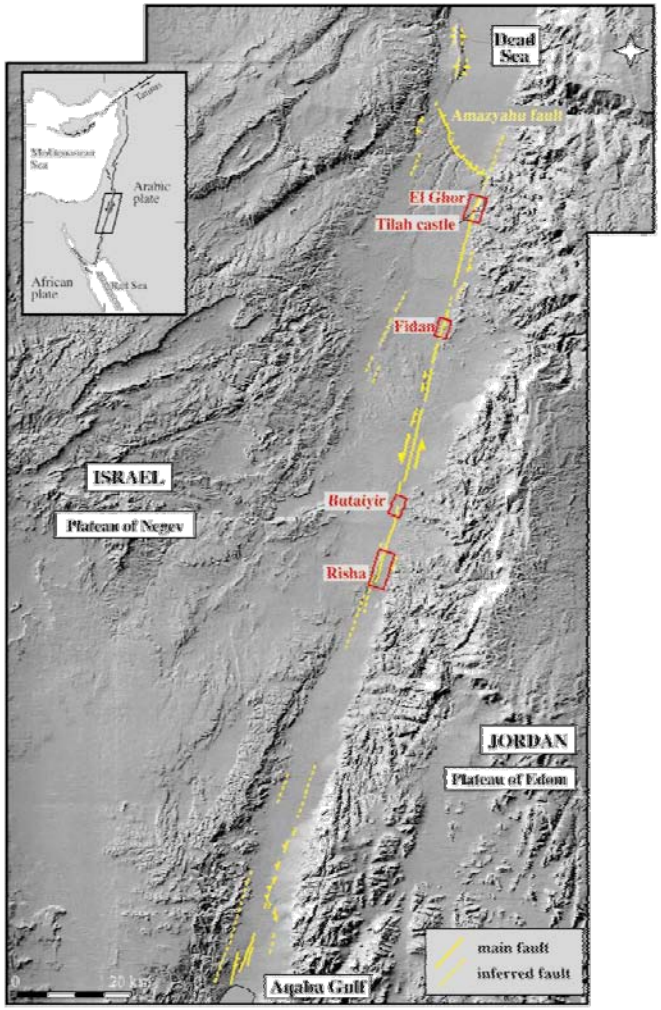

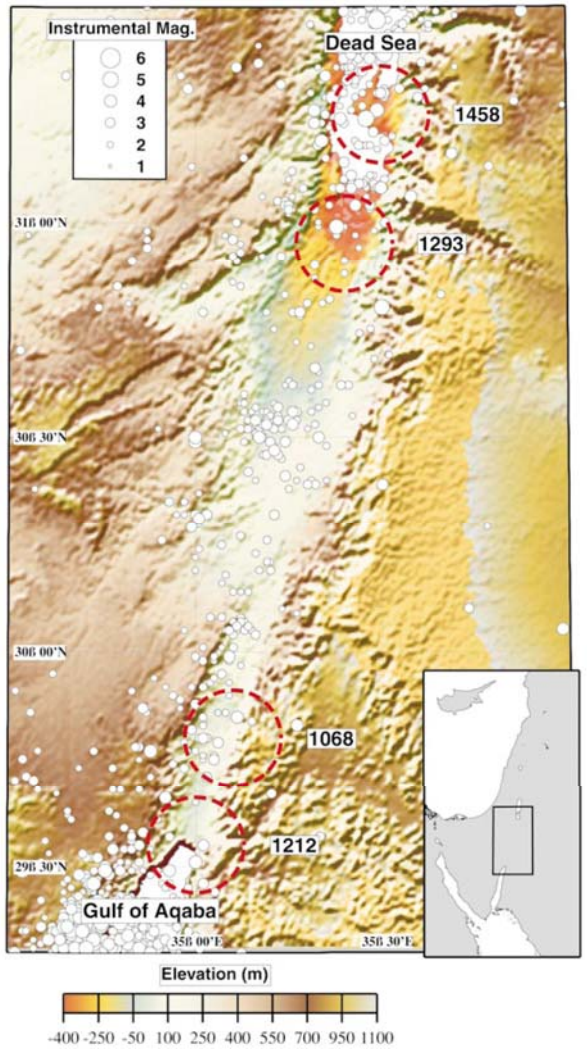

Recurrence intervals:
Klinger et al., (2000): 200 years for earthquakes Mw 7-7.2 (or larger earthquakes with longer intervals (e.g. Mw 7.6 every 6000 years).
Amit et al., (2002): Late Pleistocene: 2800+/-700 (Mw 6.7-7); Holocene: 1200+/-300 (Mw 5.9-6.7).
4 historical large earthquakes (Ambraseys et al., 1994):Two in the south (1068, 1212) and two in the north (1293, 1458).

Figure 6

The combined ages of boulders from the three investigated sites suggest that they were deposited in three events at 31 ka, 15 ka, and 4 ka. Paleoseismic studies in the area suggest a recurrence interval of 1000-2000 yr for earthquakes >M6. Therefore, it is apparent that boulder falls in the study area do not represent a full seismic record. This under representation implies that the on-going development of detachment cracks prior to triggering events is slower than the earthquake cycle and controls boulder formation or that boulder piles are formed only during big and rare earthquakes.

Figure 7

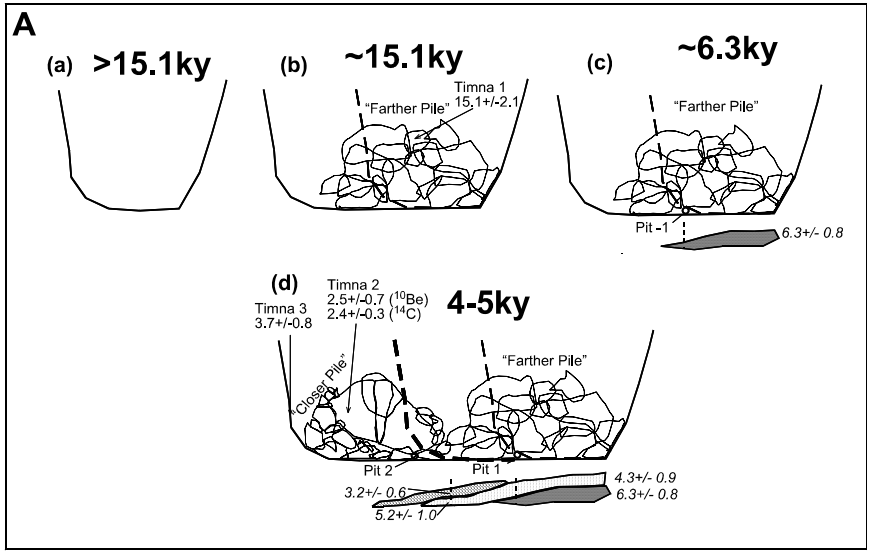

Cliff retreat rates determined from rock falls in Timna range between 0.14 and 2 m ky^{-1}. A more constrained range of 0.4 to 0.7 m ky^{-1} is calculated from the complete collapse cycles. Similar cliff retreat rates that range between 0.1 and 0.85 m ky^{-1} were calculated in other arid environments [e.g. Schumm and Chorley, 1966; Yair and Gerson, 1974; Mayer, 1979; Cole and Mayer, 1982].

In Timna, rates of cliff retreat are faster by an order of magnitude than the rate that the upper surfaces are lowered by weathering. Even though cliffs retreat through the episodic process of rock fall events while the upper surface weathers continuously, over time the difference in rates maintains the sharp morphology of Timna and vertical slopes (cliffs) do not roll back to become more gentle and rounded slopes.

Cliff retreat obviously initiated when voids large enough opened and enabled the collapse process to begin. This space opening was first accomplished through incision of stream channels through the sandstone following the development of the Arava Valley topographical base level. Assuming the range of cliff retreat rates calculated in this study, the 30 m wide Lower Valley opened approximately 40 - 70 ka. This range of ages determines the time at which the upstream-moving signal of the lowering base level of the DSF reached the Lower Valley site.

Figure 8

Reconstructing active rift margin tectonics using cosmogenic exposure age dating of desert pavements: Quaternary subsidence along the western margin of the Dead Sea Rift

Benny Guralnik[1]*, Ari Matmon[1]*, Yoav Avni[2], David Fink[3]

[1]Institute of Earth Sciences, The Hebrew University of Jerusalem
[2]Geological Survey of Israel
[3] Australian Nuclear Science and Technology Organization (ANSTO), Australia

arimatmon@cc.huji.ac.il

*Field guide

Fragmentation of drainage basins, their rearrangement, stream divergence, and consequent full drainage reversal occur in response to tectonic forcing such as subsidence of continental rift valleys and uplift of rift shoulders. We present new cosmogenic data from the Negev Desert, southern Israel, that shed light on the relations between the tectonic history of the western margins of the southern Dead Sea Rift (DSR) and drainage basin evolution since the Pliocene. In the Pliocene, a north-oriented river system drained the central Negev into the Dead Sea basin, collecting tributaries that originated east of the DSR and flowed westward (fig. 1). Tectonic deformation along the western margin of the DSR that began in the Pliocene caused regional eastward tilting and reversal of these tributaries by the early Pleistocene. Zero regional gradients which prevailed during the reversal stage, were accompanied by the accumulation of red beds and lake deposits, currently found on progressively lower elevations towards the rift, recording the Quaternary subsidence. To constrain the breakdown history of the Pliocene drainage system and reconstruct the Quaternary subsidence, we sampled mature desert pavement from 14 abandoned alluvial surfaces associated with the Plio-Pleistocene deposits. Seven samples were collected from the highest windgaps along major water divides, in which remnants of the early Pleistocene surface are preserved. Five of these samples yielded exposure ages that range between 1.9 Ma and 1.5 Ma (fig. 2). These ages bracket the collapse of the Pliocene drainage basin and suggest the eastward migration of this process. Seven other samples which yielded ages that range between 1.3 Ma and 0.5 Ma were collected from alluvial terraces inset into the early Pleistocene surface. They indicate stages of incision of the present drainage system. Under conditions of long-term hyperaridity and the absence of soil and vegetation desert pavement chert clasts are continuously exposed at the surface and do not erode. Thus, their cosmogenic isotope concentration may reflect changes in production rate due to elevation changes during exposure. By interpreting the cosmogenic isotope concentrations measured in the our easternmost samples as partially being produced at higher elevations we infer a minimum, and reasonable subsidence rate of ~130 m/Ma since 1.3 Ma (fig. 5). The detection of such a slight

change in elevation is enabled due to the unique condition of continuous exposure and no erosion of the chert clasts in the desert pavement.

Introduction

The present study focuses on the western margin of the Dead Sea Rift (fig. 1), in which the unique combination of hyperaridity, considerable subsidence during the Plio-Pleistocene (0.5 – 0.7 Km; Avni et al, 2000a), and the continuous exposure and extremely low erosion of desert pavement clasts (<0.2 m/Ma; Matmon et al, 2008) present a case-study for detecting a cosmogenic signal of tectonic activity.

Although basin fragmentation may occur even within a cratonic provenance (Chorowicz and Fabre, 1997), rift-induced modification of topography results in dramatic regional-scale flow reversals, as was reported from the Corinth–Patras Rift (Zelilidis, 2000), the Rio Grande Rift (Mack et al, 2006), Tasman Rift (Ollier, 1995), and East African Rift (Summerfield, 1991). Flow reversal was observed also in transform zones such as the East Anatolian Fault Zone (Boulton and Whittaker, 2008), and even in the glacial environments of the West Antarctic Rift system (Van der Wateren and Cloetingh, 1999, and references therein; Bart, 2004). Most commonly, paleo-flow directions are reconstructed by the inspection of windgaps, which are dry paleo-valleys that represent now-abandoned water courses (Keller et al., 1999; Burbank and Anderson, 2001). The time scale for river reversal has been recently demonstrated on the Palaeo-Nyabarongo River system, which switched from drainage into the East African Rift towards drainage away from it within approximately 300 – 350 Ka (Holzforster and Schmidt, 2007). A tectonic model for the drainage reversal induced by the Dead Sea leaky transform (traditionally referred to as "rift"; Garfunkel, 1981) was proposed by Wdowinski and Zilberman (1996), while specific drainage reversals have been reported from many locations along it (Kafri and Heimann, 1994; Matmon et al, 1999; Zilberman and Avni, 2006; Avni and Zilberman, 2007; Garfunkel and Horowitz, 1966; Ben David et al, 2002; Ginat et al, 1998; Ginat et al, 2000; Avni et al, 2000a).

The Negev Desert (10,000 km^2 at 29°–31°N, fig.1) is part of the larger Saharo-Arabian desert belt, and is currently among the driest places on Earth (Amit et al, 2006). Its Neogene history was dominated by the 18-14 Ma sinistral transform boundary between the present African and Arabian plates (Bartov et al, 1980; Garfunkel, 1981). During the Miocene, a >650 m thick section of the fluviatile Hazeva formation was deposited all over the Negev by westward-flowing rivers which originated hundreds of Km east of the transform and drained into the Mediterranean (Calvo and Bartov, 2001). The activity of this drainage system terminated at the latest ~6 Ma (Steinitz and Bartov, 1991; Steinitz et al, 2000). This termination coincides with the change in the plate's motion direction, which caused extension and initiated the development of the Dead Sea Rift as a deep inland drainage basin at ~5 Ma (Garfunkel, 1981). This tectonic phase was followed by the collapse

of the Miocene fluvial system, rift margin uplift, erosion of most of the Miocene sedimentary deposits, and the development of a N-S main water-divide along the western margins of the Dead Sea rift (Wdowinski and Zilberman, 1996).

By the early Pliocene, a new north-oriented river network known as the paleo-Paran drained most of the southern and central Negev into the Dead Sea basin. The sediments deposited by the paleo Paran drainage basin (the Arava formation) originated from the northern Sinai as well as from the Trans-Jordan Mountains (the "Edom Channel"; Ginat, 1998). Smaller westward-oriented paleo-rivers were identified as well (Avni, 1998; Avni et al, 2000a) (fig. 1). Although never directly dated, an age of 2-4 Ma was attributed to the Arava formation (Avni et al, 2000a).

During the Pliocene-Pleistocene transition, a simultaneous uplift of ~200 m of the Negev Highlands with the subsidence of ~500 – 700 m in the central Arava Valley, caused a gentle eastward tilting of a ~60 Km-wide strip about an axis roughly coinciding with the main channel of the Paleo-Paran. The proximity of the tilt axis to the paleo Paran channel is suggested by the location of the current active Paran channel only 1 – 3 Km east of its ancestor and <20 m below it (Avni et al, 2000a). In the vicinity of Mt. Zenifim (a local Plio-Pleistocene uplift axis), the axis of rotation is shifted to the east, and may be identified with the Paran Plains (fig. 1). The eastward tilting caused the fragmentation of the paleo Paran system into several smaller drainage systems (Paran, Hayyon, Neqarot, and Quraya) and relicts of the once westward-flowing rivers are found today at progressively lower elevations toward the east (Ginat et al, 1998; Avni et al, 2000a). During the period of stream reversal, as the regional gradients approached zero, a syntectonic sedimentary unit termed the Zehiha formation was deposited upon the stagnated channels (Ginat et al, 2002), masking the previous basin boundaries and promoting its break-up (Avni et al, 2000a). The resemblance of the fauna and hominid artifacts found in the Zehiha formation to those of 'Ubediya (Tschernov, 1987), assigned it an early Pleistocene age of ~1.4 Ma (Ginat et al, 2003). Although the tectonic framework of the Plio-Pleistocene is relatively well established, the fluvial deposits associated with this period lacked direct dating, limiting the understanding of the relationship between the tectonic and fluvial processes accompanying the subsidence of one of the most studied rift margins in the world.

Tectonic scenarios

The original elevations of the Pliocene Arava deposits along the presently reversed channels can be reconstructed by assuming a westward paleo-gradient similar to that of the present day Paran and Hiyyon channels (~4.5‰), and extrapolating it from the tilting axis (where no elevation change occurred) to the east (Ginat et al, 2000; Avni et al, 2000a). With these reconstructions, the cosmogenic concentrations at these sites can be subjected to two "end-member" interpretations (fig. 4). In the "pre-DP subsidence" scenario (fig. 4), the pavements developed after the surfaces reached

their final (stable) elevation. Thus, the cosmogenic concentration should reflect nothing but age and may point at the period (~400 ky) it took the paleo Paran system to completely disintegrate. The main weakness of the "pre-DP subsidence" scenario is that it forces the zero-gradient stage to be ≥ 1.9 Ma (equal or older than the oldest desert pavement sample PS-6). This is in contradiction to the assigned age of ~1.4 Ma of the deposits of lake Zihor and the associated red beds, which have been related with the fluvial stagnation during the gradient reversal (Ginat et al, 2002; 2003).

Alternatively, in the "post-DP subsidence" scenario (fig. 4), desert pavements were developed during the drainage reversal phase and at significantly higher elevations. A signal of subsidence postdating terrace abandonment should therefore be present in their cosmogenic concentrations, making their true abandonment ages slightly younger than simple exposure ages, based on a relationship derived below.

Denoting uplift and erosion rates (U, ε) and the reciprocals of atmospheric and rock attenuation lengths (M, μ), we expand Craig and Poreda's original model (1986) to account for an unstable nuclide, by including its disintegration constant (λ) in the "effective irradiation time", T (Lal, 1991):

$$T(U,\varepsilon) = \left(\lambda + MU + \mu\varepsilon\right)^{-1} \tag{1}$$

The ratio of the measured concentration in a sample (N) to the calculated in-situ production rate (P), must then satisfy the equation:

$$N / P = T(U,\varepsilon)\left(1 - \exp\left(-t / T(U,\varepsilon)\right)\right) \tag{2}$$

where t is the true exposure age, which can be expressed as

$$t = -T(U,\varepsilon)^{-1} \ln\left(1 - (N/P)\cdot T(U,\varepsilon)\right) \tag{3.1}$$

Since erosion of chert clasts in the Negev in desert pavements can be neglected equation (3.1) becomes:

$$t = -(\lambda + MU) \ln\left(1 - (N/P)\cdot(\lambda + MU)^{-1}\right) \tag{3.2}$$

The dependence between t and U for an observed N/P value, given by equation (3.2), may be represented by a curve which hereafter will be referred to as N/P plot (fig. 5). In such N/P plots simple exposure ages are obtained at the intersection of the N/P curve with $U = 0$ and for a fixed N/P ratio, there is a negative trend between exposure age and subsidence rate, one being on the expense of the other. The thin solid red and blue lines in figure 4 correspond to the observed N/P ratios at sites ES and EZ, respectively. The color band around the N/P curve represents the confidence interval due to the analytic uncertainty in N only. At this confidence interval, the observed N/P ratios of samples EZ ($1.082 \pm 0.005 \times 10^6$) and ES ($1.041 \pm 0.016 \times 10^6$) do not overlap, which means that the age of ES is significantly younger than that of EZ. This fact supports the geologic field relations: site EZ is situated on an uplifted and abandoned surface of the Edom Channel; it pre-dates the zero-gradient stage. On the other hand, desert pavement at site ES developed on top of the Zehiha formation, and post-dates the zero-gradient surface Based on known

rates of carbonate precipitation and soil formation, the time required to deposit the 15 m thick sequence of the Zehiha formation which separates both sampled surfaces was estimated to 50 – 150 Ky, (Ginat et al, 2003).

Since equation (3.2) is a solution of a differential equation, for any given point in the $U-t$ space, the tectonic rate U represents an averaged tectonic rate over the entire exposure age indicated by t. As a first-order approximation, constant tectonic rates may be assumed. Points 1 and 2 in figure 5 mark such combinations of age and constant subsidence rate (1.56 Ma at 10 m/My for EZ, 1.38 Ma at 142 m/My for ES). The product yields the estimated amount of subsidence since the Pleistocene (17 m at EZ and 195 m at ES). While the subsidence and the age shift for site EZ are negligible, the simple exposure age of ES shifts by about 100 Ky to 1.38 Ma, implying an age difference of 0.19 Ma between EZ and ES, corresponding to the time it took to deposit the Zehiha formation.

These averaged rates calculated above may significantly differ from instantaneous rates. Field evidence from the Negev suggests that the rapid tectonic activity that shaped the present basins during early Pleistocene diminished with time (Avni et al, 2000a). The cosmogenic concentrations at ES due to random monotonous subsidence histories (starting at 450 m asl, and ending today at 255 m asl) are simulated. Only those subsidence histories that produced the observed concentration at ES (within the analytic uncertainty in N and 5% uncertainty in P) are presented in figure 6. Despite the significant scatter, a trend of a diminishing tectonic activity with time is noticeable.

References

Amit, R., Enzel, Y., Sharon D., 2006. Permanent Quaternary hyperaridity in the Negev, Israel, resulting from regional tectonics blocking Mediterranean frontal systems. Geology 34, 509–512.

Avni, Y., 1998. Paleogeography and tectonics of the central Negev and the Dead Sea Rift western margin during the late Neogene and Quaternary. Geol. Surv. Isr. Rep. GSI/24/98, 231 pp. (in Hebrew, English abstr.)

Avni, Y., Bartov, Y., Garfunkel, Z., Ginat, H., 2000. The evolution of the Paran drainage basin and its relation to the Plio-Pleistocene history of the Arava Rift western margin, Israel. Isr. J. Earth Sci. 49, 215–238.

Avni, Y., Zilberman, E. 2007. Landscape evolution triggered by neotectonics in the Sede Zin region, central Negev, Israel. Isr. J. Earth Sci. 55, 189–208.

Bart, P.J., 2004. West-directed flow of the West Antarctic Ice Sheet across Eastern Basin, Ross Sea during the Quaternary. Earth Planet. Sci. Lett. 228, 425–438.

Bartov, Y., Steinitz, G., Eyal, M., Eyal, Y., 1980. Sinistral movement along the Gulf of Aqaba—its age and relation to the opening of the Red Sea, Nature 285, 220–221.

Ben-David, R., Eyal, Y., Zilberman, E., Bowman, D., 2002. Fluvial systems response to rift margin tectonics: Makhtesh Ramon area, southern Israel. Geomorphology 45, 147–163.

Boulton, S.J., Whittaker, A.C., 2008. Quantifying the slip rates, spatial distribution and evolution of active normal faults from geomorphic analysis: Field examples from an oblique-extensional graben, southern Turkey. Geomorphology, doi:10.1016/j.geomorph.2008.09.007

Burbank, D.W., Anderson, R.S., 2001. Tectonic Geomorphology. Blackwell Science, Oxford, U.K. 274 pp.

Calvo, R., Bartov, Y. 2001. Hazeva Group, southern Israel: New observations, and their implications for its stratigraphy, paleogeography, and tectono-sedimentary regime. Isr. J. Earth Sci. 50, 71–99.

Chorowicz, J., Fabre, J., 1997. Organization of drainage networks from space imagery in the Taneztouft Plateau Western Sahara: implications for the recent intracratonic deformation. Geomorphology 212, 139–151.

Garfunkel, Z., 1981. Internal structure of the Dead Sea leaky transform (rift) in relation to plate kinematics. Tectonophysics 80, 81–108.

Garfunkel, Z., Horowitz, A. 1966. The Upper Tertiary and Quaternary morphology of the Negev, Israel. Isr. J. Earth Sci. 15, 101–117.

Ginat, H., Enzel Y., Avni, Y., 1998. Translocated Plio-Pleistocene drainage systems along the Arava fault of the Dead Sea transform. Tectonophysics 284, 151–160.

Ginat, H., Zilberman, E., Avni, Y., 2000. Tectonic and paleogeographic significance of the Edom River, a Pliocene stream that crossed the Dead Sea Rift valley. Isr. J. Earth Sci. 49, 159–177.

Ginat, H., Zilberman, E., Saragusti, I., 2003. Early pleistocene lake deposits and Lower Paleolithic finds in Nahal (wadi) Zihor, Southern Negev desert, Israel. Quat. Res. 59, 445–458.

Holzforster, F., Schmidt, U., 2007. Anatomy of a river drainage reversal in the Neogene Kivu–Nile Rift. Quat. Sci. Rev. 26, 1771–1789.

Kafri, U., Heimann, A., 1994. Reversal of the palaeodrainage system in the sea of Galilee area as an indicator of the formation timing of the Dead Sea rift valley base level in northern Israel. Palaeog., Palaeocl., Palaeoec. 109, 101–109.

Keller, E.A., Gurrola, L., Tiernay, T.E., 1999. Geomorphic criteria to determine direction lateral propagation of reverse faulting and folding. Geology 27, 515–518.

Lal, D., 1991. Cosmic ray labeling of erosion surfaces: in situ nuclide production rates and erosion models. Earth Planet. Sci. Lett. 104, 424–439.

Mack, G.H., Seager, W.R., Leeder, M.R., Perez-Arlucea, M., Salyards, S.L., 2006. Pliocene and Quaternary history of the Rio Grande, the axial river of the southern Rio Grande rift, New Mexico, USA, Earth Sci. Rev. 79 (1-2), 141–162.

Matmon, A., Enzel, Y., Zilberman E., Heimann A., 1999. Late Pliocene and Pleistocene reversal of drainage systems in northern Israel: tectonic implications. Geomorphology 28, 43–59

Matmon, A., Simhai, O., Amit, R., Haviv, I., Enzel, Y., Porat, N., McDonald, E.V., Benedetti, L., Finkel, R.C., 2009. Desert pavement–coated surfaces in extreme deserts present the longest-lived landforms on Earth. Geol. Soc. Am. Bull., doi: 10.1130/B26422.1.

Ollier, C.D., 1995. Tectonics and landscape evolution in southeast Australia. Geomorphology 12, 37–44.

Reconstructing active rift margin tectonics using cosmogenic exposure age dating of desert pavements: Quaternary subsidence along the western margin of the Dead Sea Rift

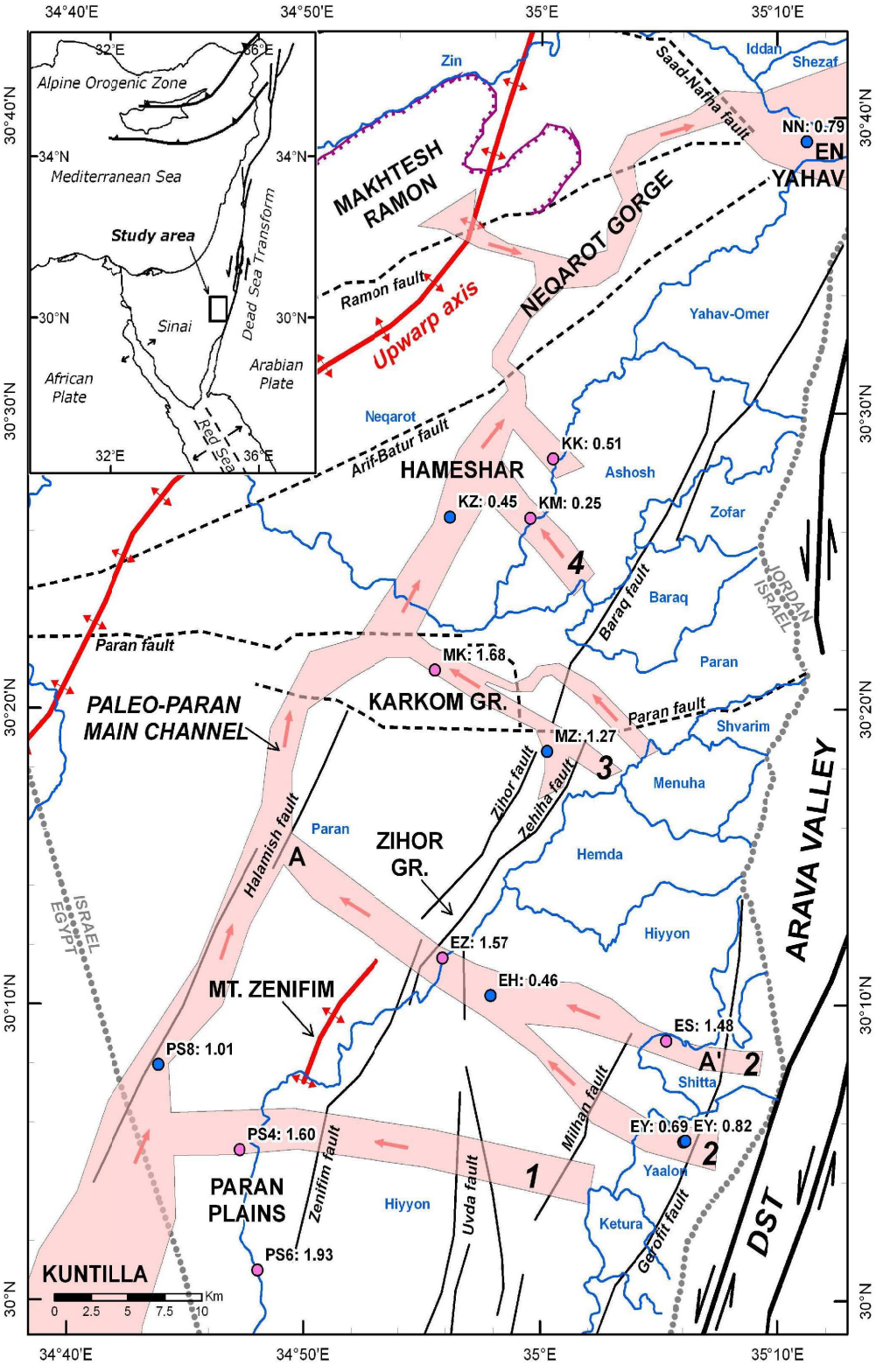

Figure 1: Study area. Present-day drainage basins are outlined in blue, faults in black, Plio-Pleistocene upwarp axes in red. Reconstructed paleo-Paran drainage is outlined in pink (arrows indicate flow direction), major tributaries are numbered: 1 – Zenifim, 2 – Edom, 3 – Menuha, 4 – Kippa. Sample locations and their simple exposure ages are indicated by small circles, pink for watergap samples, blue for stream inset samples. A-A' is the cross section locations. Sources: Ginat (1997), Avni (1998), Ginat et al (2000), Avni et al (2000)

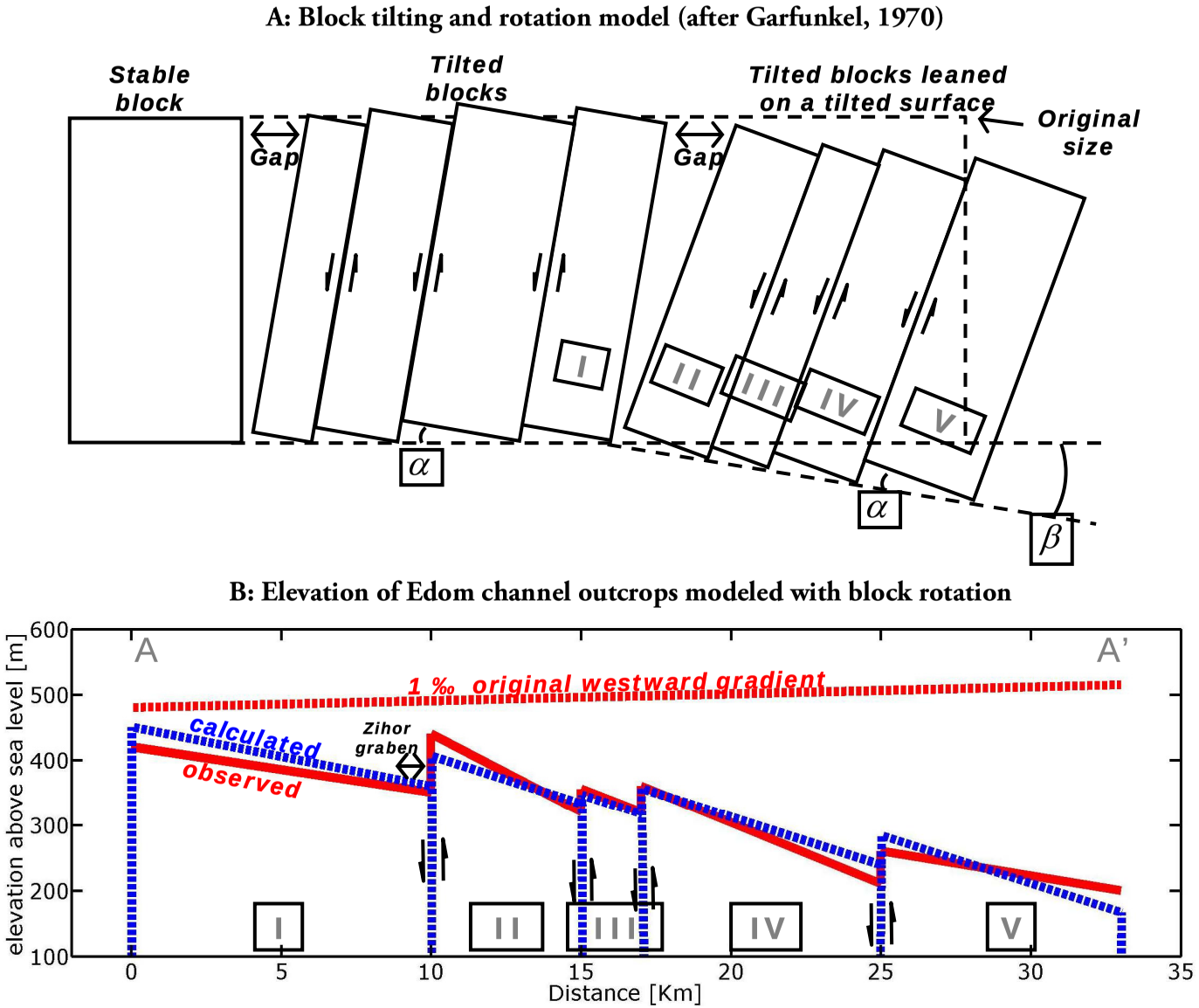

Figure 2: A – Block rotation model: regional rotation (by an angle of β for blocks II-V), is superimposed on local rotation (by an angle of α and common to all blocks), no vertical exaggeration. B – Observed and modeled elevations of the Edom channel facies along transect A-A' (see figure 1), vertical exaggeration of ~20. The model uses a pre-reversal gradient of 1‰, block height of 2 Km, subvertical faults (dipping >80°), α=0.3° and β=0.6°; calculated elevations reproduce actual heights of outcrops within a precision of 30 m.

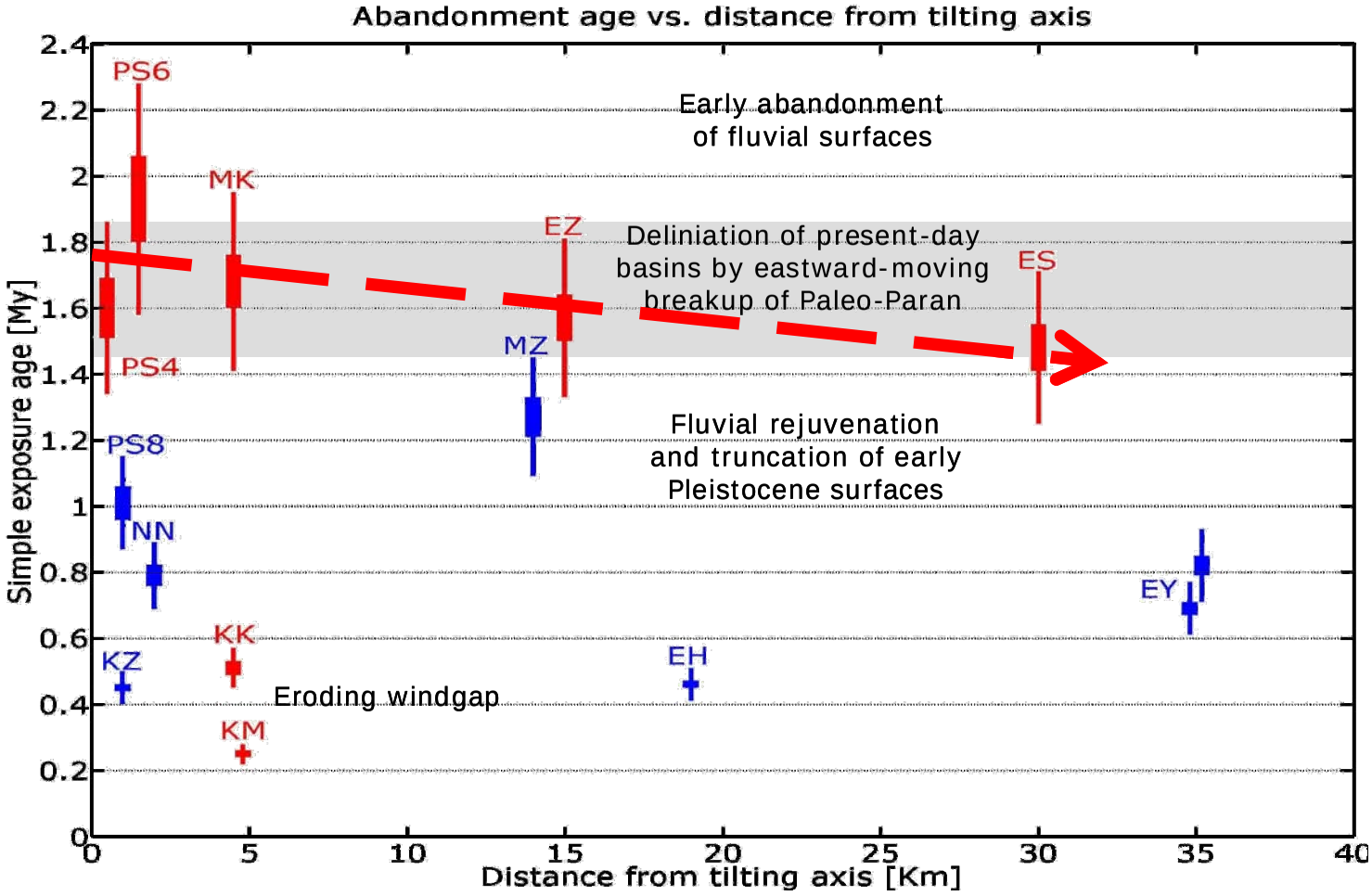

Figure 3: Simple exposure ages of desert-pavements at major windgaps (red) and on inset surfaces (blue), plotted against site distance from the Quaternary tilt axis. Random errors are indicated by thick bars, systematic uncertainty of 10% about the production rate by thin bars. Excluding the anomalously young windgaps of the Meshar (KK and KM), average windgap age is 1.65 ± 0.20 Ma. Red dashed line suggests that the basin breakup propagated in an eastward direction.

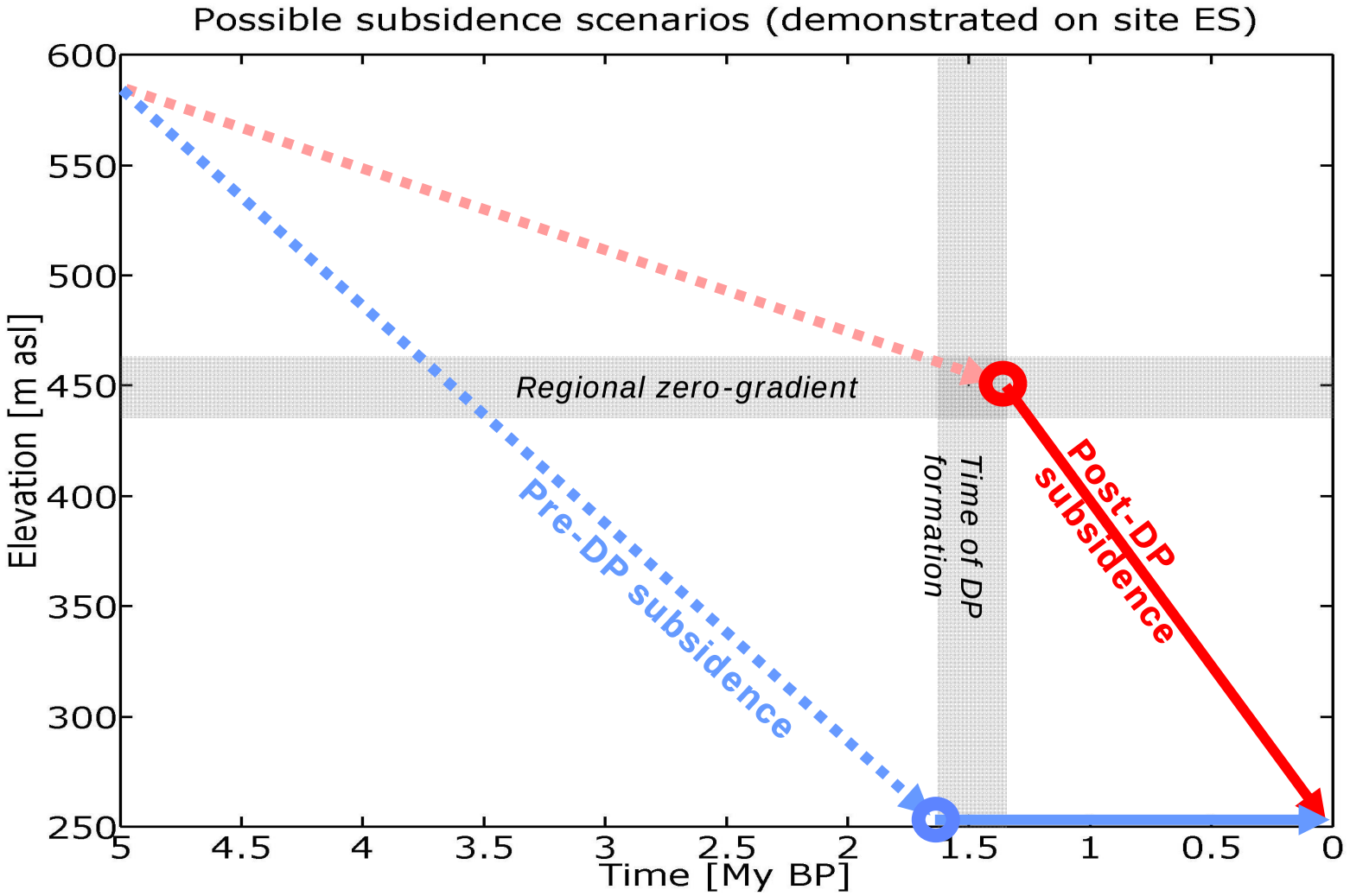

Figure 4: Desert Pavement (DP) development scenarios. Grey areas represent the elevation of regional zero gradient and age of Desert Pavement formation. Blue line represents the "Pre-DP subsidence" scenario, in which the pavements are formed at their present elevation and record age only. Red line represents the "Post-DP subsidence" scenario, in which the pavements are formed at a higher elevation and include a mixed signal of age and subsidence.

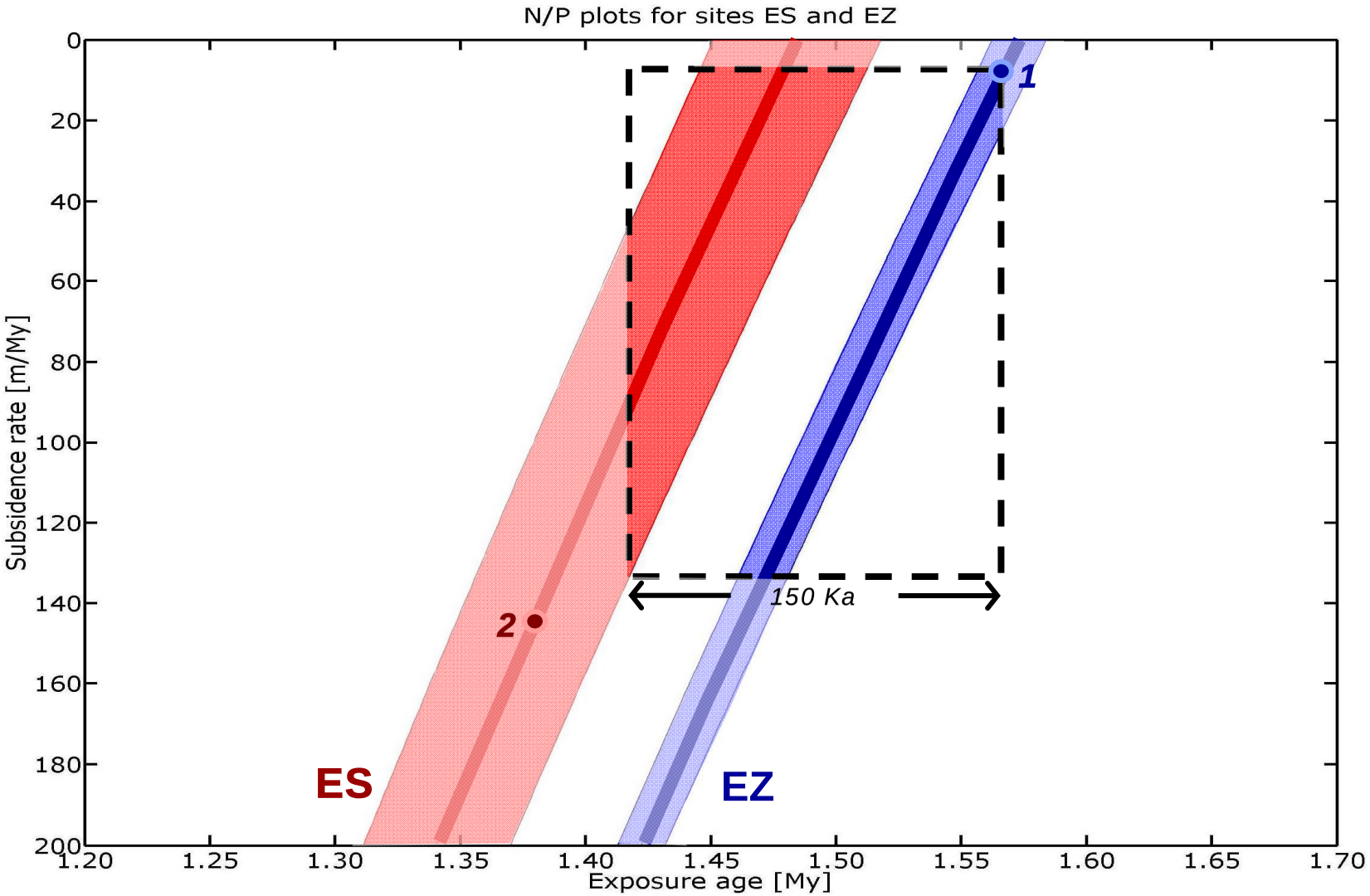

Figure 5: N/P plot: the continuous lines represent all possible combinations of constant uplift rate and true exposure age for a given sample. Simple exposure ages are given by the intersection of the curves with the U=0 line. Red and blue dots represent the corrected age assuming continuous subsidence at a constant rate.

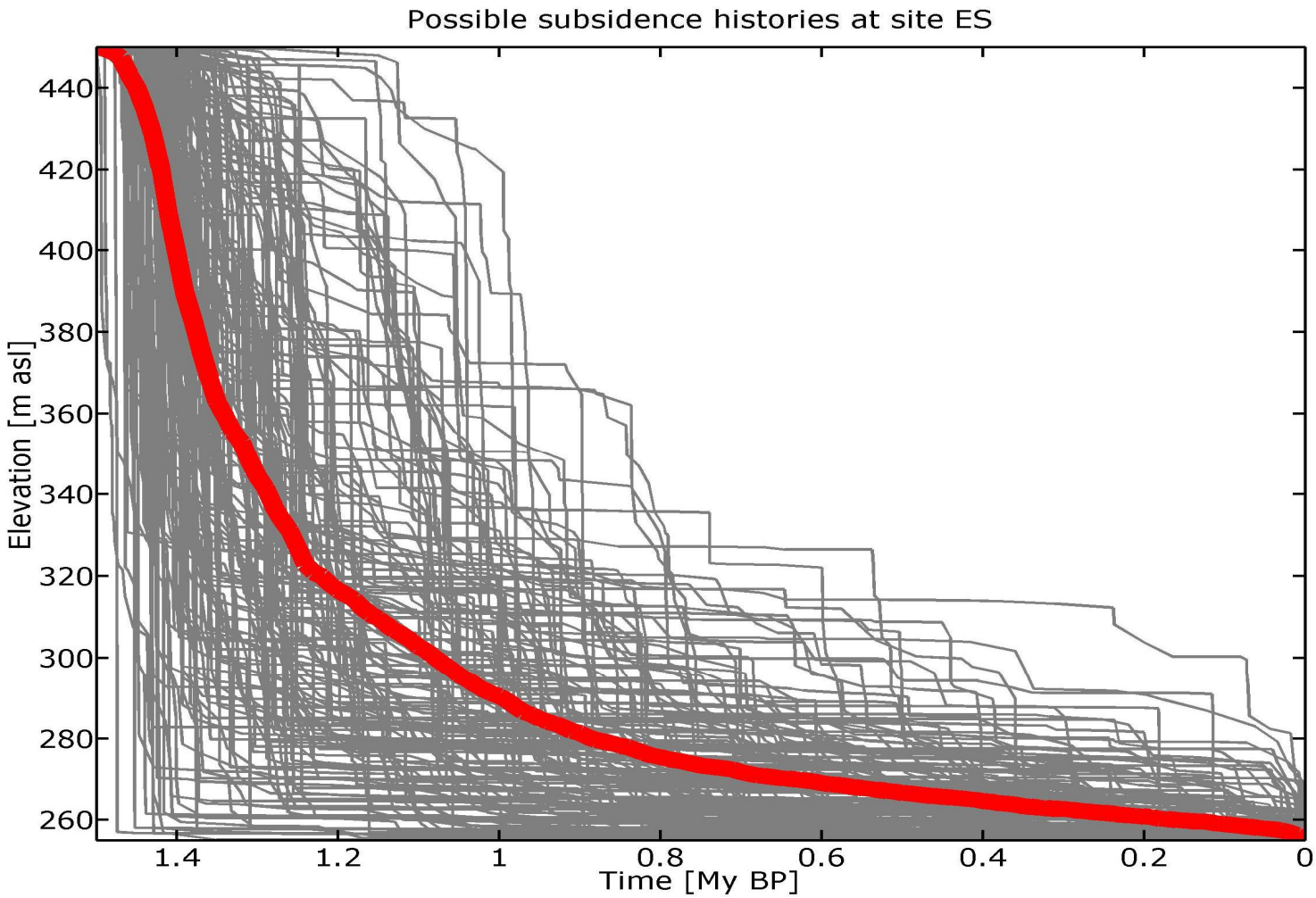

Figure 6: Plot of all possible subsidence histories at site ES, assuming <150 Ka for the deposition of Zehiha formation. Shown are histories which produced N/P values within the analytic uncertainty in N and a 5% uncertainty in P. The red line is an averaged history.

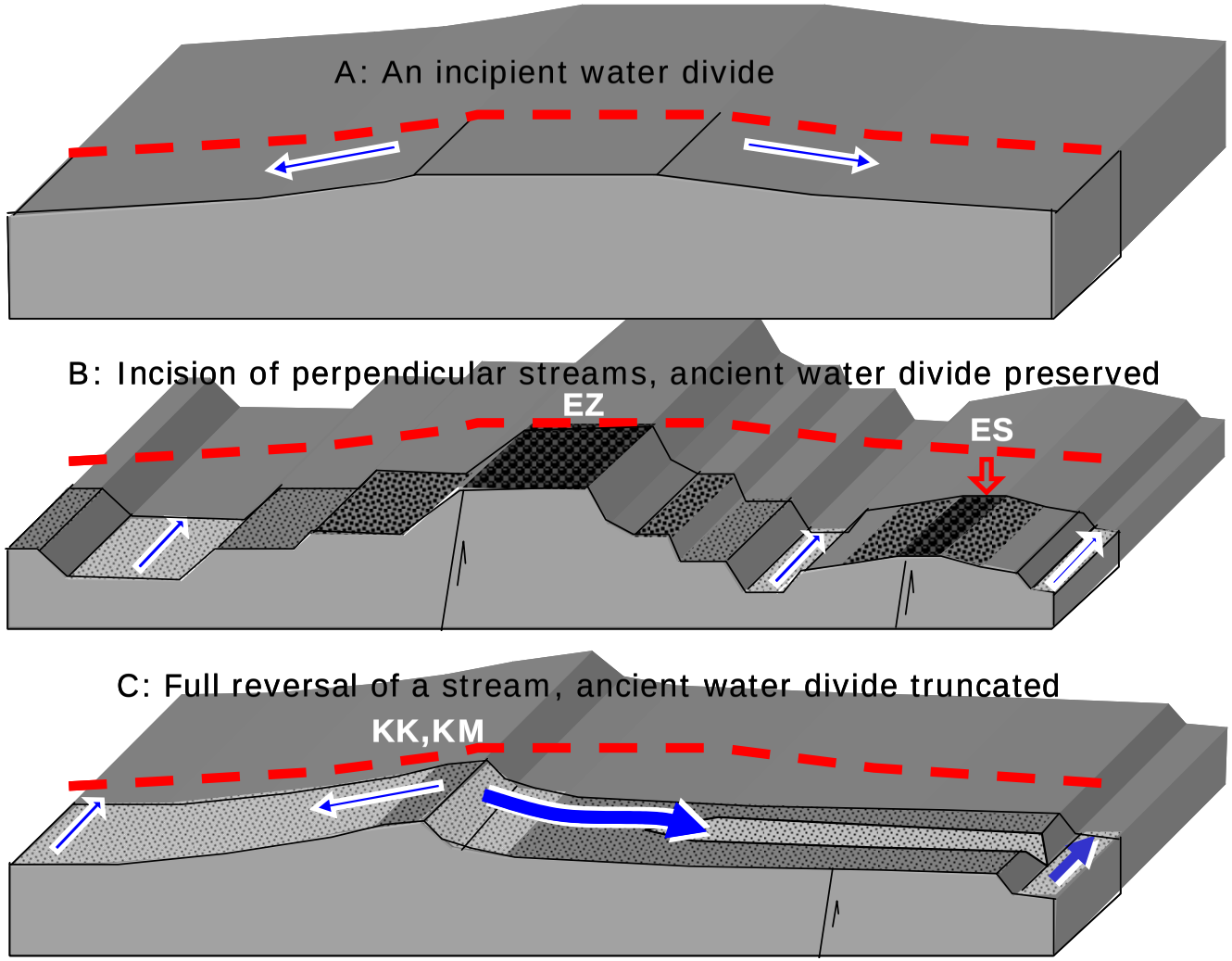

Figure 7: Scenarios for preservation or destruction of surfaces dating a basin's breakup. A – emergence of a new water divide and development of desert pavement in the windgap. B – emergence of a drainage network parallel to the water divide; drainage off the wingap is minimal, and the original abandoned surfaces are preserved. C – emergence of drainage networks away from the windgap causes its truncation and backward migration of the water divide.

Judean Mountains

23.2.2009

Field leader

Elisa Kagan

Dead Sea
Ein - Feshcha
Judean Desert
Ramallah
Jerusalem
Bethlehem
Yad Ha-Shmona
Sorek Cave
N
0
2
4
8
Kilometers

Speleoseismology in the Soreq Cave: The first dated ultra-long record of strong earthquakes

Kagan Elisa[1,2*] Miryam Bar-Matthews[2*], Avner Ayalon[2*] Amotz Agnon[1*]

[1] Institute of Earth Sciences, The Hebrew University of Jerusalem
[2]Geological Survey of Israel

elisa.kagan@mail.huji.ac.il

*field guide

Research of past earthquakes, typically retrieving records from soft sediment deformations, can benefit from the study of rockfalls and damaged deposits in caves. Dating of damaged speleothems and deposits overgrowing rockfalls constrains the dates of earthquakes. We have compiled a long-term (~200 kyr) paleoseismic record at the Soreq and nearby Har-Tuv caves, near Jerusalem. The study caves, located 40 km west of the Dead Sea Transform, record earthquake damage from Dead Sea Transform ruptures and, possibly, smaller local intraplate events. The caves were discovered by quarrying activity at 1968, before which they were entirely closed.

In the Soreq Cave, we will see a large variety and quantity of speleoseismites. We will see collapsed cave ceilings, fallen stalactites, fallen columns, stalagmites with their tops severed, and cracks (Fig. 1). Many of these damaged cave deposits are covered in post-collapse regrowth, be it a thin film of calcite, flowstone, or stalagmites, which constrain damage age. Also, the crack network will be seen, through which most of the water entering the cave seeps.

Non-seismic sources of collapse, such as ice-movements, ground subsidence, and cave-bears, problematic elsewhere, were considered and refuted. Neither ice cover, nor perma-frost, has occurred in this region during the investigated period. Ground subsidence does not pose a problem since the cave floors are solid carbonate rock. The caves have only non-natural recent openings; therefore pre-1960's animal or anthropogenic effects are not a possibility. The study caves offer an excellent opportunity for paleoseismic research as they contain a large amount of damaged deposits. The two study caves present the opportunity to correlate between two nearby sites.

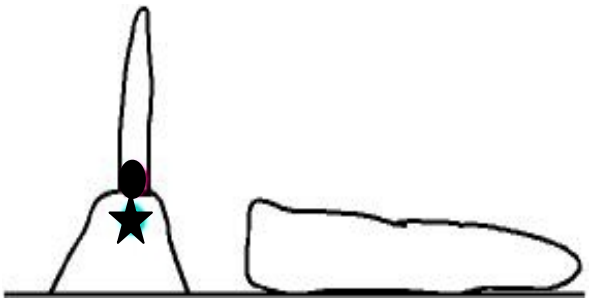

Fig 1a

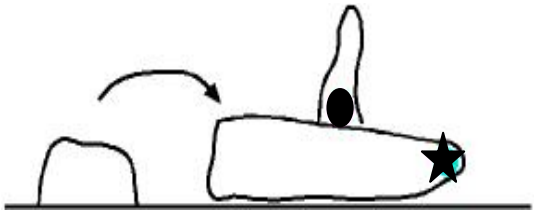

Fig 1b

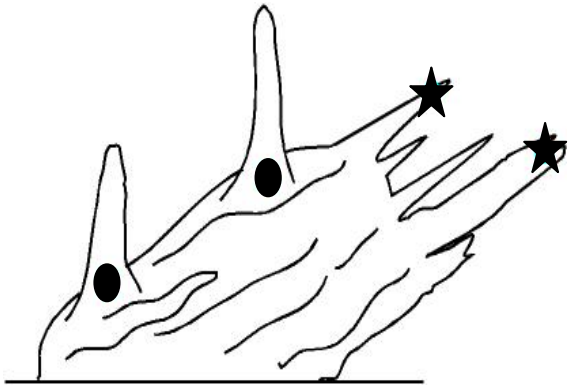

Fig 1c

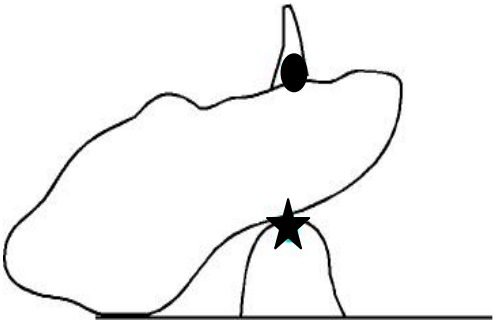

Fig 1d

Figure 1: Some of the types of speleoseismites to be seen in the Soreq Cave. Stars denote pre-earthquake age, circles denote post-earthquake age. 1a-Severed stalagmite and post-break stalagmite regrowth. 1b- Severed stalagmite and post-break stalagmite regrowth off the pre-earthquake location. 1c- Collapsed group of stalactites with post-collapse stalagmite regrowth. 1d-Collapsed block covering previously active stalagmite, with new stalagmite regrowth on block.

The Soreq and Har-Tuv caves were mapped at considerable resolution and the detailed maps demonstrate dominant EW and NW-SE orientation of fractures, and dominant EW and NS orientation of collapsed speleothems (Fig. 2). The prevailing orientations of collapsed speleothems are equivalent to directions of ground motion during the passage of surface waves emitted from the Dead Sea transform. These preferential orientations of collapse strongly support a seismic source of collapse. We identified "new generations" of speleothem growth on top of collapses. This post-collapse precipitation constrains ages of collapse. The unconformities between the collapses and the in-situ regrowth were recognized, and termed paleoseismic "contacts" or "horizons". Laminae above and below the unconformity were

separated and dated by the $^{230}Th/^{234}U$ mass spectrometry method at the MC-ICP-MS at the Geological Survey of Israel. The pre-seismic and post-seismic dates of a collapse bracket the period within which the earthquake occurred. The closer in age the pre-seismic and post-seismic deposits are, the better constrained is the earthquakes age. When dating post-seismic regrowth on collapsed bedrock (and not collapsed speleothem), only the post-seismic age is available. We also drilled cores into the flowstone floor and discovered laminae that embed fallen small stalactites (soda-straw formations) (Gilli et al., 1999). We dated the laminae that embed the fallen stalactites, which give the age of the seismic event. We also compared the oxygen stable isotopic record (^{18}O) of the laminae adjacent to the tectonic unconformities with the extensive well-dated stable isotope record of Soreq Cave speleothems, as was reconstructed for the last 185 kyr by Bar-Matthews et al. (2000) and Ayalon et al. (2002). This stable isotope comparison technique improves and corroborates the U/Th ages. It also helps us to rule out climatic events as sources for rockfalls.

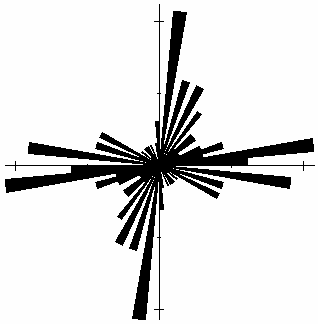

Figure 2: Rose diagram (intervals of 5°) depicting the orientations of the long axes of fallen speleothems in the Soreq Cave. Sixty fallen speleothem orientations were measured and incorportated into this diagram. Dominant EW and NS orientations are evident.

Seventy damaged speleothems were sampled and dated from which about twenty separate events were defined. The Holocene events observed in the cave correlate with lacustrine seismites dated in cores from the Dead Sea and with historically or archeologically recorded earthquakes: 185±30 yr BP correlates with an earthquake in the 1830's, 250±30 yr BP correlates with an earthquake that took place in 1759. Both dates refer to post-earthquake dripping, and we do not have positive evidence for large ground accelerations (yet these dates may correspond to crack opening responding to stress redistribution). 4400 ±400 yr BP may correlate with an archaeologically recorded earthquake from Tel Ai at ~4.7 ka (Karcz et al., 1977) and 4.6 ±0.9 ka marginal DST fault displacement (Gluck, 2001). It also correlates with a breccia layer from the Dead Sea (Migowski et al., 2004; Agnon et al., 2006). All cave events have lacustrine counterparts, but many lacustrine events do not

correlate with cave events. This may suggest that the cave filters out the smaller events and records only the larger events (Kagan et al., 2005, 2007).

For the period correlating to the Last Glacial paleo-Dead Sea Lisan Fm (75 to 20 ky) we identified ~6 events, three to four (~ 38, 40, 53, and 70 ka) of which correlate with lacustrine soft sediment deformation in all studied Lisan paleoseismic sites and additional two events (~ 47, 26 ka) which correlate with only some Lisan sites (Kagan et al., 2007). Cave-recorded events older than 75 ka (at approximately 75, 85, 108, 119, 128, 133, 150, 155, 180 ka) are at present the only dated paleoseismic record for this period in the central Dead Sea region and present a promising breakthrough in long-term paleoseismic research.

The karstic paleoseismic record supports the lacustrine seismite evidence, and the long dating range of calcite cave deposits and their potential for recording seismic events can vastly increase the length of the seismic record and are valuable for seismic hazard assessment.

References:

Agnon, A., Migowski, C., and Marco, S., 2006. Intraclast breccia layers in laminated sequences: recorders of paleo-earthquakes, in Enzel, Y., Agnon, A., and Stein, M., eds., New Frontiers in Dead Sea Paleoenvironmental Research, Geological Society of America Special Paper 401, p. 195-214.

Ayalon, A., Bar-Matthews, M. and Kaufman, A., 2002. Climatic conditions during marine isotopic stage 6 in the Eastern Mediterranean region as evident from the isotopic composition of speleothems: Soreq Cave, Israel. Geology, 30, 303-306.

Bar-Matthews, M., Ayalon, A., Kaufman, A., 2000. Timing and hydrological conditions of sapropel events in the Eastern Mediterranean, as evident from speleothems, Soreq cave, Israel. Chem. Geol., 169,145-156.

Gilli E, Levret A, Sollogoub P, et al., 1999. Research on the February 18, 1996 earthquake in the caves of Saint-Paul-de-Fenouillet area, (eastern Pyrenees, France), Geodynamica Acta 12, 143-158.

Gluck, D., 2001. The landscape evolution of the southwestern Dead Sea Basin and the paleoseismic record of the southwestern marginal fault of the Dead Sea Basin and of the Carmel Fault during the Late Pleistocene and the Holocene: Jerusalem, The Hebrew University.

Kagan, E.J, Agnon, A., Bar-Matthews, M., 2005. Dateing large, infrequent earthquakes by damaged cave deposits. Geology 33, 261-264.

Kagan, E.J, Stein, M., Bar-Matthews, M., Agnon, A., 2007. A Tale of Two Cataclysmic-Earthquakes: 39 and 52 kyr BP, Dead Sea Transform, Israel; a Multi-archive Study. AGU, Fall Meeting 2007, San Francisco, Session T12.

Karcz, I., Kafri, U. Meshel, Z., 1977. Archaeological evidence for subrecent seismic activity along the Dead Sea-Jordan rift, Nature 269, 234 – 235.

Migowski, C., Agnon, A., Bookman, R., Negendank, J. F. W., and Stein, M., 2004, Recurrence pattern of Holocene earthquakes along the Dead Sea transform revealed by varve-counting and radiocarbon dating of lacustrine sediments: Earth and Planetary Science letters 222, 301-314.